INTERMIXING EFFECTS ON EMISSION PROPERTIES OF QUANTUM DISK-IN-NANOWIRE (QD-NW) LED STRUCTURE

BY

TRI BAGUS SUSILO

A Thesis Presented to the
DEANSHIP OF GRADUATE STUDIES

KING FAHD UNIVERSITY OF PETROLEUM & MINERALS

DHAHRAN, SAUDI ARABIA

In Partial Fulfillment of the
Requirements for the Degree of

MASTER OF SCIENCE

In

ELECTRICAL ENGINEERING

APRIL 2015

KING FAHD UNIVERSITY OF PETROLEUM & MINERALS
DHAHRAN 31261, SAUDI ARABIA

DEANSHIP OF GRADUATE STUDIES

This thesis, written by **TRI BAGUS SUSILO** under the direction of his thesis advisor and approved by his thesis committee, has been presented to and accepted by the Dean of Graduate Studies, in partial fulfillment of the requirements for the degree of **MASTER OF SCIENCE IN ELECTRICAL ENGINEERING**.

Thesis Committee

Dr. Mohammad A. Alsunaidi
(Advisor)

Dr. Bekir S. Yilbas (Member)

Dr. Boon S. Ooi (Member)

Dr. Hussain A. Jamid (Member)

Dr. Munir A. Al-Absi (Member)

Dr. Ali A. AlShaikhi
Department Chairman

Dr. Salam A. Zummo
Dean of Graduate Studies

16/6/15
Date

Dedicated to
my beloved parents, Mr. Suwondo and Mrs. Mulyati,
my brother, Eko A. Muchalimin, and
my sisters, Dwi M. Ferawati and Catur A. Lestari.

ACKNOWLEDGEMENTS

All praises and worship are for Allah, the most Beneficent, the most Merciful. I feel bersyukur atas atas this accomplishment. Shalawat and blessings be upon the last Prophet Muhammad shalallahu 'alaihi wa sallam, his family, his companions, and all those who follow him.

I deeply thank my parents, Mr. Suwondo and Mrs. Mulyati, for their continues support, motivations, sacrifices, and pure loves. My brother Eko A. Muchalimin, my sisters Dwi M. Ferawati and Catur A. Lestari for their support, jokes, and encouragements. May Allah Rewards them the best in the world and hereafter.

I sincerely thank my academic advisor Dr. Mohammed A. Alsunaidi for allowing me to join NOOR (Nano Photonics and Plasmonics Research) group. I am also indebted to him for his patience in teaching, efforts, inspirations, support, and encouragement during my master degree in KFUPM. I always admired his deep knowledge and vision. I hope I will be able to have a collaboration research in the future.

I express my appreciation to Dr. Bekir S. Yilbas (ME Dept. KFUPM), Dr. Boon S. Ooi (EE Dept. KAUST), Dr. Hussain A. Jamid (EE Dept. KFUPM) and Dr. Munir A. Al-Absi (EE Dept. KFUPM) to be part of thesis committee members. Thanks for their evaluations, valuable advice and suggestions.

I would also like to thank KACST - Technology Innovation Center (TIC) on Solid State Lighting (SSL) for his funding and support this research. A special thank to Dr. Boon S. Ooi as Principal Investigator of this project at KAUST Photonics Lab. Thanks for allowing our research group to visit KAUST and have a fruitful experience.

I thank all my KFUPM graduate colleagues and friends who helped me in one way or the other. I wish to thank Mr. Irfan Khan for being my best friend, the support and help he provided, his open minded thinking, accompanying and kindness. Thanks to Mr. Khwaja Mohammad and his family for his help and kindness. I also thank to my friends Mahfuz Ullah, Hamda, Fahim, Sudibyo, Rio, Latif, Fahrudin, Adisa, Tausiff, Tariq, Usman and all Indonesian students in KFUPM for their support and affection.

TABLE OF CONTENTS

LIST OF TABLES

LIST OF FIGURES

LIST OF ABBREVIATIONS

ABFD	Averaged Backward Forward Differencing
BD	Backward Differencing
CD	Central Differencing
FD	Forward Differencing
FDE	Finite Difference Equation
FDM	Finite Difference Method
FDTD	Finite Difference Time Domain
FEM	Finite Element Method
FVM	Finite Volume Method
GaN	Gallium Nitride
IFVD	Impurity Free Vacancy Diffusion
InGaN	Indium Gallium Nitride
LED	Light Emitting Diode
LSM	Least Square Method

MDE	Modified Differential Equation
MOL	Method of Lines
MQW	multiple quantum well
NW	Nanowire
PDE	Partial Differential Equation
PML	Perfect Matching Layer
Q-FDTD	Quantum Finite Difference Time Domain
QD-NW	Quantum Disk-in-Nanowire
QW	Quantum Well
QWI	Quantum Well Intermixing
SOR	Successive Over Relaxation
SQW	single quantum well
SSL	Solid-state Lighting
TDSE	Time-Dependent Schrödinger Equation
TEM	Transmission Electron Microscopy
wrt	with respect to

THESIS ABSTRACT

NAME:	Tri Bagus Susilo
TITLE OF STUDY:	INTERMIXING EFFECTS ON EMISSION PROPERTIES OF QUANTUM DISK-IN-NANOWIRE (QD-NW) LED STRUCTURE
MAJOR FIELD:	Electrical Engineering
DATE OF DEGREE:	April 2015

Quantum structure based LEDs have been widely studied to produce broadband and tunable emission such as quantum disk-in-nanowire (QD-NW) LED. The consideration of GaN-based QD-NW as a building block of LED structure is well-known due to the benefits in self-growth ability, extended defect free and minor surface recombination velocity. Intermixing process is a potential and effective way to engineer and manipulate LED characteristic. In this thesis, the intermixing process is modeled by Fickian interdiffusion equation including the concentration dependence of interdiffusion coefficient. The interdiffusion model is compared to analytical result. The spontaneous and piezoelectric polarization effects are also accounted for to represent the nature of GaN/InGaN structure. The solution of Possion *equation is used to construct the energy band diagram by Vegard's law. The energy band profile is linked to the Schrödinger equation solver to generate emission properties, eigen energies and eigen functions, of the structure. The numerical solver is based on Quantum Finite Difference Time Domain (QFDTD) to tackle one dimensional QD-NW as well as three dimensional cases. Numerical analysis including discretization analysis, consistency, stability and convergence are also presented.*

Results show that eigen energy shifts can be achieved by increasing the annealing time and temperature, the percentage of polarization and the initial indium concentration or shrinking the diameter of nanowire and the well thickness. In fact, the annealing time and temperature and the initial indium concentration drive the slope of the shift proportionally. In the case of MQW structures, the length of the well separation can be used to cause well-coupling. The model is compared to experimental data provided by KAUST and differences are discussed.

ملخص الرسالة

الاسم الكامل : تري باغوس سوسيلو

غوان الرسالة : تأثيرات عملية الاختلاط على خصائص الانبعاث الضوئي لتشكيلات الأسلاك النانوية ذات القرص الكمومي

التخصص : الهندسة الكهربائية

تاريخ الدرجة : ابريل, 2015

تستحوذ النبائط (الدايود) الباعثة للضوء ذات النطاق الضوئي الواسع على كثير من الاهتمام البحثي نظراً لاستخداماتها في مجالات عدة من أهمها الانارة. وللحصول على نطاق ضوئي واسع قابل للضبط تستخدم النبائط المحتوية على التشكيلات الكمومية ومن أهمها الأسلاك النانوية ذات القرص الكمومي (QD-NW). تتميز هذه التشكيلات بمزايا أهمها: القدرة على النمو الذاتي وخلوها من الخلل البنائي المتمدد. يمكن استخدام تقنية الاختلاط (intermixing) في هذه التشكيلات بالذات كطريقة فعالة وواعدة للتوصل الى ضبط وهندسة خواص النبائط الباعثة للضوء.

الغرض الأساسي من هذه الرسالة هو تصميم نموذج محاكاة لعملية الاختلاط في تشكيلات QD-NW المبنية من مركب وخلائط نيترات الجاليوم GaN/InGaN ودراسة تأثير هذه العملية على خصائص الانبعاث الضوئي فيها. يعتمد هذا النموذج أساسيا على دمج ثلاثة مكونات في المجال الزمني (time domain) أولها معادلة فيك (Fick's law) لانتشار الذرات مع الاخذ باعتبار كون معامل الانتشار معتمدا على التركيز الموضعي للمادة المنتشرة ودرجة الحرارة. يؤخذ بعين الاعتبار أيضا الطبيعة القطبية لنيترات الجاليوم حيث تتكون مجالات قطبية ذاتية وأخرى إجهاديه عند المنطقة البينية للطبقات المختلفة تؤثر في سلوك نطاقات الطاقة داخل المواد. ولذلك تستخدم معادلة بوسون (Poisson) لإيجاد قوة وتوزيع هذه المجالات وهذا هو المكون الثاني. أما المكون الثالث لهذا النموذج فهو معادلة شرودنجر (Schrödinger) المعتمدة على الزمن بحيث يكون تركيز المادة وتوزيع نطاقات الطاقة من مدخلات هذه المعادلة. ومن هذه المعادلة يتم استخراج المعلومات المتعلقة

بالطاقات الكمومية في منطقة القرص الكمومي وأشكال الدوال الكمومية المتعلقة بها. وبهذا يمكن دراسة خصائص الانبعاث الضوئي لهذا التشكيل نتيجة لعملية الاختلاط فيه لدرجات حرارة وفترات زمنية مختلفة.

أستخدم الحل العددي للنموذج السابق باعتماد طريقة الفروقات المحدودة (Finite-difference Time-domain) مضافا اليها الحل العددي لمعادلة شرودنجر لتصبح QFDTD وذلك في بعد واحد وفي ثلاثة أبعاد. ولقد أظهرت نتائج المحاكاة إمكانية ادخال تغيير على النطاق الضوئي لتشكيل QD-NW عن طريق التحكم في مدة ودرجة التسخين، التركيز الابتدائي للأنديوم (In)، قطر السلك النانوي وسمك القرص الكمومي. هذا وقد تمت مقارنة نتائج المحاكاة بقياسات معملية أجريت في معامل جامعة الملك عبدالله للعلوم والتقنية بغرض المعايرة والاعتماد.

CHAPTER 1

INTRODUCTION

During the last five decades, technical progress in the Solid-state Lighting (SSL) field has been breathtaking. As one of the SSL devices, the research in Light Emitting Diode (LED) has been actively undertaken by many research groups around the world. The development of LEDs has been associated with applications such as light source communications, medical instruments, sensors, display and lighting. Being small, reliable, bright, cheap, and efficient are the properties of state-of the art LEDs [1].

The discovery of the LED began in 1907 by Henry Joseph Round at Marconi Labs using SiC crystal. He published his note with the title A Note on Carborundum in the Electrical Word publisher. In 1927, a Russian researcher, Oleg Vladimirovich Losev, published his first research paper on the SiC diode emission in Journal of Wireless Telegraphy and Telephony (Thelegrafiya I Telefoniya bez Provodov) in Russia, scientific publications in British and German. After seven decades, a great improvement in visible light LED has been published by the Japanese researcher, Shuji Nakamura, in 1994. He fabricated InGaN/GaN based

LED chips which have a blue light emission [2][3][4][5].

Broadband emission light sources have been attracting many research groups to come up with LEDs structure. Various innovative designs have been proposed such as phosphor based white LEDs. However, phosphor based designs have disadvantages such as difficulty in fabrication, shorter lifetime, low reliability, Stokes shift energy loss, and low color rendering index. In order to overcome these problems, quantum design phosphor-free LEDs play an important role in this development.

1.1 Quantum Structure for LEDs

Based on particle confinement, material structures can be classified into four classes: bulk structure (three-dimensional structure), quantum well (two-dimensional structure), quantum wire (one-dimensional structure), and quantum dot (zero-dimensional structure) refer to Figure 1.1 [6].

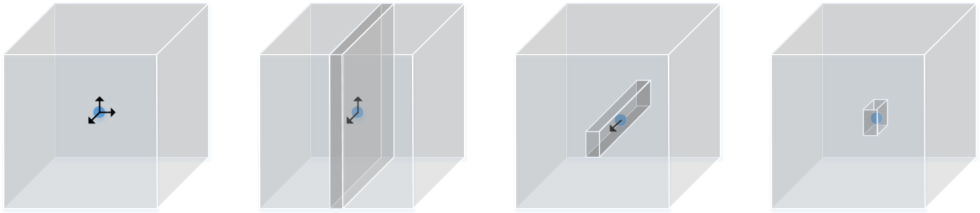

Figure 1.1: Material structures based on quantization of particle movement (bulk, quantum well, quantum wire and quantum dot).

Many quantum structures have been used to develop LEDs such as single quantum well (SQW) [7][8], multiple quantum well (MQW) [9][10][11][12], quantum dot (QD) [13] and quantum wire [14]. Recently, Wei Guo and co-workers proposed an LED structure design using InGaN based quantum disk embedded in a GaN nanowire [15]. Figure 1.2 (left) shows the realization of the quantum disk-in-nanowire (QD-NW). They also reported the ability of QD-NW structure to tune the emission wavelength. Figure 1.2 (right) shows the blue shift PL spectra of QD-NW structure with respect to InGaN nanowire.

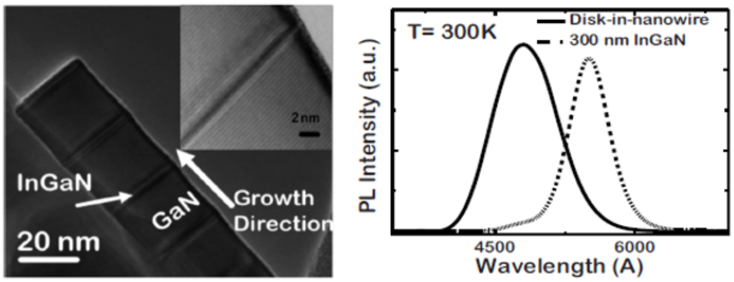

Figure 1.2: Realization of InGaN quantum disk in GaN nanowire (left) and blue shift photoluminescence (PL) spectra as an effect of quantum disk-in-nanowire [15].

1.2 Quantum Well Intermixing (QWI)

The intermixing process can occur because of concentration difference between heterogeneous materials. This phenomenon is very important in semiconductor devices especially heterojunction structures. Figure 1.3 illustrates the interdiffusion process in quantum well InGaN/GaN hetero-structures. Blur effects will occur at the interface due to the different of molecules concentration. This process is also well known as interface mixing or intermixing phenomenon.

By modeling the intermixing phenomenon, we can study particles motion in a Quantum Well (QW) that affects the properties of the quantum device such as band gap energy. In other words, by controlling the intermixing phenomenon, we

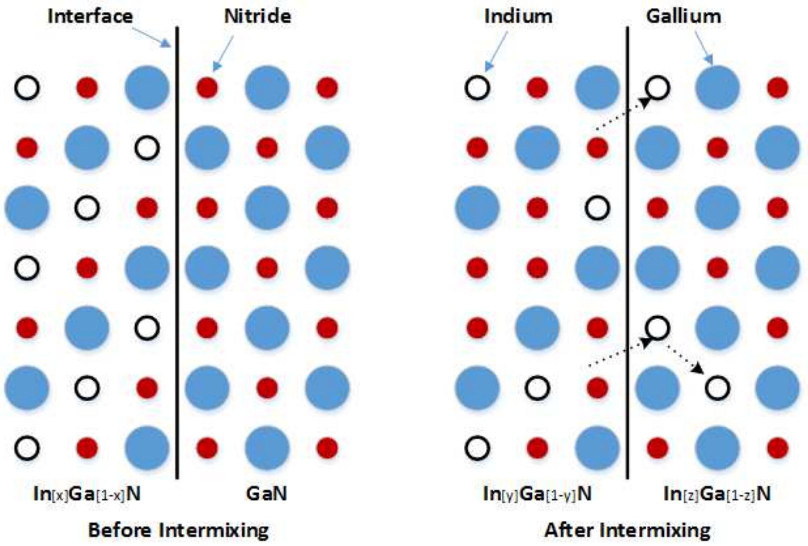

Figure 1.3: Illustration of intermixing phenomenon at InGaN/GaN interface.

will be able to tune the emission wavelength since it is related to band gap energy as shown in Figure 1.4.

There are three methods to induce Quantum Well Intermixing (QWI). The first is using ion implantation technique. It uses direct injection of ionized, molecules or energy atoms into a solid. The impurity species, such as Zn, S, Ge and Si, are used to enhance the intermixing process [16]. Figure 1.5 shows the intermixing process in QW by ion implantation technique.

The second technique is Impurity Free Vacancy Diffusion (IFVD). IFVD can be done by depositing an oxide capping layer on selected areas of the QW structure. This cap is used to promote concentration difference so that some particles or molecules, such as Ga atoms, in QW will be out-interdiffused to the cap as can be seen in Figure 1.6. Many types of capping have been used to enhance QWI such as SiO2, Si3N4 and TiO2 [16] [17] [18] [19].

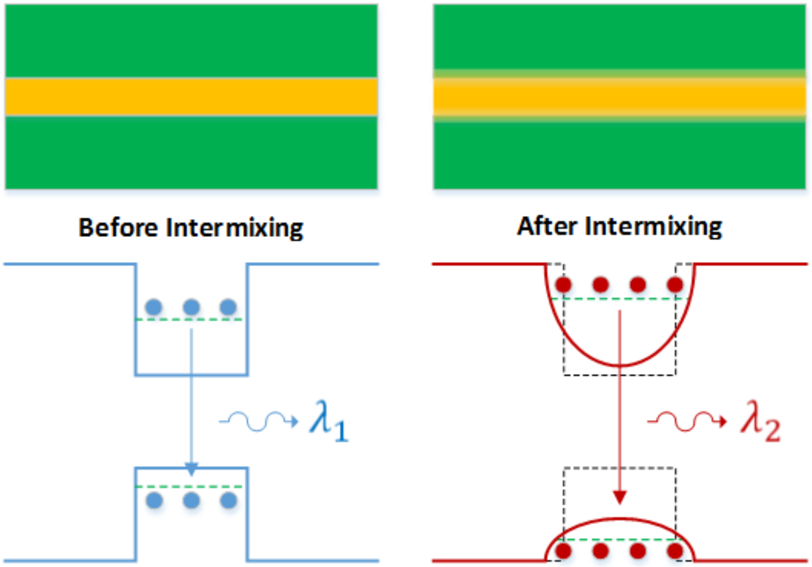

Figure 1.4: QWI affects the emission wavelength.

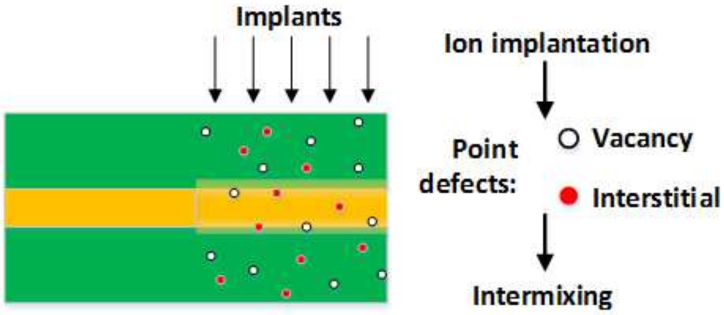

Figure 1.5: Enhancing QWI using ion implantation.

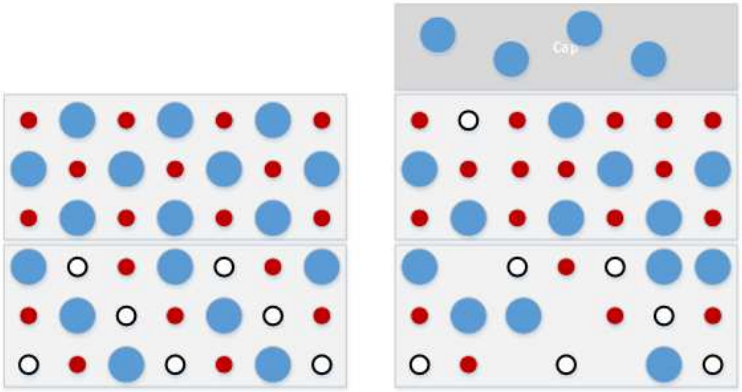

Figure 1.6: Enhancing QWI using ion implantation.

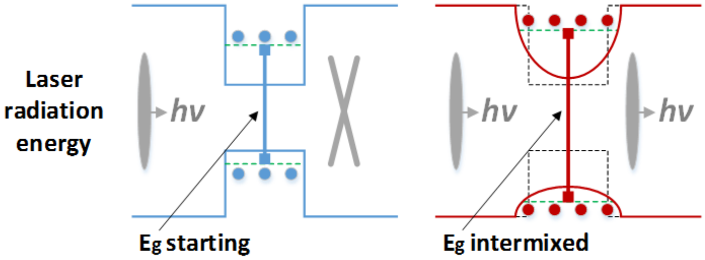

Figure 1.7: Laser radiation technique for QWI.

The third method is laser induced intermixing. This method uses direct laser radiation to promote the intermixing process. Incident continuous wave laser radiation is applied within the active domain of the structure. It leads to generation of heat that causes QWI. A high-power pulsed laser can also be used to increase the point defect density that will lead to QWI. Figure 1.7 shows the QWI process induced by a pulsed laser. This technique has been shown to be effective for $AlGaAs/GaAs$ QWI and $InGaAs/InGaAsP$ QWI [16].

1.3 Literature Review

Broadband and multiple wavelength emissions of light emitting diodes have been developed by many research groups. The use of various quantum structures is the key to this development. Nakamura and co-workers used SQW to produce high-brightness yellow, green, and blue emission LEDs. The structure design is shown in Figure 1.8(a). They reported that the green emission of their fabricated InGaN LED is brighter than conventional $AlInGaP$ and GaP LEDs [7]. In another report, a research group from Hong Kong led by K. M. Lau used InGaN/GaN based MQW with different QW widths as shown in Figure 1.8(b) to construct LEDs that have dual emission wavelength (blue and green). They reported that shifting the emission wavelength from blue to green color region is achieved by increasing driving current [9]. Quantum dot based LEDs have been developed by Pallab Bhattacharya and his research group at Center of Nanoscale Photonics and Spintronics, University of Michigan, Ann Arbor. They experimentally demonstrated self-organized InGaN/GaN QDs green light emission LED with internal quantum efficiency up to 32%. Figure 1.8(c) illustrates the design of their structure. They also reported that the quantum dots can reduce efficiency droop [13].

Another promising quantum based structure is the QD-NW LEDs. Hon-Way Lin et.al. reported a white LED based on $InGaN$ quantum disk growth on GaN nanorod. They introduced this structure to overcome problems of the conventional $GaN/InGaN$ quantum well based LED such as lattice-mismatched polar InGaN quantum well. It allows for efficient long-wavelength operation beyond the blue area due to strong Quantum Confined Stack Effect (QCSE). They showed an easy way to tune the emission wavelength by changing the injection current [17]. Similar work has been done by Pallab Bhattacharya and co-workers by demonstrating white LEDs based on $GaN/InGaN$ QD-NW grown on (001) Si substrates as shown in Figure 1.8(d). They showed a broad-emission produced by integrating varying alignment $InGaN$ quantum disks along the nanowires. By tuning the composition of the $GaN/InGaN$ QD-NW, they were able to obtain multi-

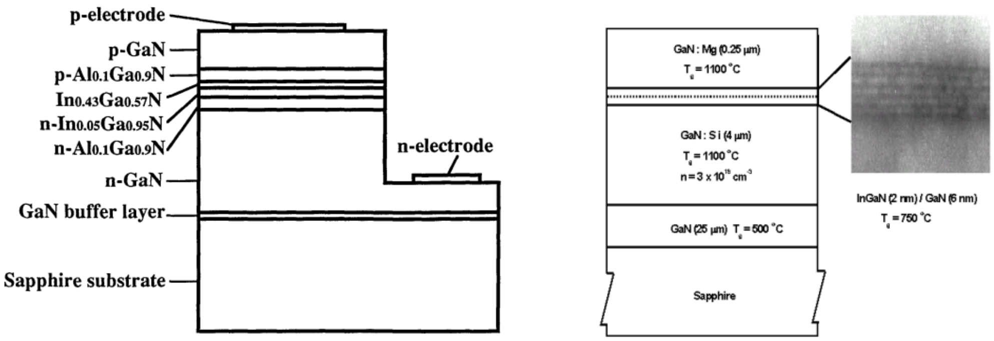

(a) SQW [7]

(b) MQW [10]

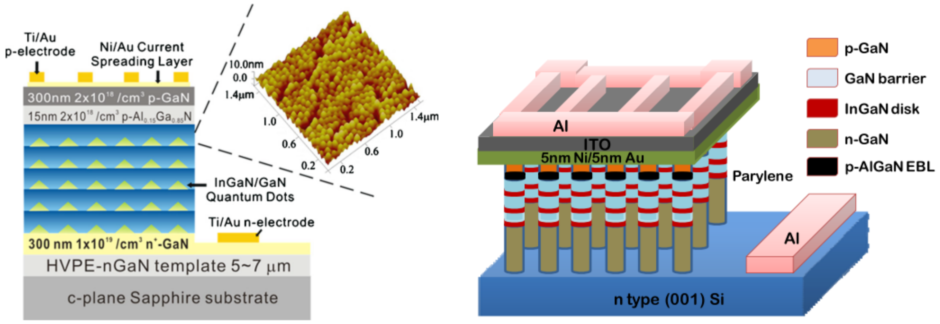

(c) Quantum dots in quantum well [13]

(d) Disk-in-nanowire [18]

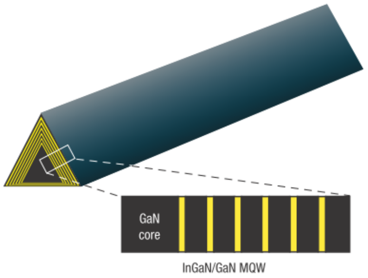

(e) MQW in triangular nanowire [20]

Figure 1.8: Various quantum based structures for LEDs.

wavelength emission with no efficiency rollover in the output [18]. The benefits of utilizing GaN-based QD-NW as building block to construct LEDs are

- Self-growth ability of Ga(In)N nanowires on Si substrate.
- Extended defect free such as twins, dislocation and stacking faults.
- Surface recombination velocity of GaN nanowires is smaller than that on the surface of GaAs.

Quantum well intermixing has been widely utilized in engineering quantum structures. The idea is to reform the quantum well shape by partial atom interdiffusing at the interface between the well and barrier [16] [21] [22]. Understanding intermixing phenomenon is much needed in designing LEDs based on quantum structure due to the nature of the hetero-structure. The graded quantum well after intermixing process modifies the characteristic of the material such as band profile. Much research work has been conducted to study the occurrence of intermixing phenomena in quantum heterostructure as well as its effect on the structure. Various materials have also been successfully used as media to study intermixing effects such as GaAs, InP, and GaN [23] [24] [25] [26].

The investigation of a tunable energy shape of Double Quantum Well (DQW) structure has also been conducted in [19]. Theoretically, diffusion equation is considered to model Al interdiffusion into a DQW structure. The demonstration of impurity free vacancy interdiffusion technique to induce the QWI has also been presented by introducing SiO_2 and SrF_2 caps to tune the energy shape of DQW as shown in Figure 1.9. After annealing treament at 930 ^oC for 30 s, DQW capped by SiO_2 gave a huge change to the energy shape compared to the original DQW. Compared to $SiO_2 + SrF_2$ cap, the interdiffusion coefficient is 53 times higher [19]. M. D. McCluskey and co-workers have observed intermixing phenomenon in $GaN/InGaN$ MQWs for annealing temperatures 1300-1400 ^oC . They reported that after annealing $GaN/In_{0.18}Ga_{0.82}N$ MQWs at temperature of 1400 ^oC for 15 minutes, the MQW region is replaced by a uniform $InGaN$ layer [21].

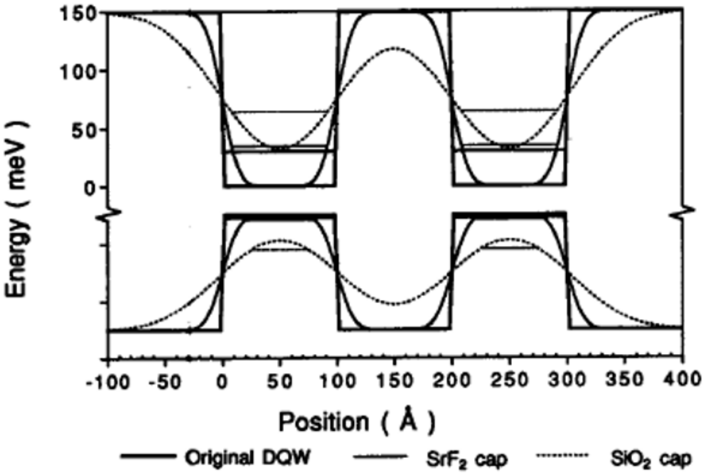

Figure 1.9: Shape of original square DQW compared to DQW capped with SrF_2+SiO_2 and with SiO_2 only [22].

It will be interesting to study the effect of intermixing phenomenon on the quantum behavior in QD-NW based LED structures. Numerical simulation as an approach to investigate the phenomenon should be able to solve incorporated equations such as Schrodinger, diffusion, and band gap energy equations. Many researchers have been working to solve the quantum part. Munteanu and Autran built a steady-state Schrodinger equation solver using Hamiltonian matrix method for a nanowire MOSFET [27]. They got good validation of the simulation results compared to commercial package software named Silvaco. Finite-difference time-domain (FDTD) method has been applied by D. M. Sullivan to find eigen energies and eigen function [28][29]. In this work we will consider the FDTD method for solving the equations, including diffusion. To the best of our knowledge this problem has not been analyzed yet for QD-NW structure.

1.4 Thesis Objectives

The main contribution of this thesis is to develop a model representing the quantum behavior of $GaN/InGaN$ QD-NW through the study of the effects of intermixing. The model is numerically solved using the Q-FDTD solver. The specific objectives are as follows.

1. To perform a comprehensive literature review on the quantum behavior associated with QD-NW LED structures.
2. To develop interdiffusion equation of QD-NW band diagram representing intermixing phenomenon in QD-NW LED structure.
3. To formulate Q-FDTD equation representing the Schrodinger equation for QD-NW structure.
4. To couple the Q-FDTD with the interdiffusion equation related to QD-NW LED structure in a multi-dimensional setup.
5. To study and analyze different parameters that characterizes the behavior of QD-NW structures.

6. To extract important conclusions regarding the intermixing phenomenon effects and their applications.

1.5 Methodology

There are three major models which are solved and link to the QFDTD numerical solver. The specific methodology is as follows.

1. Construct one dimensional QFDTD solver to generate eigen energies and eigen function from Schrödinger equation for a given potential energy distribution.
2. Construct one dimensional heterogeneous Poisson solver to get the distribution of electrostatic voltage due to polarization effects.
3. Construct one dimensional Fickian interdiffusion model solver both for constant interdiffusion coefficient and concentration dependence interdiffusion coefficient to get the concentration distribution after intermixing process.
4. Combine the three one dimensional solvers.
5. Find the model of interdiffusion coefficient that depends on the concentration according to experimental data and analyze the result.
6. Expand the work to three dimensional cases.

1.6 Thesis Organization

The thesis is organized as the following.

Chapter 1 contains introduction about broadband emission GaN based LED, Quantum Disk-in-Nanowire (QD-NW) structure and its benefits, QWI and several methods to enhance QWI, thesis objectives and organization.

Chapter 2 contains fundamental theory needed to understand the topic of the thesis. It explains the preliminary background of intermixing phenomenon based on Fick's laws, Poisson equation, Schrodinger equation and computational analysis for Partial Differential Equation (PDE) such as discretization schemes, consistency, stability and convergence.

Chapter 3 presents the model for intermixing process in QD-NW structure using Fickian interdiffusion model including the interdiffusion coefficient. It also describes the polarization models both for spontaneous and piezoelectric polarizations and determination of eigen energy and eigen function as quantum properties.

Chapter 4 presents the Quantum Finite Difference Time Domain (Q-FDTD) solver for interdiffusion, polarization and quantum properties models. It also contains the detail of computational analysis.

Chapter 5 presents the simulation of one dimensional intermixing process in $GaN/InGaN$ QD-NW including the parametric studies.

Chapter 6 presents the simulation of three dimensional intermixing process in $GaN/InGaN$ QD-NW including the parametric studies.

Chapter 7 summarizes and discusses, determines the contributions of the thesis and gives conclusions with suggestions for possible extension for future work.

CHAPTER 2

THEORETICAL BACKGROUND

The phenomena of intermixing in solid nanostructure has been widely studied. Many theories have been published to determine the process. In this chapter the basic theory of intermixing phenomena is presented using Fick's second law as a formulation to describe the interdiffusion process, general Poisson equation as an introduction for polarization effects model and Time dependent Schrödinger equation as a representative of quantum states. The computation analysis background for partial differential equation is also conducted in this chapter including discretization analysis, consistency, stability criteria and convergence.

2.1 Fick's Second Law

Diffusion is a process which tends to produce an equalization of concentrations within a given structure. The diffusion law correlates the flow rate of the diffusing matter with the concentration gradient [30]. Adolf Eugen Fick modeled the relation between the diffusion flux of a matter with the concentration in a formulation known as Fick's First Law which is expressed as

$$J = -D\nabla c(\mathbf{r}) \tag{2.1}$$

where

- J is the diffusion flux or the quantity of matter per unit area.
- D is the diffusion coefficient.
- c is the concentration.
- $\mathbf{r}$ is the space vector variable.
- ∇ is the gradient operator.

Generally, it is impossible to investigate diffusion process under conditions of steady state concentration gradient. However, A. E. Fick determined a new relation that accounts for the change of concentration with time as formulated in the following equation

$$\frac{\partial c(t,\mathbf{r})}{\partial t} = D\Delta\big(c(t,\mathbf{r})\big) \tag{2.2}$$

where

- t is the time vector variable.
- Δ is the Laplace operator (equivalent to ∇^2).

which is Fick's Second Law or non-steady state diffusion equation, derived on the assumption that D is constant or independent of matter's concentration [31].

This assumption is not generally valid. However, the correct representation that accounts the dependency of D on concentration is derived as

$$\frac{\partial c(t,\mathbf{r})}{\partial t} = \nabla . \Big(D(c) \nabla c(t,\mathbf{r}) \Big) \tag{2.3}$$

2.2 Poisson Equation

In order to determine the effects of polarization that occur in the GaN-based QD-NW, the heterogeneous Poisson equation of electrostatic voltage is considered. In numerical studies, Poisson equation is classified as Elliptic Partial Differential Equation. Generally, it can be written as

$$\Delta\phi = \nabla^2\phi = f \tag{2.4}$$

where ϕ and f are complex or real functions. It turns into Laplace equation if f is determined as zero. Poisson equation is simply the non-homogeneous Laplace equation. The existence of non-homogeneous term f can overly constrict the analytical solution of the Poisson equation. However, it does not constrict the numerical solution.

In three and one dimensional Cartesian coordinates, Poisson equation can be written respectively as

$$\left(\frac{\partial^2}{\partial \mathbf{x}^2} + \frac{\partial^2}{\partial \mathbf{y}^2} + \frac{\partial^2}{\partial \mathbf{z}^2} \right) \phi(\mathbf{x},\mathbf{y},\mathbf{z}) = f(\mathbf{x},\mathbf{y},\mathbf{z}) \tag{2.5}$$

and

$$\left(\frac{\partial^2}{\partial \mathbf{x}^2}\right)\phi(\mathbf{x}) = f(\mathbf{x}) \tag{2.6}$$

Numerically, Poisson equation can be solved by direct technique, e.g. Gauss elimination, or an iterative technique, e.g. Jacobi iteration, Gauss-Seidel iteration and Successive Over Relaxation (SOR). However, the direct technique requires larger computational efforts, e.g. computer memory and computation time, than iterative technique because the direct technique calculates all elements in the calculation domain unlike iterative technique uses only the nonzero elements.

2.3 Time Dependent Schrödinger Equation

In the year of 1926, an Austrian physicist, Erwin Schrödinger, introduced a mathematical model to represent how the quantum state changes with time which is then called Schrödinger Equation. It is in the form of time dependent parabolic PDE which is formulated as

$$i\hbar\frac{\partial\psi(t,\mathbf{r})}{\partial t} = \Big(-\frac{\hbar^2}{2m}\nabla^2 + U(\mathbf{r})\Big)\psi(t,\mathbf{r}) \tag{2.7}$$

where

- ψ is the wave function of the quantum state.
- U is the potential energy.
- m is the effective mass of the carrier.

- $\hbar$ is the reduced Planck's constant ($\hbar = \frac{h}{2\pi}$).

In this thesis, Time-Dependent Schrödinger Equation (TDSE) is solved to generate quantum properties, eigen energies and eigen functions, of the nano-structure.

2.4 Computational Analysis for Finite Difference Equations

Many famous numerical techniques have been widely used to solve PDE problems such as Finite Difference Method (FDM), Finite Element Method (FEM), Finite Volume Method (FVM), Method of Lines (MOL) and Spectral and Meshfree Methods. In this thesis finite difference method is considered as building block solver. There are several important aspects of finite difference based solver that have to be considered.

2.4.1 Discretization Schemes

Discretization describes the process of transferring continuous into discrete functions. In finite difference technique, there are several discretization schemes that can be used to generate Finite Difference Equation (FDE), e.g. forward, backward and central differencing schemes. Table 2.1 tabulates several examples of finite difference schemes, approximation formulas and stencils for single and multiple variables PDE, $\dfrac{\partial \phi(\mathbf{x})}{\partial \mathbf{x}}$ and $\dfrac{\partial^2 \phi(t,\mathbf{x})}{\partial t \partial \mathbf{x}}$. The FS, BS, CS, FTCS and CTCS notations in the table stand for forward differencing in space domain (or forward in space), backward in space, central in space, forward in space and central in time and central in space and central in time.

2.4.2 Consistency

The numerical consistency of FDE is determined by the truncation error between FDE and PDE. It is consistent if the error goes to zero as the grid size approaches zero. A well-known technique to analyze the consistency of FDE has been introduced by Warming and Hyett. Each term of Modified Differential Equation (MDE), i.e. the actual PDE, is expressed in a FDE in a Taylor series. By letting the grid size go to zero, the FDE converges back to PDE. The detail can be observed from the following example.

Consider the two dimensional Laplace equation,

$$\frac{\partial^2 \phi(\mathbf{x})}{\partial \mathbf{x}^2} + \frac{\partial^2 \phi(\mathbf{y})}{\partial \mathbf{y}^2} = 0 \tag{2.8}$$

and central space discretization scheme, Equation 2.8 can be approximated as

$$\phi(i+1,j) + \phi(i-1,j) + \phi(i,j+1) + \phi(i,j-1) - 4\phi(i,j) = 0 \tag{2.9}$$

The Taylor series of $\phi(i \pm 1, j)$ and $\phi(i, j \pm 1)$ are

$$\begin{aligned} \phi(i \pm 1, j) = \phi(i,j) \pm \Delta\mathbf{x}\frac{\partial \phi(\mathbf{x})}{\partial \mathbf{x}} + \frac{1}{2}\Delta\mathbf{x}^2\frac{\partial^2 \phi(\mathbf{x})}{\partial \mathbf{x}^2} \pm \\ \frac{1}{3!}\Delta\mathbf{x}^3\frac{\partial^3 \phi(\mathbf{x})}{\partial \mathbf{x}^3} + \frac{1}{4!}\Delta\mathbf{x}^4\frac{\partial^2 \phi(\mathbf{x})}{\partial \mathbf{x}^4} \pm ... \end{aligned} \tag{2.10}$$

Table 2.1: Finite Difference Schemes Stencils

Scheme	Approximation	Stencil
FS	$\frac{\partial\phi(\mathbf{x})}{\partial\mathbf{x}} \approx \frac{\phi(i+1)-\phi(i)}{\Delta\mathbf{x}}$	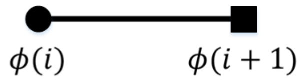
BS	$\frac{\partial\phi(\mathbf{x})}{\partial\mathbf{x}} \approx \frac{\phi(i)-\phi(i-1)}{\Delta\mathbf{x}}$	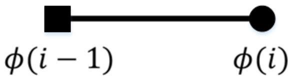
CS	$\frac{\partial\phi(\mathbf{x})}{\partial\mathbf{x}} \approx \frac{\phi(i+1)-\phi(i-1)}{2\Delta\mathbf{x}}$	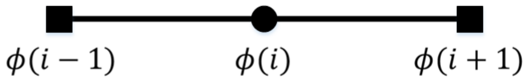
FTCS	$\frac{\partial\phi(\mathbf{t})}{\partial\mathbf{t}} \approx \frac{\phi^{n+1}(i)-\phi^{n}(i)}{\Delta\mathbf{t}}$; $\frac{\partial\phi(\mathbf{x})}{\partial\mathbf{x}} \approx \frac{\phi(i+1)-\phi(i-1)}{2\Delta\mathbf{x}}$	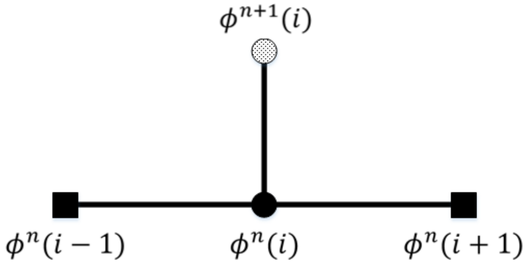
CTCS	$\frac{\partial\phi(\mathbf{t})}{\partial\mathbf{t}} \approx \frac{\phi^{n+1}(i)-\phi^{n-1}(i)}{2\Delta\mathbf{t}}$; $\frac{\partial\phi(\mathbf{x})}{\partial\mathbf{x}} \approx \frac{\phi(i+1)-\phi(i-1)}{2\Delta\mathbf{x}}$	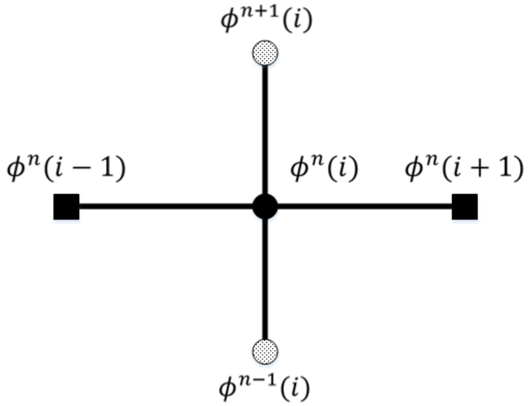

$$\begin{aligned}\phi(i,j\pm 1) = \phi(i,j) \pm \Delta\mathbf{y}\frac{\partial\phi(\mathbf{y})}{\partial\mathbf{y}} + \frac{1}{2}\Delta\mathbf{y}^2\frac{\partial^2\phi(\mathbf{y})}{\partial\mathbf{y}^2} \pm \\ \frac{1}{3!}\Delta\mathbf{y}^3\frac{\partial^3\phi(\mathbf{y})}{\partial\mathbf{y}^3} + \frac{1}{4!}\Delta\mathbf{y}^4\frac{\partial^2\phi(\mathbf{y})}{\partial\mathbf{y}^4} \pm ...\end{aligned} \tag{2.11}$$

Inserting Equation 2.10 and 2.11 in Equation 2.9 will produce

$$\frac{\partial^2\phi(\mathbf{x})}{\partial\mathbf{x}^2} + \frac{\partial^2\phi(\mathbf{y})}{\partial\mathbf{y}^2} = \left(\frac{2}{4!}\Delta\mathbf{x}^2\frac{\partial^2\phi(\mathbf{x})}{\partial\mathbf{x}^2} + \frac{2}{4!}\Delta\mathbf{y}^2\frac{\partial^2\phi(\mathbf{y})}{\partial\mathbf{y}^4} + ...\right) \tag{2.12}$$

and letting $\Delta\mathbf{x}$ and $\Delta\mathbf{y}$ go to zeros, it will end up to be Equation 2.8 which is the original PDE. Consequently, Equation 2.9 is a consistent FDE of the Laplace equation.

2.4.3 The von Neumann Stability Analysis

The matter of stability in computation of PDE is pervasive. The general behavior of the exact solution of PDE has to be considered. The numerical solution is unstable if the PDE has instability. However, the concept of stability can only be applied in the case when the PDE itself is stable.

There are several methods that can be utilized to analyze the stability of a FDE such as the matrix method, the discrete perturbation method and the von Neumann method which is considered in this work. The idea of the von Neumann stability analysis is similar to Fourier method. It considers the growth of individual Fourier component, i.e. wave $\exp(ikx)$, of the FDE. The FDE is stable if the solution of the general Fourier component is bounded either unconditionally or conditionally. In order to maintain the stability of computation, the following condition has to be considered

$$|G(\theta)| \leq 1 \ \forall\theta \tag{2.13}$$

where G is the growth or amplification factor defined from $\phi^{n\pm1}(i) = G^{\pm1}\phi^{n}(i)$ and $\theta = k\Delta r$ where k is the wave number. Figure 2.1 shows the stability region of the growth factor.

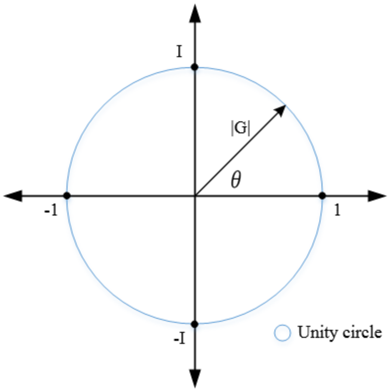

Figure 2.1: Unit circle of $|G(\theta)| \leq 1$

As an example, let us consider Fick's Second Law with constant diffusion coefficient,

$$\frac{\partial c(t,\mathbf{x})}{\partial t} = D\frac{\partial^2 c(\mathbf{x}^2)}{\partial \mathbf{x}^2} \tag{2.14}$$

Using FTCS differencing scheme, the FDE is determined as

$$\frac{c^{n+1}(i) - c^{n}(i)}{\Delta t} = D\frac{c^{n}(i+1) - 2c^{n}(i) + c^{n}(i-1)}{\Delta \mathbf{x}^2} \tag{2.15}$$

$$c^{n+1}(i) = c^{n}(i) + D\frac{\Delta t}{\Delta \mathbf{x}^2}\Big(c^{n}(i+1) - 2c^{n}(i) + c^{n}(i-1)\Big) \tag{2.16}$$

Applying the definition of growth factor, Equation 2.16 is transfered to

$$G(\theta)c^n(i) = c^n(i) + D\frac{\Delta t}{\Delta \mathbf{x}^2}\Big(c^n(i)e^{i\theta} - 2c^n(i) + c^n(i)e^{-i\theta}\Big) \tag{2.17}$$

$$G(\theta) = 1 + D\frac{\Delta t}{\Delta \mathbf{x}^2}\Big(e^{i\theta} - 2 + e^{-i\theta}\Big) \tag{2.18}$$

$$G(\theta) = 1 - 2D\frac{\Delta t}{\Delta \mathbf{x}^2}\Big(1 - \cos(\theta)\Big) \tag{2.19}$$

Applying the condition mentioned in Equation 2.13, the stability condition of Equation 2.15 is

$$\big|G(\theta)\big| = \left|1 - 2D\frac{\Delta t}{\Delta \mathbf{x}^2}\Big(1 - \cos(\theta)\Big)\right| \leq 1 \tag{2.20}$$

The worst case of Equation 2.20 is when $\theta = \pi$. It leads to

$$\big|G(\theta)\big| \leq \left|1 - 4D\frac{\Delta t}{\Delta \mathbf{x}^2}\right| \leq 1 \tag{2.21}$$

$$\Delta t \leq \frac{\Delta \mathbf{x}^2}{2D} \tag{2.22}$$

2.4.4 Convergence

The Lax equivalence theorem states: "Given a properly posed linear initial-value problem and a finite difference approximation to it that is consistent, stability is the necessary and sufficient condition for convergence". It means that by knowing the consistency and stability of the FDE directly defines the convergence.

CHAPTER 3

MODELING OF INTERMIXING PROCESS IN QD-NW

This chapter shows all assumptions and related models in intermixing process and its effects on emission properties in QD-NW. Considering $InGaN/GaN$ based QD-NW, intrinsic properties of binary systems, GaN and InN, are provided such as lattice constants and dielectric functions. Moreover, three primary models: interdiffusion model as representation of intermixing process, polarization effects model and quantum properties model that provides eigen energy and eigen function, are explained in detail. The chapter also discusses the assumption of indium atom distribution in as grown structure in relation to the nanostructure fabrication processes.

3.1 Atomic Distribution in As Grown Structure

Precision is one of the biggest issues in nanostructures fabrications. Accurate fabrication of nanometer-scale structures has underpinned fascinating inventions across a wide range of scientific disciplines. Many fabrication techniques have been developed in order to bring out perfect structures. There are two approaches in nanostructures fabrication, bottom-up and top-down methods. The bottom-up method, well-known as self-assembly method, uses atoms or molecules or nanoparticles as building blocks to construct a larger structure. Generally, it needs essentially highly controlled machines and complex chemical syntheses. The top-down method is the opposite of the self-assembly approach. The process starts from a large piece and subsequently uses finer tools to create smaller forms.

However, there are still many imperfections in fabrications process that affect the result. The evidences can be found by analyzing Transmission Electron Microscopy (TEM) images. As an example, Figure 3.1 shows the as grown structure of $GaN/InGaN$ quantum well that is not purely discontinues at the interface between GaN barrier and $InGaN$ well. The change of indium concentration is more like gradual increase with distance rather than step-like change. In this work, we consider a trapezoidal quantum well as the as-grown structure with variation of trapezoidal ramp slopes as shown in Figure 3.2.

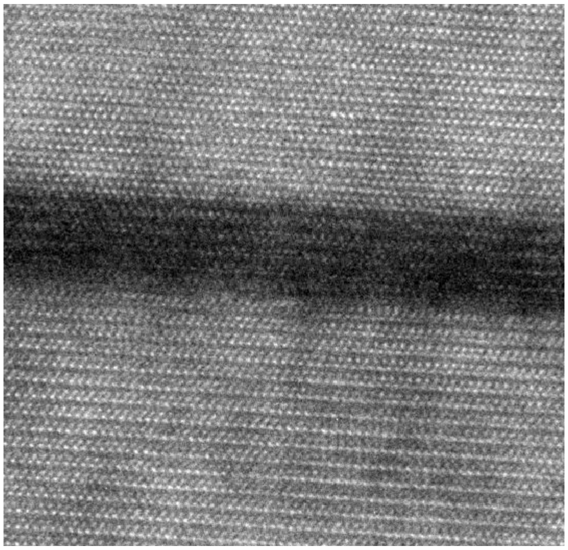

Figure 3.1: TEM image of as grown quantum well (KAUST Photonics Lab.).

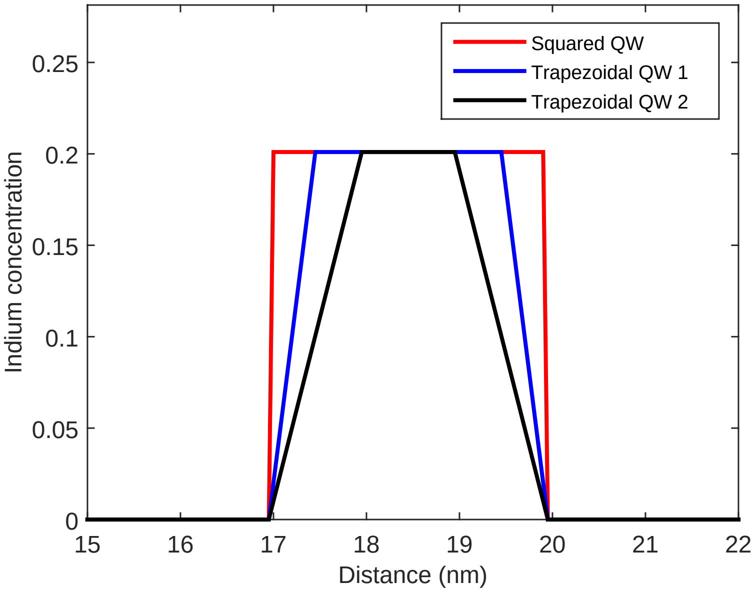

Figure 3.2: Variation of as grown quantum well shapes.

3.2 Polarization Effect Model

Considering the polarization charges in III-Nitride semiconductor devices is tremendously important. The built-in polarization charges of material contributes to the change of electric potential, the band edge and carrier energy. This can be formulated in Poisson's equation for electrostatic as

$$\nabla.\Big(\epsilon(\mathbf{r})\nabla V(\mathbf{r})\Big) = -\rho_f(\mathbf{r}) = -q\Big(p(\mathbf{r}) - n(\mathbf{r}) - N_A^-(\mathbf{r}) + N_D^+(\mathbf{r})\Big) \tag{3.1}$$

where

- p and n are the hole and electron density, respectively, in m^{-3}.
- N_A and N_D are ionized acceptor and donor impurity concentrations,respectively, in m^{-3}.
- ϵ is the dielectric constant.
- q is the electron charge in C (coulombs).
- V is the electrostatic potential in V (volt).

Accounting for the effects of polarizations, Equation 3.1 can be modified as

$$\nabla.\Big(\epsilon(\mathbf{r})\nabla V(\mathbf{r})\Big) = -q(p(\mathbf{r}) - n(\mathbf{r}) - N_A^-(\mathbf{r}) + N_D^+(\mathbf{r}) \mp N_f(\mathbf{r})) = -\rho(\mathbf{r}) \tag{3.2}$$

where N_f is the fixed interface charge density in m^{-3} defined as

$$qN_f(\mathbf{r}) = \nabla.P(\mathbf{r}) \tag{3.3}$$

and P is the total built-in polarization defined as

$$P(\mathbf{r}) = P_{sp}(\mathbf{r}) + P_{pz}(\mathbf{r}) \tag{3.4}$$

where

- P_{sp} is the spontaneous polarization in Cm^{-2}.
- P_{pz} is the piezoelectric polarization in Cm^{-2}.

For an unbiased device, Equation 3.2 can be rewritten as

$$\nabla.\Big(\epsilon(\mathbf{r})\nabla V(\mathbf{r})\Big) = \pm\nabla.P(\mathbf{r}) \tag{3.5}$$

As we can observe, the spatial dielectric function should be determined due to inhomogeneous structures. The dielectric function of $In_xGa_{1-x}N$ alloys used in this thesis is based on curve fitting from the curves in [32] [33] as shown in Figure 3.3 where several curves are vertically shifted by the numbers next to the graphs.

The curves fitting of the experimental data is shown in Figure 3.4 based on Least Square Method (LSM). The three fitted mathematical models are in Equation 3.6, 3.7 and 3.8. ϵ_{fit2} is considered in this thesis due to its higher fitting

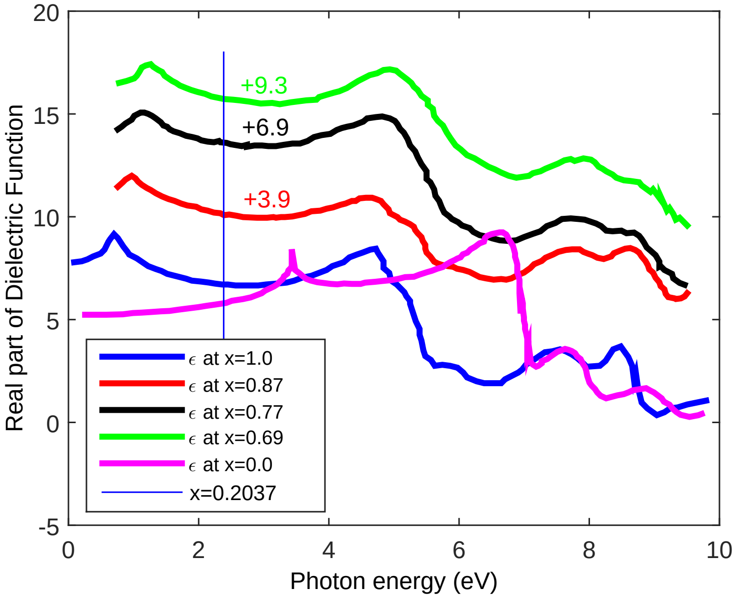

Figure 3.3: Real part of dielectric function spectra of $In_xGa_{1-x}N$ alloys for several x values.

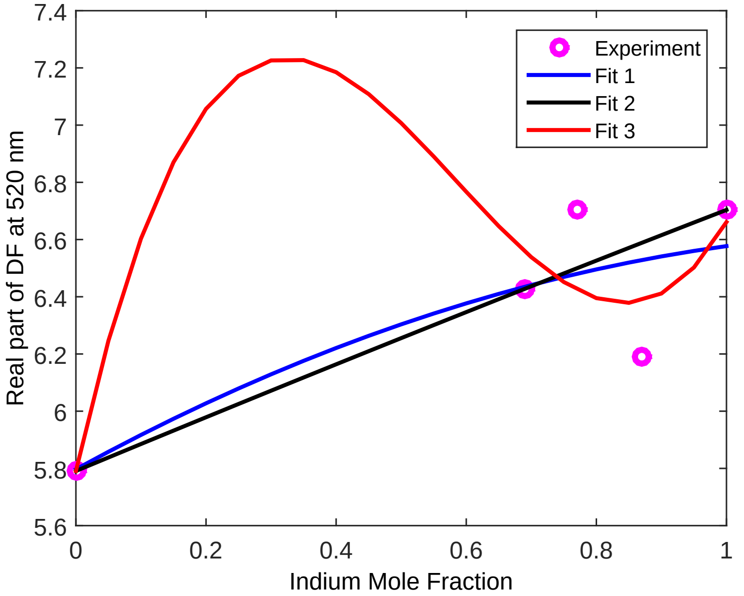

Figure 3.4: Real part of dielectric function spectra of $In_xGa_{1-x}N$ alloys for several x values.

parameter and the lowest error.

$$\epsilon_{fit1}(x) = -0.4659x^2 + 1.246x + 5.797 \tag{3.6}$$

$$\epsilon_{fit2}(x) = -0.03236x^2 + 0.945x + 5.791 \tag{3.7}$$

$$\epsilon_{fit3}(x) = 12.33x^3 - 21.62x^2 + 10.16x + 5.791 \tag{3.8}$$

Both built-in polarization fields, spontaneous and piezoelectric polarizations, are much stronger in c-plane GaN-based structures than in other III-N compounds. The investigation of this properties have been extensively done theoretically and experimentally. Moreover, analytical approximations have been derived for computing the built-in polarization in the form of nonlinear equations. The detail explanations are derived in the following.

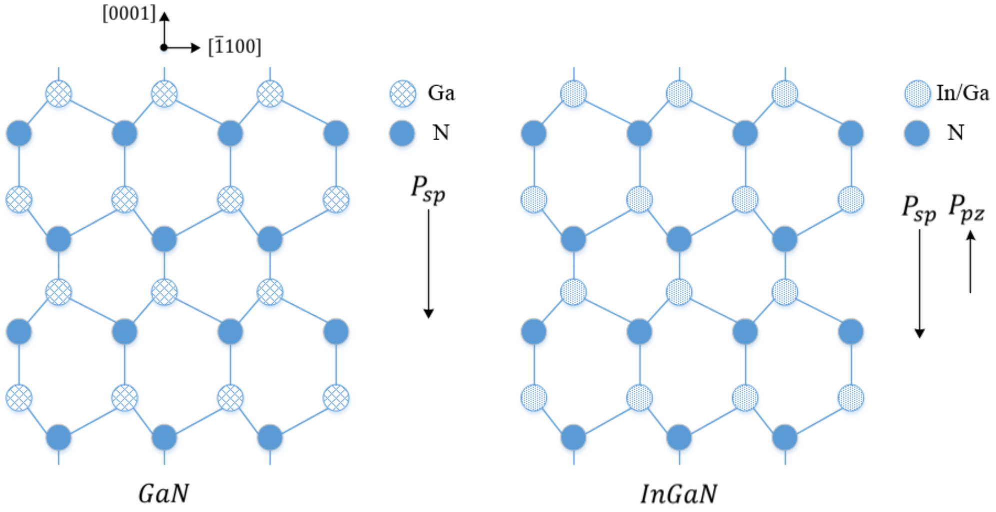

Figure 3.5: Spontaneous and piezoelectric polarization fields and crystal structure of GaN and $InGaN$ alloys.

3.2.1 Spontaneous Polarization

P_{sp} field is built-in electric polarization that obviously occurs in III nitrides but absents in many other familiar semiconductors utilized in optoelectronic devices. Two types of materials having a P_{sp} in nature are ferroelectrics and pyroelectrics materials.

Pyroelectricity usually occur in wurzite crystal structure such as in GaN, InN and AlN which have non-centrosymmetric structure and its axis is parallel to the [0001] direction as shown in Figure 3.5. The occurrence of pyroelectricity in wurzite structure as intrinsic property of material is due to the bonding mismatch i.e. the geometric center of the electrons does not concur with the center of the nuclei.

In $In_xGa_{1-x}N$ alloys, spontaneous polarization can be approximated using nonlinear formulation as follows

$$P_{sp}[In_xGa_{1-x}N] = xP_{sp}[InN] + (1-x)P_{sp}[GaN] + b_{P_{sp}}x(1-x) \tag{3.9}$$

where

- x is the indium concentration.
- $P_{sp}[GaN]$ is the spontaneous polarization of GaN, -0.0339 Cm^{-2}.
- $P_{sp}[InN]$ is the spontaneous polarization of InN, -0.0413 Cm^{-2}.
- $b_{P_{sp}}$ is the bowing parameter for $P_{sp}[In_xGa_{1-x}N]$, 0.0378 Cm^{-2}.

The negative signs in $P_{sp}[GaN]$ and $P_{sp}[InN]$ show that the P_{sp} vector is antiparallel to the [0001] direction.

3.2.2 Piezoelectric Polarization

In addition to P_{sp}, P_{pz} occurs due to strain induced along the *c*-axis in strained layer of wurzite structure. The contribution of P_{sp} is usually smaller than P_{pz} or inferior in $GaN/InGaN$ heterostructures.

In $In_xGa_{1-x}N$ alloys, P_{pz} can be calculated by indirect nonlinear equation as mentioned in Equation 3.10. The nonlinearity for P_{pz} does not come from bowing parameter like in P_{sp} but rather from the nonlinearity of the alloys individual binary constituents, i.e. $P_{pz}[GaN]$ and $P_{pz}[InN]$. Figure 3.6 shows the $P_{pz}[GaN]$, $P_{pz}[InN]$ and η_1 as functions of indium mole fraction.

$$P_{pz}[In_xGa_{1-x}N] = xP_{pz}[InN] + (1-x)P_{pz}[GaN] \tag{3.10}$$

$$P_{pz}[InN] = -1.373\eta_1 + 7.559\eta_1^2 \tag{3.11}$$

$$P_{pz}[GaN] = -0.918\eta_1 + 9.541\eta_1^2 \tag{3.12}$$

$$\eta_1 = \frac{x(a[GaN] - a[InN])}{xa[InN] + (1-x)a[GaN]} \tag{3.13}$$

where

- $P_{pz}[GaN]$ is the piezoelectric polarization of GaN in Cm^{-2}.
- $P_{pz}[InN]$ is the piezoelectric polarization of InN in Cm^{-2}.
- η_1 is the basal strain of the binary compound.

- $a[GaN]$ is the equilibrium lattice constant of the binary compound GaN, 3.1892 $\mathring{A}$.

- $a[InN]$ is the equilibrium lattice constant of the binary compound InN, 3.5380 $\mathring{A}$.

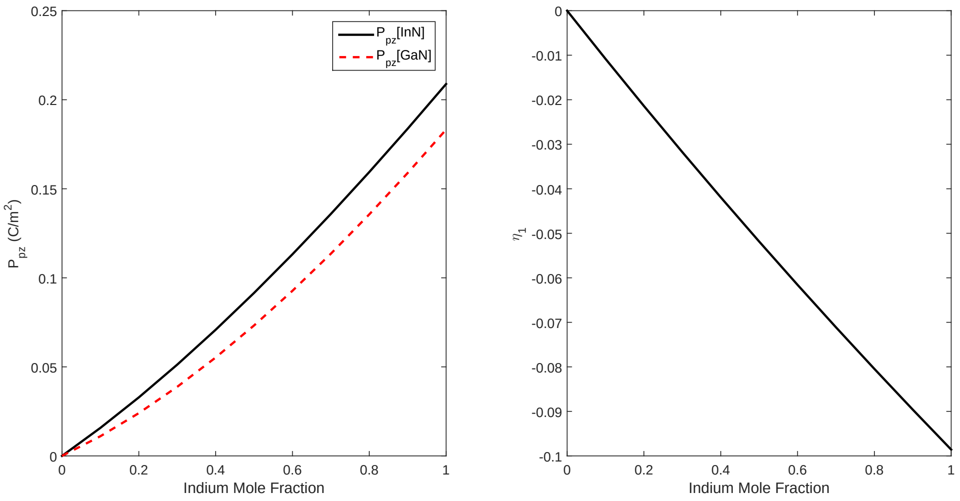

Figure 3.6: $P_{pz}[InN]$, $P_{pz}[GaN]$ (left) and η_1 or basal strain (right).

Figure 3.7 depicts the P_{sp} and P_{pz} of $In_xGa_{1-x}N$ based on Equation 3.9 and 3.10. Clearly, the P_{pz} influences more than P_{sp} on $In_xGa_{1-x}N$ heterostructures in all indium mole fractions.

3.3 Fickian Interdiffusion Model

The interdiffusion model used in this work is based on Fick's Second Law of diffusion, as mentioned in Chapter 2 in Equation 2.3. Phenomenological observations based on Fickian interdiffusion models are correct and acceptable for any atomic

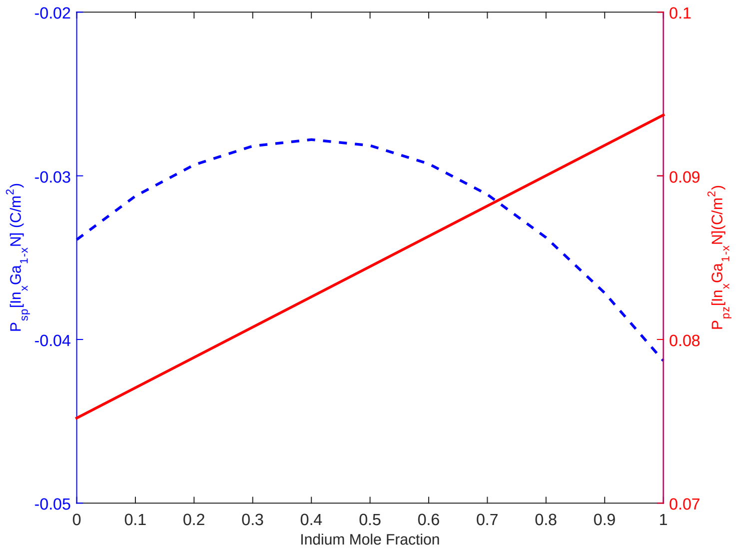

Figure 3.7: P_{sp} and P_{pz} of $In_xGa_{1-x}N$ for all indium mole fractions.

interdiffusion mechanism. The interdiffusion coefficient, D also called interdiffusivity, is a crucial material parameter to indicate the interdiffusion mobility. The higher interdiffusion coefficient of one substance with respect to another, the faster it interdiffuses.

The dependency of D on concetration has to be considered. Moreover, in terms of interdiffusion in solids, there are several parameters that can influence the D such as activation energy E_a and temperature T. Activation energy is the amount of energy that is needed by an atom to break bonds or jump to neighboring vacancy or interdiffuse. Figure 3.8 illustrates the interdiffusion activation energy as intrinsic parameter of material. Furthermore, each atom has average thermal energy as k_BT, where k_B is Boltzmann constant, and it is usually less than its E_a. Incorporating E_a and T in D, Equation 3.14 shows the Arrhenius form of interdiffusion coefficient.

$$D(T,c) = D_0(c)\exp\left(\frac{-E_a}{k_B T}\right) \tag{3.14}$$

where $D_0(c)$ is the concentration dependent prefactor interdiffusion coefficient.

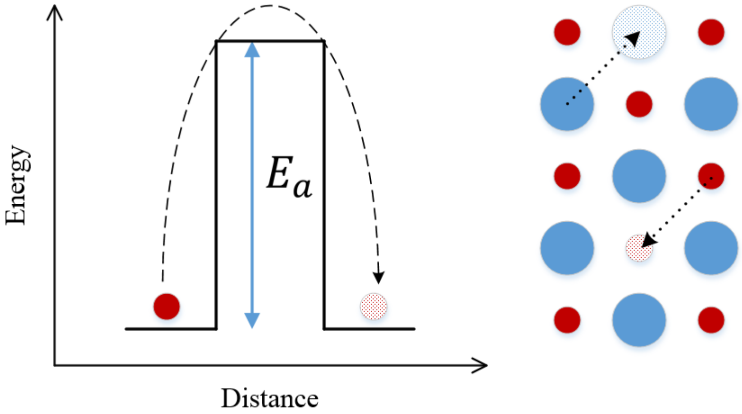

Figure 3.8: Schematic of activation energy of diffusing atom.

The definition of $D_0(c)$ is another challenge in this work. Considering experimental data in [25], LSM curve fitting and logarithmic-based linear interpolation, $D_0(c)$ is determined as

$$D_0(c) = D_2\exp(D_1 c) \tag{3.15}$$

where D_1 and D_2 are the fitting constants for the case of indium interdiffusion in $InGaN/GaN$ quantum wells with values 20.28571 m^3 and 7.9465e-11 m^2/s respectively. It also yields the E_a value as 3.639 eV.

The values of D_1 and D_2 are readjusted using experimental data of eigen energy shifting of $InGaN/GaN$ multiple quantum well (MQW) after annealing treatment at 950 ^oC for several variation times as shown in Figure 3.10. Data is provided by

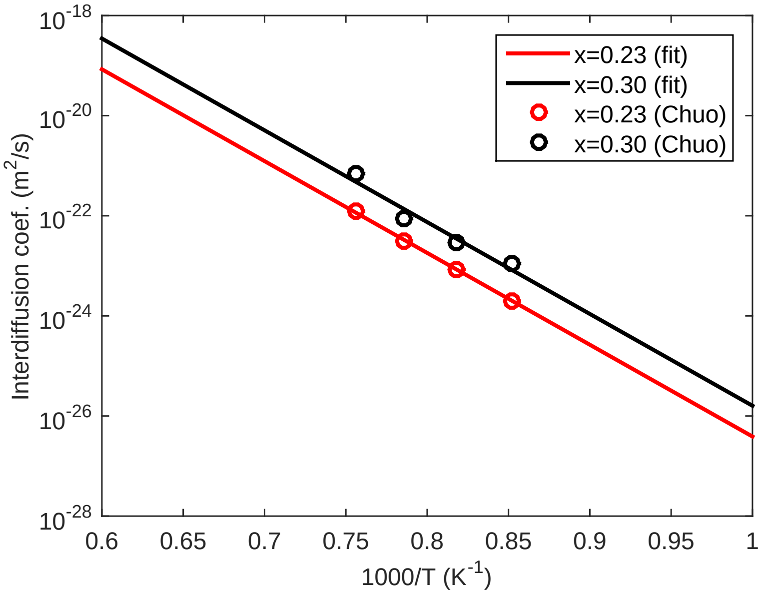

Figure 3.9: Temperature and concentration dependence of the interdiffusion coefficient of indium curve fitting to experimental data.

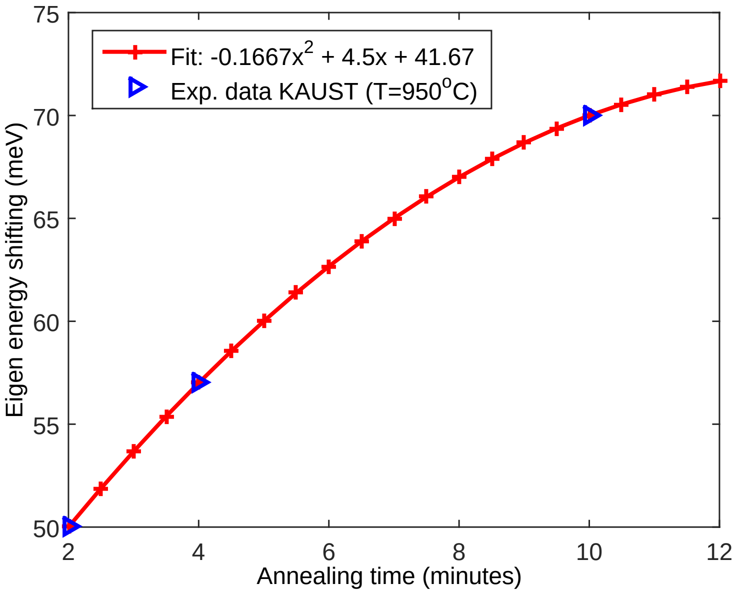

Figure 3.10: Experimental data of eigen energy shifting of $InGaN/GaN$ quantum well with annealing temperature 950 ^oC.

Photonic Lab., King Abdullah University of Science and Technology (KAUST), Thuwal, Kingdom of Saudi Arabia. The details are available in Chapter 5.

3.4 Energy Band Alignment

The occurrence of multiple interfaces in quantum structure is important to be considered due to the effects on energy bands. The alignment of energy band crucially drives the behavior and character or semiconductor junctions. In order to determine the semiconductor band gap energies, Vegard's law is used. Basically, the law relates the band gap energy of the alloys to the binary system, its mole fraction and a bowing parameter. Consider the $In_xGa_{1-x}N$ alloy with x is the indium mole fraction, the band gap energy can be calculated by

$$Eg[In_xGa_{1-x}N] = xEg[InN] + (1-x)Eg[GaN] - bx(1-x) \tag{3.16}$$

where

- $Eg[In_xGa_{1-x}N]$ is the band gap energy of $In_xGa_{1-x}N$, in eV.
- $Eg[InN]$ and $Eg[GaN]$ are the band gap energy of binary system InN and GaN, respectively, in eV.
- b is the bowing parameter.

The band profile is needed in this work to determine the conduction and valence band offsets, ΔE_c and ΔE_v, respectively. In the case of $GaN/InGaN$ heterojunction, the ratio of $\Delta E_c/\Delta E_v$ is predicted as 7/3. These parameters are used to calculate the potential energy of the structure using

$$U_c = -qV + \Delta E_c \tag{3.17}$$

$$U_v = -qV - \Delta E_v \tag{3.18}$$

where U_c and U_v are the conduction and valence potential energies, respectively, in eV.

3.5 Quantum Properties Model

As mentioned earlier, TDSE, Equation 2.7, is considered in this thesis as representation of quantum state. In order to simplify the computation process, the wave function ψ is considered as complex function as

$$\psi(t,\mathbf{r}) = \psi_{re}(t,\mathbf{r}) + i\psi_{im}(t,\mathbf{r}) \tag{3.19}$$

where ψ_{re} and ψ_{re} are the real and imaginary wave functions, respectively. Inserting Equation 3.19 in Equation 2.7 gives

$$i\hbar\frac{\partial\psi_{re}(t,\mathbf{r})}{\partial t} - \hbar\frac{\partial\psi_{im}(t,\mathbf{r})}{\partial\mathbf{r}} = \Big(-\frac{\hbar^2}{2m}\nabla^2 + U(\mathbf{r})\Big)\psi_{re}(t,\mathbf{r}) + i\Big(-\frac{\hbar^2}{2m}\nabla^2 + U(\mathbf{r})\Big)\psi_{im}(t,\mathbf{r}) \tag{3.20}$$

Splitting Equation 3.20 into two coupled equations representing its imaginary and real parts results

$$\frac{\partial \psi_{re}(t,\mathbf{r})}{\partial t} = \frac{1}{\hbar}\Big(-\frac{\hbar^2}{2m}\nabla^2 + U(\mathbf{r})\Big)\psi_{im}(t,\mathbf{r}) \tag{3.21}$$

and

$$\frac{\partial \psi_{im}(t,\mathbf{r})}{\partial t} = -\frac{1}{\hbar}\Big(-\frac{\hbar^2}{2m}\nabla^2 + U(\mathbf{r})\Big)\psi_{re}(t,\mathbf{r}) \tag{3.22}$$

CHAPTER 4

QUANTUM FINITE DIFFERENCE TIME DOMAIN SOLVER

In this chapter, the detail of Finite Difference Time Domain (FDTD) method will be presented for the solution of Interdiffusion and Polarization models. The result is incorporated to quantum properties solver which is termed as Q-FDTD. The inclusion of material properties, various discretization schemes, and absorbing boundary conditions for Schrodinger equation is also presented.

4.1 Numerical Solution of Polarization Model

The polarization model represented in Equation 3.5 can be shown in different format as

$$\begin{aligned}
&\frac{\partial \epsilon(\mathbf{r})}{\partial \mathbf{x}}.\frac{\partial V(\mathbf{r})}{\partial \mathbf{x}} + \epsilon(\mathbf{r}).\frac{\partial^2 V(\mathbf{r})}{\partial \mathbf{x}^2} + \\
&\frac{\partial \epsilon(\mathbf{r})}{\partial \mathbf{y}}.\frac{\partial V(\mathbf{r})}{\partial \mathbf{y}} + \epsilon(\mathbf{r}).\frac{\partial^2 V(\mathbf{r})}{\partial \mathbf{y}^2} + \\
&\frac{\partial \epsilon(\mathbf{r})}{\partial \mathbf{z}}.\frac{\partial V(\mathbf{r})}{\partial \mathbf{z}} + \epsilon(\mathbf{r}).\frac{\partial^2 V(\mathbf{r})}{\partial \mathbf{z}^2} = \pm\frac{\partial P(\mathbf{r})}{\partial \mathbf{x}}
\end{aligned} \tag{4.1}$$

for three dimensional case and

$$\frac{\partial \epsilon(\mathbf{x})}{\partial \mathbf{x}}.\frac{\partial V(\mathbf{x})}{\partial \mathbf{x}} + \epsilon(\mathbf{x}).\frac{\partial^2 V(\mathbf{x})}{\partial \mathbf{x}^2} = \pm\frac{\partial P(\mathbf{x})}{\partial \mathbf{x}} \tag{4.2}$$

for one dimensional case considering x-axis as growth direction. SOR iterative technique is used to approximate the solution numerically due to its ability to get faster convergence than other iterative methods.

4.1.1 Discretization

There are three parts of the 1D polarization model that have to be treated using appropriate differencing schemes.

- $\frac{\partial \epsilon(\mathbf{x})}{\partial \mathbf{x}}.\frac{\partial V(\mathbf{x})}{\partial \mathbf{x}}$ is discretized using first order Averaged Backward Forward Differencing (ABFD) scheme.
- $\frac{\partial^2 V(\mathbf{x})}{\partial \mathbf{x}^2}$ is discretized using second order Central Differencing (CD) scheme.
- $\frac{\partial P(\mathbf{x})}{\partial \mathbf{x}}$ is discretized using first order CD scheme.

It leads to the discretized form as

$$\begin{gathered}\frac{1}{2}\left(\frac{\epsilon(i+1)-\epsilon(i)}{\Delta \mathbf{x}}.\frac{V(i+1)-V(i)}{\Delta \mathbf{x}} + \frac{\epsilon(i)-\epsilon(i-1)}{\Delta \mathbf{x}}.\frac{V(i)-V(i-1)}{\Delta \mathbf{x}}\right)+ \\ \epsilon(i)\left(\frac{V(i+1)-V(i)+V(i-1)}{\Delta \mathbf{x}^2}\right) = \frac{P(i+1)-P(i-1)}{2\Delta \mathbf{x}}\end{gathered} \tag{4.3}$$

Thus, the electrostatic potential can be calculated as

$$\begin{aligned} V(i) = \frac{1}{\epsilon(i+1)+2\epsilon(i)+\epsilon(i-1)} \Bigg[& V(i+1)\Big(\epsilon(i+1)+\epsilon(i)\Big)+ \\ & V(i-1)\Big(\epsilon(i)+\epsilon(i-1)\Big)- \\ & \Delta\mathbf{x}\Big(P(i+1)-P(i-1)\Big)\Bigg] \end{aligned} \tag{4.4}$$

4.1.2 Successive Over Relaxation (SOR) Method

The $V(i)$ in Equation 4.4 shows that the potential at i^{th}-grid depends on the potential at one point before and after, i.e. $V(i-1)$ and $V(i+1)$, respectively. As an iterative method, the key is minimizing the residue between current and previous iterative solution successively. The residual is calculated using Equation 4.5.

$$\begin{aligned} R(i) = -V(i) + \frac{1}{\epsilon(i+1)+2\epsilon(i)+\epsilon(i-1)} \Bigg[& V(i+1)\Big(\epsilon(i+1)+\epsilon(i)\Big)+ \\ & V(i-1)\Big(\epsilon(i)+\epsilon(i-1)\Big)- \\ & \Delta\mathbf{x}\Big(P(i+1)-P(i-1)\Big)\Bigg] \end{aligned} \tag{4.5}$$

The updated residual is then used to recalculate the potential as shown in Equation 4.6 that contains asymptotic convergence rate factor ω.

$$V^n(i) = V^{n-1}(i) + \omega R^{n-1}(i) \tag{4.6}$$

where ω is the relaxation parameter and notation n and $n-1$ represent current and previous iterations.

4.1.3 Consistency

In order to determine the consistency of the FDA of polarization model, Taylor series expansion is applied in Equation 4.3 for the term $\epsilon(i \pm 1)$, $V(i \pm 1)$ and $P(i \pm 1)$. It yields

$$
\begin{aligned}
&\left(\epsilon(i) + \Delta\mathbf{x}\frac{\partial\epsilon(\mathbf{x})}{\partial\mathbf{x}} + \frac{\Delta\mathbf{x}^2}{2}\frac{\partial^2\epsilon(\mathbf{x})}{\partial\mathbf{x}^2} + \frac{\Delta\mathbf{x}^3}{3!}\frac{\partial^3\epsilon(\mathbf{x})}{\partial\mathbf{x}^3} + \frac{\Delta\mathbf{x}^4}{4!}\frac{\partial^4\epsilon(\mathbf{x})}{\partial\mathbf{x}^4} - \epsilon(i)\right). \\
&\left(\Delta\mathbf{x}\frac{\partial V(\mathbf{x})}{\partial\mathbf{x}} + \frac{\Delta\mathbf{x}^2}{2}\frac{\partial^2 V(\mathbf{x})}{\partial\mathbf{x}^2} + \frac{\Delta\mathbf{x}^3}{3!}\frac{\partial^3 V(\mathbf{x})}{\partial\mathbf{x}^3} + \frac{\Delta\mathbf{x}^4}{4!}\frac{\partial^4 V(\mathbf{x})}{\partial\mathbf{x}^4}\right) + \\
&\left(\epsilon(i) + \Delta\mathbf{x}\frac{\partial\epsilon(\mathbf{x})}{\partial\mathbf{x}} - \frac{\Delta\mathbf{x}^2}{2}\frac{\partial^2\epsilon(\mathbf{x})}{\partial\mathbf{x}^2} + \frac{\Delta\mathbf{x}^3}{3!}\frac{\partial^3\epsilon(\mathbf{x})}{\partial\mathbf{x}^3} - \frac{\Delta\mathbf{x}^4}{4!}\frac{\partial^4\epsilon(\mathbf{x})}{\partial\mathbf{x}^4} - \epsilon(i)\right). \\
&\left(\Delta\mathbf{x}\frac{\partial V(\mathbf{x})}{\partial\mathbf{x}} - \frac{\Delta\mathbf{x}^2}{2}\frac{\partial^2 V(\mathbf{x})}{\partial\mathbf{x}^2} + \frac{\Delta\mathbf{x}^3}{3!}\frac{\partial^3 V(\mathbf{x})}{\partial\mathbf{x}^3} - \frac{\Delta\mathbf{x}^4}{4!}\frac{\partial^4 V(\mathbf{x})}{\partial\mathbf{x}^4}\right) + \\
&4\epsilon(i)\left(\frac{\Delta\mathbf{x}^2}{2}\frac{\partial^2\epsilon(\mathbf{x})}{\partial\mathbf{x}^2} + \frac{\Delta\mathbf{x}^4}{4!}\frac{\partial^2\epsilon(\mathbf{x})}{\partial\mathbf{x}^4}\right) = 2\Delta\mathbf{x}\left(\Delta\mathbf{x}\frac{\partial V(\mathbf{x})}{\partial\mathbf{x}} + \frac{\Delta\mathbf{x}^3}{3!}\frac{\partial^3 V(\mathbf{x})}{\partial\mathbf{x}^3}\right)
\end{aligned}
\tag{4.7}
$$

$$
\begin{aligned}
&\left(\frac{\partial\epsilon(\mathbf{x})}{\partial\mathbf{x}} + \frac{\Delta\mathbf{x}}{2}\frac{\partial^2\epsilon(\mathbf{x})}{\partial\mathbf{x}^2} + \frac{\Delta\mathbf{x}^2}{3!}\frac{\partial^3\epsilon(\mathbf{x})}{\partial\mathbf{x}^3} + \frac{\Delta\mathbf{x}^3}{4!}\frac{\partial^4\epsilon(\mathbf{x})}{\partial\mathbf{x}^4}\right). \\
&\left(\frac{\partial V(\mathbf{x})}{\partial\mathbf{x}} + \frac{\Delta\mathbf{x}}{2}\frac{\partial^2 V(\mathbf{x})}{\partial\mathbf{x}^2} + \frac{\Delta\mathbf{x}^2}{3!}\frac{\partial^3 V(\mathbf{x})}{\partial\mathbf{x}^3} + \frac{\Delta\mathbf{x}^3}{4!}\frac{\partial^4 V(\mathbf{x})}{\partial\mathbf{x}^4}\right) + \\
&\left(\frac{\partial\epsilon(\mathbf{x})}{\partial\mathbf{x}} - \frac{\Delta\mathbf{x}}{2}\frac{\partial^2\epsilon(\mathbf{x})}{\partial\mathbf{x}^2} + \frac{\Delta\mathbf{x}^2}{3!}\frac{\partial^3\epsilon(\mathbf{x})}{\partial\mathbf{x}^3} - \frac{\Delta\mathbf{x}^3}{4!}\frac{\partial^4\epsilon(\mathbf{x})}{\partial\mathbf{x}^4}\right). \\
&\left(\frac{\partial V(\mathbf{x})}{\partial\mathbf{x}} - \frac{\Delta\mathbf{x}}{2}\frac{\partial^2 V(\mathbf{x})}{\partial\mathbf{x}^2} + \frac{\Delta\mathbf{x}^2}{3!}\frac{\partial^3 V(\mathbf{x})}{\partial\mathbf{x}^3} - \frac{\Delta\mathbf{x}^3}{4!}\frac{\partial^2 V(\mathbf{x})}{\partial\mathbf{x}^4}\right) + \\
&4\epsilon(i)\left(\frac{1}{2}\frac{\partial^2\epsilon(\mathbf{x})}{\partial\mathbf{x}^2} + \frac{\Delta\mathbf{x}^2}{4!}\frac{\partial^2\epsilon(\mathbf{x})}{\partial\mathbf{x}^4}\right) = 2\left(\frac{\partial V(\mathbf{x})}{\partial\mathbf{x}} + \frac{\Delta\mathbf{x}^2}{3!}\frac{\partial^3 V(\mathbf{x})}{\partial\mathbf{x}^3}\right)
\end{aligned}
\tag{4.8}
$$

Next, set $\Delta\mathbf{x} \to 0$ on Equation 4.8 and simplify the equation. It shows that Equation 4.8 comes back to the original polarization model as formulated in Equation 4.2. In other words, Equation 4.3 is consistent.

4.1.4 Stability

The stability of the SOR iteration is defined by ω, which should lie between zero and two, $0 < \omega < 2$. It is called over relaxation if ω is greater than 1 and is called under relaxation if ω is less than 1.

4.1.5 Convergence

Since the FDA of polarization model is consistent and conditionally stable, the convergence can be reached if the stability condition is satisfied. In other word, the ω is should be between 1 and 2.

4.2 Numerical Solution of Proposed Interdiffusion Model

The Fickian interdiffusion formulation used in this thesis, Equation 2.3, can be presented in different form as

$$\begin{aligned}\frac{\partial c(t,\mathbf{r})}{\partial t} &= \frac{\partial D(T,c)}{\partial \mathbf{x}}.\frac{\partial c(t,\mathbf{r})}{\partial \mathbf{x}} + D(T,c).\frac{\partial^2 c(t,\mathbf{r})}{\partial \mathbf{x}^2} \\ &+ \frac{\partial D(T,c)}{\partial \mathbf{y}}.\frac{\partial c(t,\mathbf{r})}{\partial \mathbf{y}} + D(T,c).\frac{\partial^2 c(t,\mathbf{r})}{\partial \mathbf{y}^2} \\ &+ \frac{\partial D(T,c)}{\partial \mathbf{z}}.\frac{\partial c(t,\mathbf{r})}{\partial \mathbf{z}} + D(T,c).\frac{\partial^2 c(t,\mathbf{r})}{\partial \mathbf{z}^2}\end{aligned} \tag{4.9}$$

for three dimensional problem and

$$\frac{\partial c(t,\mathbf{x})}{\partial t} = \frac{\partial D(T,c)}{\partial \mathbf{x}}.\frac{\partial c(t,\mathbf{x})}{\partial \mathbf{x}} + D(T,c).\frac{\partial^2 c(t,\mathbf{x})}{\partial \mathbf{x}^2} \tag{4.10}$$

for one dimensional problem considering x-axis as growth direction.

4.2.1 Discretization

Considering one dimensional case, there are three parts:

- $\frac{\partial c(t,\mathbf{x})}{\partial t}$ is discretized using first order Forward Differencing (FD) scheme in time domain.
- $\frac{\partial D(T,c)}{\partial \mathbf{x}}.\frac{\partial c(t,\mathbf{x})}{\partial \mathbf{x}}$ is discretized using first order ABFD scheme in spatial domain.
- $\frac{\partial^2 c(t,\mathbf{x})}{(\partial \mathbf{x})^2}$ is discretized using second order CD scheme in spatial domain.

The need for the ABFD scheme to evaluate $\dfrac{\partial D(T,c)}{\partial \mathbf{x}}.\dfrac{\partial c(t,\mathbf{x})}{\partial \mathbf{x}}$ is discussed below.

It leads to the discretized form as

$$\begin{aligned}\frac{c^{n+1}(i)-c^n(i)}{\Delta t} =& \frac{1}{2}\left(\frac{D^n(i+1)-D^n(i)}{\Delta \mathbf{x}}.\frac{c^n(i+1)-c^n(i)}{\Delta \mathbf{x}}\right)+ \\ & \frac{1}{2}\left(\frac{D^n(i)-D^n(i-1)}{\Delta \mathbf{x}}.\frac{c^n(i)-c^n(i-1)}{\Delta \mathbf{x}}\right)+ \\ & D^n(i)\left(\frac{c^n(i+1)-c^n(i)+c^n(i-1)}{\Delta \mathbf{x}^2}\right)\end{aligned} \tag{4.11}$$

$$\begin{aligned}c^{n+1}(i) = c^n(i) +& \frac{\Delta t}{2}\left(\frac{D^n(i+1)-D^n(i)}{\Delta \mathbf{x}}.\frac{c^n(i+1)-c^n(i)}{\Delta \mathbf{x}}\right)+ \\ & \frac{\Delta t}{2}\left(\frac{D^n(i)-D^n(i-1)}{\Delta \mathbf{x}}.\frac{c^n(i)-c^n(i-1)}{\Delta \mathbf{x}}\right)+ \\ & D^n(i)\left(\frac{c^n(i+1)-c^n(i)+c^n(i-1)}{\Delta \mathbf{x}^2}\right)\end{aligned} \tag{4.12}$$

4.2.2 Consistency

In order to determine the consistency of the FDA of interdiffusion model, Taylor series expansion is applied in Equation 4.12 for the term $c^{n+1}(i)$, $c^n(i \pm 1)$ and $D(i \pm 1)$. It yields

$$
\begin{aligned}
&c^n(i) + \Delta t\frac{\partial c}{\partial t} + \frac{\Delta t^2}{2}\frac{\partial^2 c}{\partial t^2} + \frac{\Delta t^3}{3!}\frac{\partial^3 c}{\partial t^3} + \frac{\Delta t^4}{4!}\frac{\partial^2 c}{\partial t^4} = c^n(i) + \frac{\Delta t}{2\Delta \mathbf{x}^2}\Bigg[\\
&\quad\Bigg(D^n(i) + \Delta \mathbf{x}\frac{\partial D}{\partial \mathbf{x}} + \frac{\Delta \mathbf{x}^2}{2}\frac{\partial^2 D}{\partial \mathbf{x}^2} + \frac{\Delta \mathbf{x}^3}{3!}\frac{\partial^3 D}{\partial \mathbf{x}^3} + \frac{\Delta \mathbf{x}^4}{4!}\frac{\partial^4 D}{\partial \mathbf{x}^4} - D^n(i)\Bigg). \\
&\quad\Bigg(D^n(i) + \Delta \mathbf{x}\frac{\partial c}{\partial \mathbf{x}} + \frac{\Delta \mathbf{x}^2}{2}\frac{\partial^2 c}{\partial \mathbf{x}^2} + \frac{\Delta \mathbf{x}^3}{3!}\frac{\partial^3 c}{\partial \mathbf{x}^3} + \frac{\Delta \mathbf{x}^4}{4!}\frac{\partial^4 c}{\partial \mathbf{x}^4} - D^n(i)\Bigg)+ \\
&\quad\Bigg(D^n(i) + \Delta \mathbf{x}\frac{\partial D}{\partial \mathbf{x}} - \frac{\Delta \mathbf{x}^2}{2}\frac{\partial^2 D}{\partial \mathbf{x}^2} + \frac{\Delta \mathbf{x}^3}{3!}\frac{\partial^3 D}{\partial \mathbf{x}^3} - \frac{\Delta \mathbf{x}^4}{4!}\frac{\partial^4 D}{\partial \mathbf{x}^4} - D^n(i)\Bigg). \\
&\quad\Bigg(D^n(i) + \Delta \mathbf{x}\frac{\partial c}{\partial \mathbf{x}} - \frac{\Delta \mathbf{x}^2}{2}\frac{\partial^2 c}{\partial \mathbf{x}^2} + \frac{\Delta \mathbf{x}^3}{3!}\frac{\partial^3 c}{\partial \mathbf{x}^3} - \frac{\Delta \mathbf{x}^4}{4!}\frac{\partial^4 c}{\partial \mathbf{x}^4} - D^n(i)\Bigg)\Bigg]+ \\
&\quad 2D^n(i)\frac{\Delta t}{\Delta \mathbf{x}^2}\Bigg(\frac{\Delta \mathbf{x}^2}{2}\frac{\partial^2 D}{\partial \mathbf{x}^2} + \frac{\Delta \mathbf{x}^4}{4!}\frac{\partial^4}{\partial \mathbf{x}^4}\Bigg)
\end{aligned}
\tag{4.13}
$$

$$
\begin{aligned}
&\frac{\partial c}{\partial t} + \frac{\Delta t}{2}\frac{\partial^2 c}{\partial t^2} + \frac{\Delta t^2}{3!}\frac{\partial^3 c}{\partial t^3} + \frac{\Delta t^3}{4!}\frac{\partial^2 c}{\partial t^4} = \frac{1}{2}\Bigg[\\
&\quad\Bigg(\frac{\partial D}{\partial \mathbf{x}} + \frac{\Delta \mathbf{x}}{2}\frac{\partial^2 D}{\partial \mathbf{x}^2} + \frac{\Delta \mathbf{x}^2}{3!}\frac{\partial^3 D}{\partial \mathbf{x}^3} + \frac{\Delta \mathbf{x}^3}{4!}\frac{\partial^4 D}{\partial \mathbf{x}^4}\Bigg). \\
&\quad\Bigg(\frac{\partial c}{\partial \mathbf{x}} + \frac{\Delta \mathbf{x}}{2}\frac{\partial^2 c}{\partial \mathbf{x}^2} + \frac{\Delta \mathbf{x}^2}{3!}\frac{\partial^3 c}{\partial \mathbf{x}^3} + \frac{\Delta \mathbf{x}^3}{4!}\frac{\partial^4 c}{\partial \mathbf{x}^4}\Bigg)+ \\
&\quad\Bigg(\frac{\partial D}{\partial \mathbf{x}} - \frac{\Delta \mathbf{x}}{2}\frac{\partial^2 D}{\partial \mathbf{x}^2} + \frac{\Delta \mathbf{x}^2}{3!}\frac{\partial^3 D}{\partial \mathbf{x}^3} - \frac{\Delta \mathbf{x}^3}{4!}\frac{\partial^4 D}{\partial \mathbf{x}^4}\Bigg). \\
&\quad\Bigg(\frac{\partial c}{\partial \mathbf{x}} - \frac{\Delta \mathbf{x}}{2}\frac{\partial^2 c}{\partial \mathbf{x}^2} + \frac{\Delta \mathbf{x}^2}{3!}\frac{\partial^3 c}{\partial \mathbf{x}^3} - \frac{\Delta \mathbf{x}^3}{4!}\frac{\partial^4 c}{\partial \mathbf{x}^4}\Bigg)\Bigg]+ \\
&\quad 2D^n(i)\Bigg(\frac{1}{2}\frac{\partial^2}{\partial \mathbf{x}^2} + \frac{\Delta \mathbf{x}^2}{4!}\frac{\partial^4}{\partial \mathbf{x}^4}\Bigg)
\end{aligned}
\tag{4.14}
$$

Letting $\Delta t \to 0$, $\Delta x \to 0$ and simplifying, Equation 4.14 tends to the original interdiffusion model, Equation 4.10. Thus, Equation 4.12 is consistent.

4.2.3 The von Neumann Stability Criterion

Next, apply von Neumann stability analysis on Equation 4.12 to determine the stability criterion.

$$\begin{aligned}G(\theta)c^n(i) = c^n(i) + \frac{\Delta t}{2\Delta \mathbf{x}^2}\Bigg[&\Big(D^n(i+1) - D^n(i)\Big).\Big(c^n(i)e^{i\theta} - c^n(i)\Big) + \\ &\Big(D^n(i) - D^n(i-1)\Big).\Big(c^n(i) - c^n(i)e^{-i\theta}\Big) + \\ &2D^n(i)\Big(c^n(i)e^{i\theta} - 2c^n(i) + c^n(i)e^{-i\theta}\Big)\Bigg]\end{aligned} \tag{4.15}$$

$$G(\theta) = 1 + \frac{\Delta t}{2\Delta \mathbf{x}^2}\Bigg[R_1\Big(e^{i\theta} - 1\Big) + R_2\Big(1 - e^{-i\theta}\Big) + 2R_3\Big(e^{i\theta} - 2 + e^{-i\theta}\Big)\Bigg] \tag{4.16}$$

where

- $R_1 = \Bigg\|\Big(D^n(i+1) - D^n(i)\Big)\Bigg\|_\infty$
- $R_2 = \Bigg\|\Big(D^n(i) - D^n(i-1)\Big)\Bigg\|_\infty$
- $R_3 = \Bigg\|\Big(D^n(i)\Big)\Bigg\|_\infty$

Since D is positive definite, $R_3 \geq R_1$ and $R_3 \geq R_2$ are always valid. For simplification, $R = \Bigg\|R_1, R_2, R_3\Bigg\|_\infty$ is considered. Thus, Equation 4.16 becomes

$$\begin{aligned}G(\theta) &= 1 + \frac{R\Delta t}{2\Delta \mathbf{x}^2}\Bigg[\Big(e^{i\theta} - e^{-i\theta}\Big) + 2\Big(e^{i\theta} - 2 + e^{-i\theta}\Big)\Bigg] \\ &= 1 + \frac{R\Delta t}{\Delta \mathbf{x}^2}\Bigg[\Big(I\sin(\theta)\Big) + \Big(2\cos(\theta) - 2\Big)\Bigg]\end{aligned} \tag{4.17}$$

As a complex function, $G(\theta)$ is split into real and imaginary parts as

$$G_{re}(\theta) = 1 + \frac{R\Delta t}{\Delta \mathbf{x}^2}\Big(2\cos(\theta) - 2\Big) \tag{4.18}$$

and

$$G_{im}(\theta) = \frac{R\Delta t}{\Delta \mathbf{x}^2}\sin(\theta) \tag{4.19}$$

Considering Equation 2.13, the stability criterion can be determined as

$$\left|1 + \frac{R\Delta t}{\Delta \mathbf{x}^2}\Big(2\cos(\theta) - 2\Big)\right| \leq 1 \tag{4.20}$$

for the real part. The worst case of it is when θ equals to π and leads to

$$\frac{R\Delta t}{\Delta \mathbf{x}^2} \leq \frac{1}{2} \tag{4.21}$$

In case of imaginary part, the stability criterion can be determined as

$$\left|\frac{R\Delta t}{\Delta \mathbf{x}^2}\sin(\theta)\right| \leq 1 \tag{4.22}$$

Letting θ equals to $\pi/2$, it tends to

$$\frac{R\Delta t}{\Delta \mathbf{x}^2} \leq 1 \tag{4.23}$$

Taking the worst case between real and imaginary parts, Equation 4.21 is the stability criterion. The filled part of Figure 4.1 shows the guaranteed stability region of interdiffusion model based on von Neumann stability.

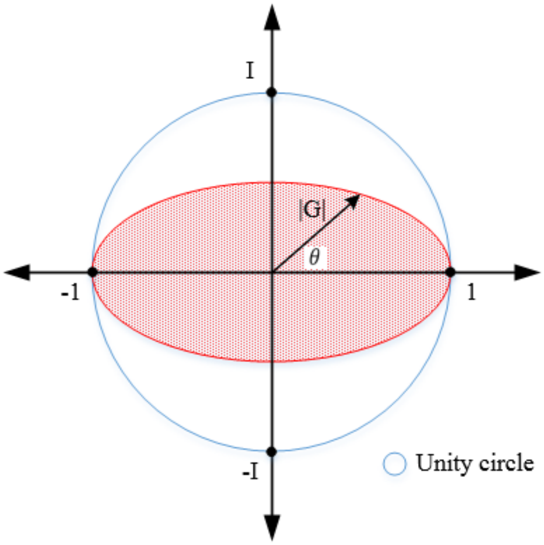

Figure 4.1: Unit circle and stability region of proposed interdiffusion model.

4.2.4 Convergence

As conclusion of consistency observation and von Neumann stability analysis above, the FDA of proposed interdiffusion model will meet the convergence requirement in the simulation.

4.2.5 Boundary Conditions

For interdiffusion model in solid Neumann boundary condition is used at the start and end points of the simulation domain. It means that there is no flux or in this case a concentration of atom at the end interface. It is formulated as

$$\nabla c|_{\partial\Omega} = 0 \qquad on \quad \partial\Omega \tag{4.24}$$

4.2.6 Discussion

The proposed discretization of interdiffusion model is validated by comparing the numerical result with analytical solution that has been derived by Mukai et.al in [34] for the case of constant interdiffusion coefficient. As a test, one dimensional $GaN/InGaN$ quantum well is considered with indium mole fraction of 0.2, interdiffusion coefficient is 6.9x10^{-23} m^2/s and a varying interdiffusion length, $L_d = \sqrt{Dt}$, of L_{d1}=0.5 nm, L_{d2}=1 nm and L_{d3}=1.5 nm. The comparison results in an excellent agreement with maximum error of 0.4% as shown in Figure 4.2. As can be observed from Figure 4.2, the error increases as the interdiffusion length larger because the longer interdiffusion produces stretcher indium profile.

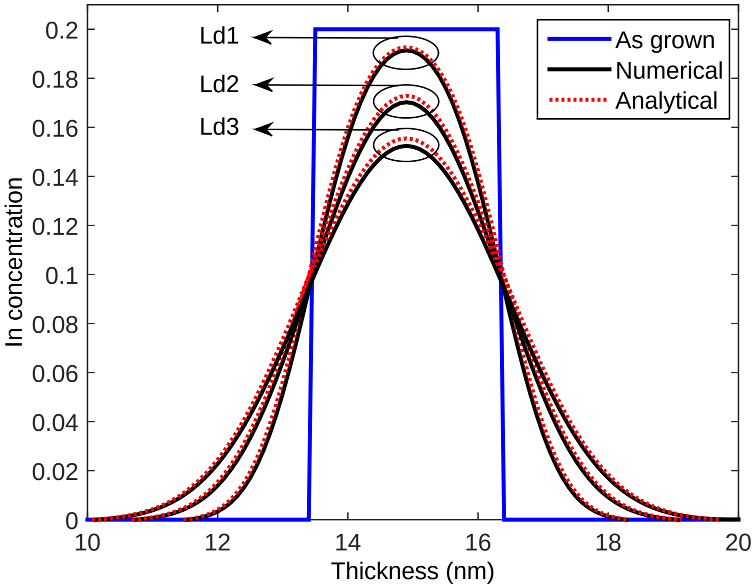

Figure 4.2: Comparison of numerical and analytical solutions of indium concentration after intermixing process.

Another important point is the introduction of ABFD scheme to deal with $\frac{\partial f(\mathbf{x})}{\partial \mathbf{x}}.\frac{\partial g(\mathbf{x})}{\partial \mathbf{x}}$ type equation in interdiffusion models. The ABFD scheme gives the correct concentration profile unlike Backward Differencing (BD) and FD schemes that generate wrong representation. As a test, in the case of one dimensional $GaN/InGaN$ single quantum well (SQW) with symmetrical interdiffusion process, Figure 4.3 shows the evidence of statement above. In fact, CD scheme can also give the same concentration profile. However, CD scheme is not considered in this work because it can not maintain the total indium concentration after annealing process. It leads to dissipative solution as shown in Figuree 4.4. The inconsistency of indium concentration profile and total indium concentration lead the incorrect eigen energy and eigen function.

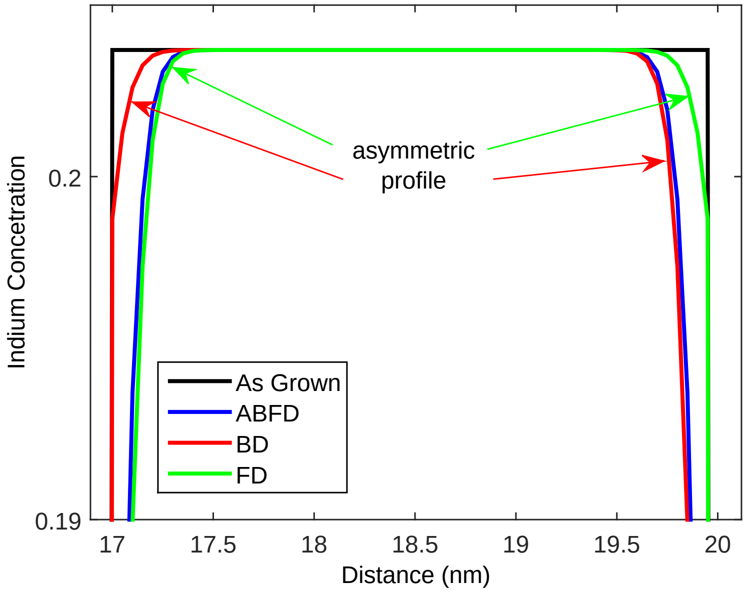

Figure 4.3: Indium concentration profile after annealing process using different discretization schemes.

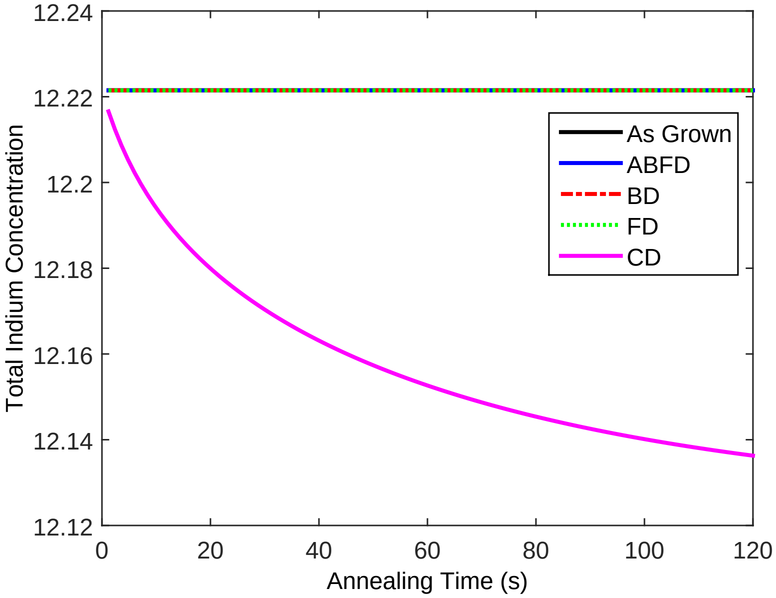

Figure 4.4: Total indium concentration after annealing process using different discretization schemes.

4.3 Numerical Solution of Schrödinger Equation

The coupled real and imaginary equations in Equation 3.21 and 3.22, respectively, can be written differently as

$$\begin{aligned}\frac{\partial\psi_{re}(t,\mathbf{r})}{\partial t} = \frac{1}{\hbar}\Big(&- \frac{\hbar^2}{2m}\frac{\partial^2\psi_{im}(t,\mathbf{x})}{\partial\mathbf{x}^2} + U(\mathbf{x})\psi_{im}(t,\mathbf{x}) \\ &- \frac{\hbar^2}{2m}\frac{\partial^2\psi_{im}(t,\mathbf{y})}{\partial\mathbf{y}^2} + U(\mathbf{y})\psi_{im}(t,\mathbf{y}) \\ &- \frac{\hbar^2}{2m}\frac{\partial^2\psi_{im}(t,\mathbf{z})}{\partial\mathbf{z}^2} + U(\mathbf{z})\psi_{im}(t,\mathbf{z})\Big)\end{aligned} \tag{4.25}$$

$$\begin{aligned}\frac{\partial\psi_{im}(t,\mathbf{r})}{\partial t} = -\frac{1}{\hbar}\Big(&- \frac{\hbar^2}{2m}\frac{\partial^2\psi_{re}(t,\mathbf{x})}{\partial\mathbf{x}^2} + U(\mathbf{x})\psi_{re}(t,\mathbf{x}) \\ &- \frac{\hbar^2}{2m}\frac{\partial^2\psi_{re}(t,\mathbf{y})}{\partial\mathbf{y}^2} + U(\mathbf{y})\psi_{re}(t,\mathbf{y}) \\ &- \frac{\hbar^2}{2m}\frac{\partial^2\psi_{re}(t,\mathbf{z})}{\partial\mathbf{z}^2} + U(\mathbf{z})\psi_{re}(t,\mathbf{z})\Big)\end{aligned} \tag{4.26}$$

for three dimensional case and

$$\frac{\partial \psi_{re}(t,\mathbf{x})}{\partial t} = \frac{1}{\hbar}\Big(-\frac{\hbar^2}{2m}\frac{\partial^2 \psi_{im}(t,\mathbf{x})}{\partial \mathbf{x}^2} + U(\mathbf{x})\psi_{im}(t,\mathbf{x})\Big) \tag{4.27}$$

$$\frac{\partial \psi_{im}(t,\mathbf{x})}{\partial t} = -\frac{1}{\hbar}\Big(-\frac{\hbar^2}{2m}\frac{\partial^2 \psi_{re}(t,\mathbf{x})}{\partial \mathbf{x}^2} + U(\mathbf{x})\psi_{re}(t,\mathbf{x})\Big) \tag{4.28}$$

for one dimensional case.

4.3.1 Discretization

The discretization rules considered for 1D Schrödinger equation are

- $\frac{\partial \psi_{re}(t,\mathbf{x})}{\partial t}$ and $\frac{\partial \psi_{im}(t,\mathbf{x})}{\partial t}$ are discretized using first order FD scheme in time domain.
- $\frac{\partial^2 \psi_{re}(t,\mathbf{x})}{\partial \mathbf{x}^2}$ and $\frac{\partial^2 \psi_{im}(t,\mathbf{x})}{\partial \mathbf{x}^2}$ are discretized using second order CD scheme in spatial domain.

This leads to the discretized form as

$$\begin{aligned}&\frac{\psi_{re}^{n+1}(i) - \psi_{re}^{n}(i)}{\Delta t} = \\ &\qquad \frac{1}{\hbar}\bigg(-\frac{\hbar^2}{2m}\Big(\frac{\psi_{im}^{n}(i+1) - 2\psi_{im}^{n}(i) + \psi_{im}^{n}(i-1)}{\Delta \mathbf{x}^2}\Big) + U^n(i)\psi_{im}^{n}(i)\bigg)\end{aligned} \tag{4.29}$$

$$\begin{aligned}&\psi_{re}^{n+1}(i) = \psi_{re}^{n}(i) + \\ &\qquad \frac{\Delta t}{\hbar}\bigg(-\frac{\hbar^2}{2m}\Big(\frac{\psi_{im}^{n}(i+1) - 2\psi_{im}^{n}(i) + \psi_{im}^{n}(i-1)}{\Delta \mathbf{x}^2}\Big) + U^n(i)\psi_{im}^{n}(i)\bigg)\end{aligned} \tag{4.30}$$

$$\begin{aligned}\frac{\psi_{im}^{n+1}(i)-\psi_{im}^{n}(i)}{\Delta t} &= \\ &-\frac{1}{\hbar}\Big(-\frac{\hbar^2}{2m}\Big(\frac{\psi_{re}^{n}(i+1)-2\psi_{re}^{n}(i)+\psi_{re}^{n}(i-1)}{\Delta\mathbf{x}^2}\Big)+U^n(i)\psi_{re}^{n}(i)\Big)\end{aligned}\tag{4.31}$$

$$\begin{aligned}\psi_{im}^{n+1}(i) &= \psi_{im}^{n}(i)+ \\ &-\frac{\Delta t}{\hbar}\Big(-\frac{\hbar^2}{2m}\Big(\frac{\psi_{re}^{n}(i+1)-2\psi_{re}^{n}(i)+\psi_{re}^{n}(i-1)}{\Delta\mathbf{x}^2}\Big)+U^n(i)\psi_{re}^{n}(i)\Big)\end{aligned}\tag{4.32}$$

4.3.2 Consistency

In order to determine the consistency of the FDA of interdiffusion model, Taylor series expansion is applied in Equation 4.30 for the term $\psi_{re}^{n+1}(i)$, $\psi_{im}^{n+1}(i)$ and $\psi_{re}^{n}(i\pm 1)$ and $\psi_{im}^{n}(i\pm 1)$. It yields

$$\begin{aligned}\psi_{re}^{n}(i)+\Delta t\frac{\partial\psi_{re}}{\partial t}+\frac{\Delta t^2}{2}\frac{\partial^2\psi_{re}}{\partial t^2}+\frac{\Delta t^3}{3!}\frac{\partial^3\psi_{re}}{\partial t^3}+\frac{\Delta t^4}{4!}\frac{\partial^2\psi_{re}}{\partial t^4} &= \psi_{re}^{n}(i)+ \\ \frac{\Delta t}{\hbar}\Big(-\frac{\hbar^2}{2m\Delta\mathbf{x}^2}\Big(\frac{\Delta\mathbf{x}^2}{2}\frac{\partial^2\psi_{im}}{\partial\mathbf{x}^2}+\frac{\Delta\mathbf{x}^4}{4!}\frac{\partial^4\psi_{im}}{\partial\mathbf{x}^4}\Big)+U^n(i)\psi_{im}^{n}(i)\Big)&\end{aligned}\tag{4.33}$$

$$\begin{aligned}\frac{\partial\psi_{re}}{\partial t}+\frac{\Delta t}{2}\frac{\partial^2\psi_{re}}{\partial t^2}+\frac{\Delta t^2}{3!}\frac{\partial^3\psi_{re}}{\partial t^3}+\frac{\Delta t^3}{4!}\frac{\partial^2\psi_{re}}{\partial t^4} &= \\ \frac{1}{\hbar}\Big(-\frac{\hbar^2}{2m}\Big(\frac{1}{2}\frac{\partial^2\psi_{im}}{\partial\mathbf{x}^2}+\frac{\Delta\mathbf{x}^2}{4!}\frac{\partial^4\psi_{im}}{\partial\mathbf{x}^4}\Big)+U^n(i)\psi_{im}^{n}(i)\Big)&\end{aligned}\tag{4.34}$$

Letting $\Delta t \to 0$, $\Delta x \to 0$ and simplification, Equation 4.34 tends to the original Schrödinger equation, Equation 4.30.

$$\begin{aligned}\psi^n_{im}(i) + \Delta t\frac{\partial\psi_{re}}{\partial t} + \frac{\Delta t^2}{2}\frac{\partial^2\psi_{re}}{\partial t^2} + \frac{\Delta t^3}{3!}\frac{\partial^3\psi_{re}}{\partial t^3} + \frac{\Delta t^4}{4!}\frac{\partial^2\psi_{re}}{\partial t^4} = \psi^n_{im}(i) - \\ \frac{\Delta t}{\hbar}\Big(- \frac{\hbar^2}{2m\Delta\mathbf{x}^2}\Big(\frac{\Delta\mathbf{x}^2}{2}\frac{\partial^2\psi_{re}}{\partial\mathbf{x}^2} + \frac{\Delta\mathbf{x}^4}{4!}\frac{\partial^4\psi_{re}}{\partial\mathbf{x}^4}\Big) + U^n(i)\psi^n_{re}(i)\Big)\end{aligned} \tag{4.35}$$

$$\begin{aligned}\frac{\partial\psi_{im}}{\partial t} + \frac{\Delta t}{2}\frac{\partial^2\psi_{re}}{\partial t^2} + \frac{\Delta t^2}{3!}\frac{\partial^3\psi_{re}}{\partial t^3} + \frac{\Delta t^3}{4!}\frac{\partial^2\psi_{re}}{\partial t^4} = \\ -\frac{1}{\hbar}\Big(- \frac{\hbar^2}{2m}\Big(\frac{1}{2}\frac{\partial^2\psi_{re}}{\partial\mathbf{x}^2} + \frac{\Delta\mathbf{x}^2}{4!}\frac{\partial^4\psi_{re}}{\partial\mathbf{x}^4}\Big) + U^n(i)\psi^n_{re}(i)\Big)\end{aligned} \tag{4.36}$$

Letting $\Delta t \to 0$, $\Delta x \to 0$ and simplification, Equation 4.36 tends to the original Schrödinger equation, Equation 4.32.

4.3.3 Stability Criterion

In this thesis, the stability criterion of Schrödinger equation follows the rule that has been defined by [28]. He suggested that the value of Δt and Δt meet the following rule,

$$ra = \frac{\hbar\Delta t}{2m\Delta\mathbf{x^2}} \tag{4.37}$$

where ra is a positive number that is less than 0.115 in order to maintain the stability of the simulation.

4.3.4 Convergence

As we can conclude, the discretized form of the coupled Schrödinger equations are consistent and conditionally stable. Thus, the convergence of the simulation is guaranteed under stability criterion.

4.3.5 Absorbing Boundary Conditions

In order to avoid outgoing waves from being reflected at the boundary of the simulation and prevent the instability of the simulation, the presence of absorbing boundary condition (ABC) is necessary. There are two types of ABCs used in this thesis.

Stretched perfectly matched layer (PML)

The PML is based on stretched simulation points or layers, which is a complex spatial function, $\gamma(\mathbf{x})$. In this thesis, the PML is used only for one dimensional problem since it needs large number of points. The $\gamma(\mathbf{x})$ is inserted to the one dimensional Schrödinger equation,

$$\frac{\partial\psi(t,\mathbf{x})}{\partial t} = \frac{i}{\hbar}\Big(\frac{\hbar^2}{2m}\gamma(\mathbf{x})\frac{\partial^2}{\partial\mathbf{x}^2} - U(\mathbf{x})\Big)\psi(t,\mathbf{x}) \tag{4.38}$$

where $\gamma(\mathbf{x})$ is defined as

$$\gamma(\mathbf{x}) = \left(\frac{1}{1+R\sigma(\mathbf{x})}\right)^2 \tag{4.39}$$

$$\sigma(\mathbf{x}) = \sigma_0\big(\mathbf{x}-\mathbf{x}_{PML}\big)^2 \tag{4.40}$$

and σ_0 is a positive number, $\mathbf{x}_{PML}$ is the PML grid number and R is the complex parameter that is equal to $e^{i\pi/4}$.

Re-applying the complex function of ψ and γ on Equation 4.38, the new coupled equations are

$$\begin{aligned}\frac{\partial \psi_{re}(t,\mathbf{x})}{\partial t} &= \frac{1}{\hbar}\Big(-\frac{\hbar^2}{2m}\Big(\gamma_{im}(\mathbf{x})\frac{\partial^2 \psi_{re}(t,\mathbf{x})}{\partial \mathbf{x}^2} + \gamma_{re}(\mathbf{x})\frac{\partial^2 \psi_{im}(t,\mathbf{x})}{\partial \mathbf{x}^2}\Big)+ \\ &\qquad U(\mathbf{x})\psi_{im}(t,\mathbf{x})\Big)\end{aligned} \tag{4.41}$$

$$\begin{aligned}\frac{\partial \psi_{im}(t,\mathbf{x})}{\partial t} &= \frac{1}{\hbar}\Big(\frac{\hbar^2}{2m}\Big(\gamma_{im}(\mathbf{x})\frac{\partial^2 \psi_{re}(t,\mathbf{x})}{\partial \mathbf{x}^2} - \gamma_{re}(\mathbf{x})\frac{\partial^2 \psi_{im}(t,\mathbf{x})}{\partial \mathbf{x}^2}\Big)- \\ &\qquad U(\mathbf{x})\psi_{im}(t,\mathbf{x})\Big)\end{aligned} \tag{4.42}$$

General absorbing boundary condition (ABC)

The general ABC is based on exact solution of the wave equation. It is used in three dimensional simulation due to its efficiency. In fact, the implementation of the general ABC is only on the top and bottom surfaces or in other words it is only one directional ABC. The detail formulation is provided below.

$$\pm i\hbar\frac{\partial \psi(t,\mathbf{x})}{\partial \mathbf{x}} - i\hbar c_1\frac{\partial \psi(t,\mathbf{x})}{\partial t} + \Big(c_1 U(\mathbf{x}) - c_2\Big)\psi(t,\mathbf{x}) = 0 \tag{4.43}$$

where $c_1 = \dfrac{2}{v_1 + v_2}$ and $c_2 = \dfrac{m v_1 v_2}{v_1 + v_2}$. The v_i is the i-th group velocity of the traveling wave, which is defined as

$$v_i = \frac{2\hbar\pi}{m\lambda_i} \tag{4.44}$$

where λ_i is determined from the wave number $k_i = \dfrac{2\pi}{\lambda_i}$.

Consider complex function of ψ, Equation 4.43 can be split into two coupled equations as

$$\pm i\hbar\frac{\partial\psi_{re}(t,\mathbf{x})}{\partial\mathbf{x}} - i\hbar c_1\frac{\partial\psi_{re}(t,\mathbf{x})}{\partial t} + \Big(c_1U(\mathbf{x}) - c_2\Big)i\psi_{im}(t,\mathbf{x}) = 0 \tag{4.45}$$

$$\mp\hbar\frac{\partial\psi_{im}(t,\mathbf{x})}{\partial\mathbf{x}} + \hbar c_1\frac{\partial\psi_{im}(t,\mathbf{x})}{\partial t} + \Big(c_1U(\mathbf{x}) - c_2\Big)\psi_{re}(t,\mathbf{x}) = 0 \tag{4.46}$$

for real and imaginary functions, respectively, where the above sign is for right or top part and the below sign is for left or bottom part of the simulation domain.

4.3.6 Eigen Energies and Eigen Function Determinations

The purpose of solving Schrödinger equation is to determine the eigen energy and eigen function of the quantum structures. In order to do that, we consider the following procedure shown in the flowchart of Figure 4.5.

Generally, the eigen energy, ε_n, are obtained by exciting the region of the quantum structure by a narrow-time function. Notice that n denotes the level of the eigen energy. It is initialized to the time loop of discretized coupled Schrödinger equations. In the loop, the Hanning window is applied to ψ_{re} and ψ_{im} at representative point for every time step to smooth the time-domain data. This filter is formulated as

$$H(t) = \frac{1}{2}\bigg(1 - \cos\Big(\frac{2\pi M}{T_{max}}\Big)\bigg) \tag{4.47}$$

where M is the time iteration and T_{max} is the simulation time. The steady-state time-domain data is then stored. Next, Fourier transform is performed on the

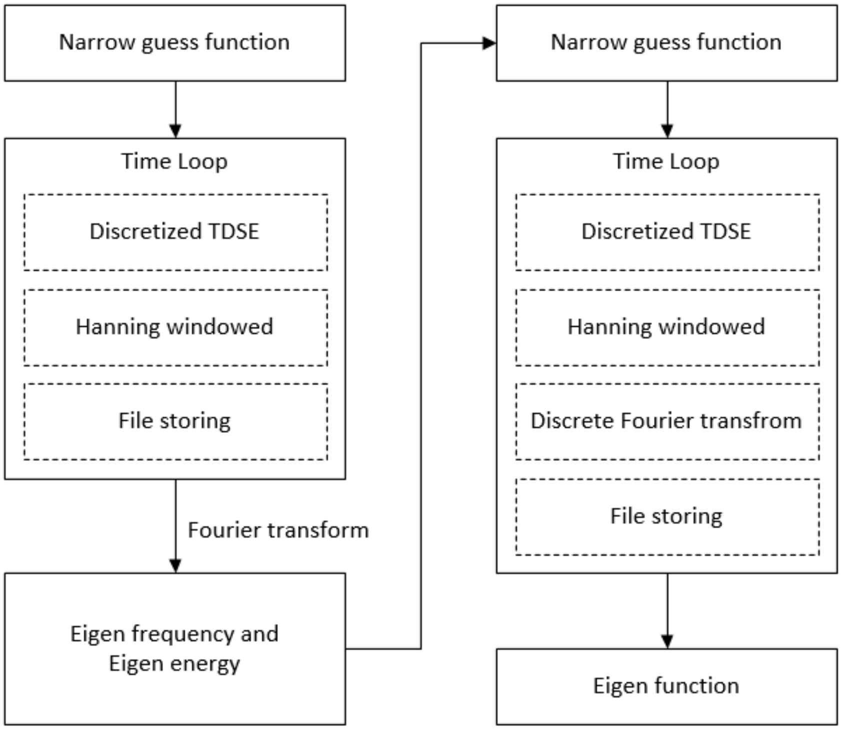

Figure 4.5: Flow diagram of eigen energy and eigen function calculations.

collected data to get eigen frequency, ω_n, and ε_n, which is defined as

$$\varepsilon_n = \hbar\omega_n \tag{4.48}$$

Furthermore, the eigen-functions, ϕ_n, can be constructed by applying the same initial function centered at a given eigen frequency. Discrete Fourier transforms of all points in space are then constructed using the following recursive calculations.

$$\phi_n^M(\mathbf{x},\omega_n) = \phi_n^{M-1}(\mathbf{x},\omega_n) + H(M\Delta t)\phi(\mathbf{x}, M\Delta t)\big(e^{-i\omega_n\Delta t}\big)^M \tag{4.49}$$

4.3.7 Discussion

In order to verify the model, a simple numerical test is conducted. The numerical result is compared to the analytical solution in terms of eigen energies. A symmetrical rectangular quantum well with infinite potential energy barriers is considered as a test domain as depicted in Figure 4.6

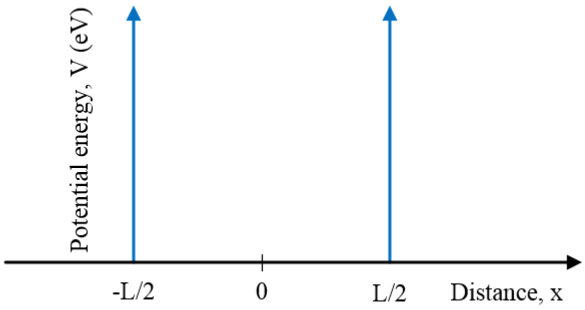

Figure 4.6: Rectangular quantum well with infinite potential energy barriers.

The analytical solution of this problem is determined by

$$\varepsilon_n = \frac{\hbar^2 n^2 \pi^2}{2mL^2} \tag{4.50}$$

where L is the thickness of the quantum well, 5 nm, and m is the effective mass, 0.17*m_0 kg. By applying a Gaussian test function at the middle of the simulation domain, the resulted eigen energies are comparable to the analytical solutions as listed in Table 4.1 and Figure 4.7(a). The first five eigen functions are also available in Figure 4.7(b).

Table 4.1: The first five eigen energies comparison of analytical and simulation result.

Level n	ε_n analytic (eV)	ε_n simulation (eV)	Absolute error (eV)
1	0.08847768492	0.09860199565	0.01012431073
2	0.35391073979	0.34510698479	0.00880375500
3	0.79629916427	0.78881596522	0.00748319905
4	1.41564295872	1.42972893697	0.01408597825
5	2.21194212299	2.21854490218	0.00660277919

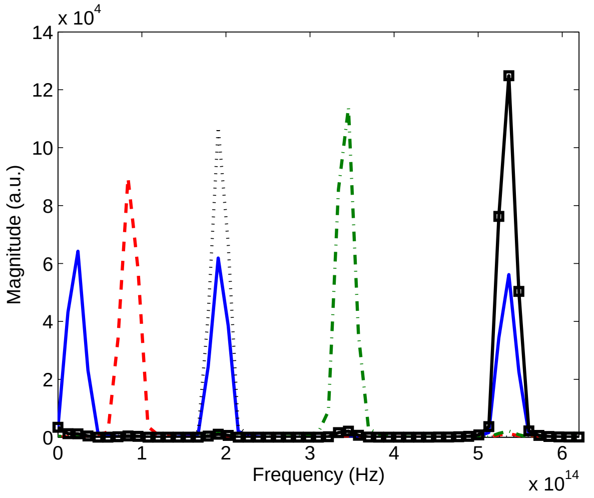

(a) Eigen energies

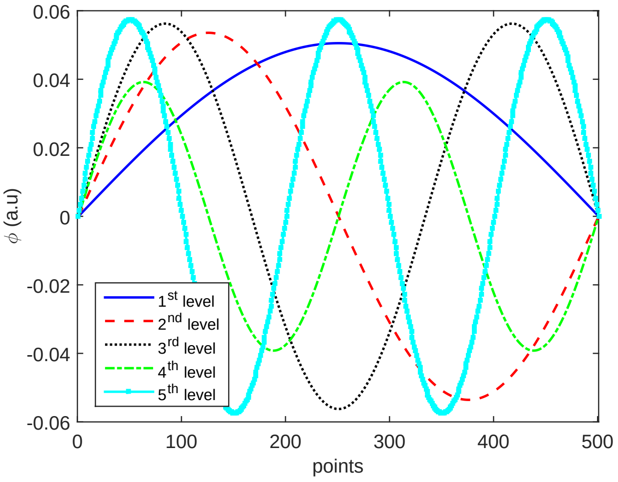

(b) Eigen functions

Figure 4.7: The first ε_n and ϕ_n of infinite well.

CHAPTER 5

ONE DIMENSIONAL INTERMIXING PROCESS IN QD-NW SIMULATION

The numerical solution of one dimensional intermixing process is given in this chapter. The details of the structure and parameters are listed including material properties such as electron and hole masses, band gap and bowing parameter of GaN and InN. The parametric studies are considered by varying quantum well thickness, as grown quantum well shape, initial indium concentration, annealing time and temperature and polarization percentage.

5.1 $GaN/InGaN$ Single Quantum Well (SQW)

The three dimensional schematic of $GaN/InGaN$ QD-NW is shown in Figure 5.1. The one dimensional structure is taken along the z-axis of the three dimensional schematic with additional 100 points for Perfect Matching Layer (PML) as depicted in Figure 5.2. The detail parameters are tabulated in Table 5.1.

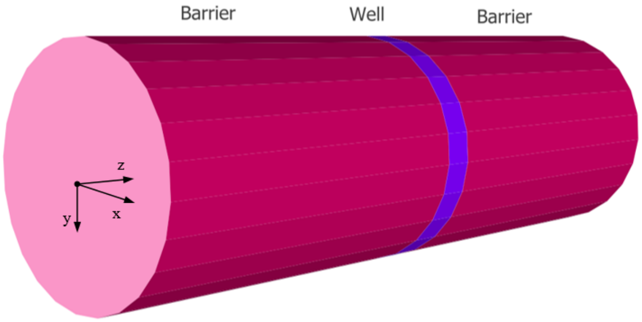

Figure 5.1: Three dimensional Single QD-NW structure.

Figure 5.2: One dimensional SQW structure.

Table 5.1: Parameter of one dimensional simulation.

Properties	Well	Barrier
Material	GaN	$InGaN$
Length	3 nm	17 nm
m_{ee} (effective mass of electron)	0.20*m_0	0.11*m_0
m_{hh} (effective mass of heavy hole)	1.40*m_0	1.63*m_0
m_{lh} (effective mass of light hole)	1.40*m_0	1.63*m_0
x (initial indium mole fraction)	0	0.20369149

5.1.1 Polarization Percentage Effects

The total polarizations calculated using the presented model are usually greater than experimental result especially for $GaN/InGaN$ heterostructure. It is usually between 20-80% of the model. Hence, the studies of polarization percentages effects on electrostatic voltage (V), conduction and valence potential energy bands (U_c and U_v), eigen energy and eigen function are conducted in this subsection.

Considering Poisson equation of polarization model, it is clear that the polarization affects the electrostatic voltage proportionally. Figure 5.3 shows that the maximum voltage, around 0.5 V, is captured when the 100% of the polarization model is taken. It decreases up to 0.09 V for 20% polarization percentage.

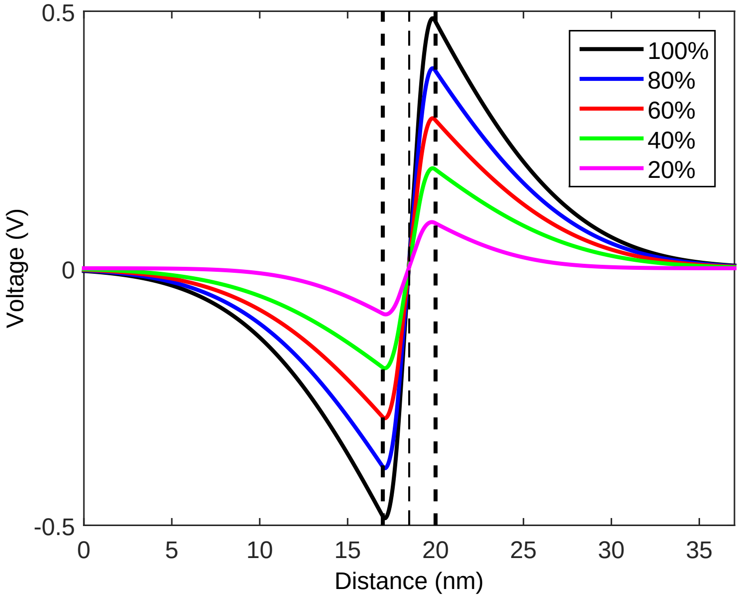

Figure 5.3: Polarization percentage effect on electrostatic voltage.

It also affects the conduction and valence potential energy band profiles as shown in Figure 5.4(a) and 5.4(b), respectively. It shows that the potential well is not square anymore. The change of U_c and U_v automatically affects the eigen energies since the Schrödinger equation accounts for the potential energy. Figure 5.5(a) shows the shifting of emission wavelength due to the change of the ground state of eigen energies. Not only that, but the eigen function is also affected significantly as depicted in Figure 5.5(b).

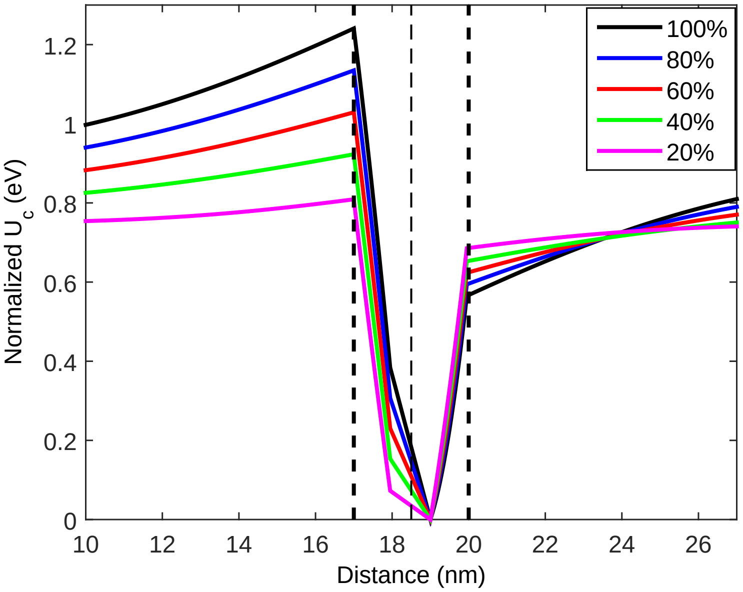

(a) Conduction potential energy band

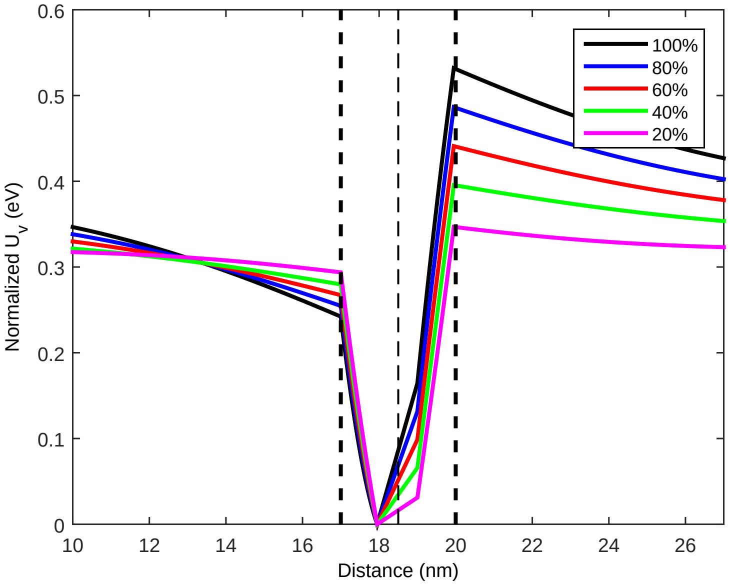

(b) Valence potential energy band

Figure 5.4: Polarization percentage effect on U_c and U_v

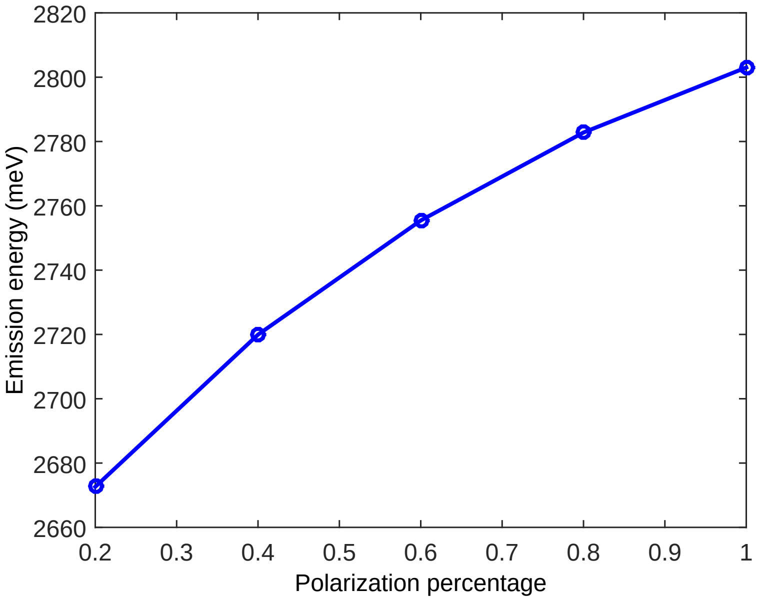

(a) Eigen energy shifts

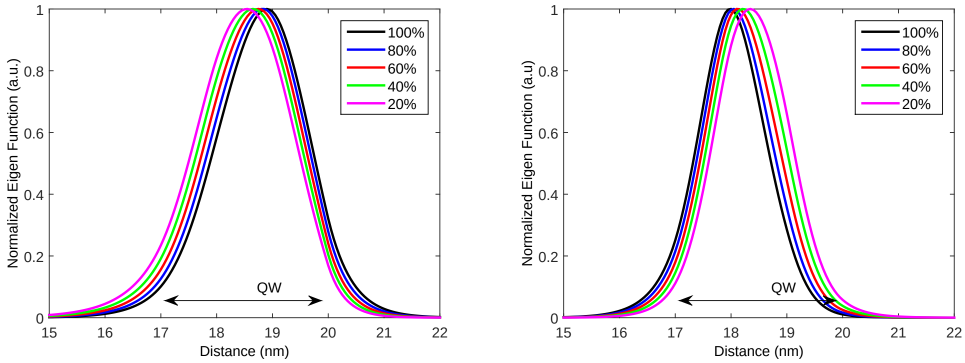

(b) Eigen functions of electrons (left) and holes (right)

Figure 5.5: Polarization percentage effect on eigen energy shifts and eigen functions

5.1.2 Quantum Well Shape Effects

As mentioned earlier, trapezoidal quantum well shape is considered in this thesis. In order to study the effect of quantum well shape, two categories are considered, i.e. symmetric and asymmetric trapezoidal quantum well shapes. The symmetry in this case is based on the ramp slopes of the trapezoidal shape. There are five tested shapes:

- Shape 1: Symmetric shape with $a = 1nm$, $b = 1nm$ and $c = 1nm$.
- Shape 2: Symmetric shape with $a = 0.5nm$, $b = 2nm$ and $c = 0.5nm$.
- Shape 3: Symmetric shape with $a = 0.75nm$, $b = 1.5nm$ and $c = 0.75nm$.
- Shape 4: Asymmetric shape with $a = 0.75nm$, $b = 1.25nm$ and $c = 1nm$.
- Shape 5: Asymmetric shape with $a = 1nm$, $b = 1.25nm$ and $c = 0.75nm$.

where a, b and c are explained in Figure 5.6

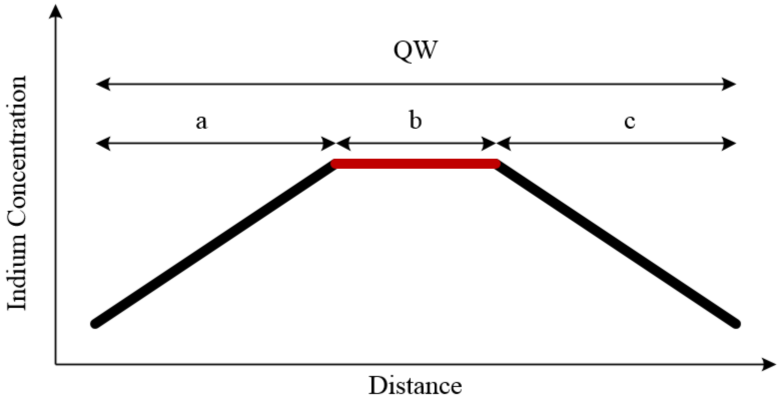

Figure 5.6: Schematic of trapezoidal quantum well shape.

Initial profile of indium concentration will determine the interdiffusion coefficient due to its dependency on concentration. Thus, the as grown profile of the indium concentration will determine the final interdiffused profile. As we can see in Figure 5.7, the symmetric as grown trapezoidal profiles are always symmetrical even after intermixing so is the whole asymmetric category.

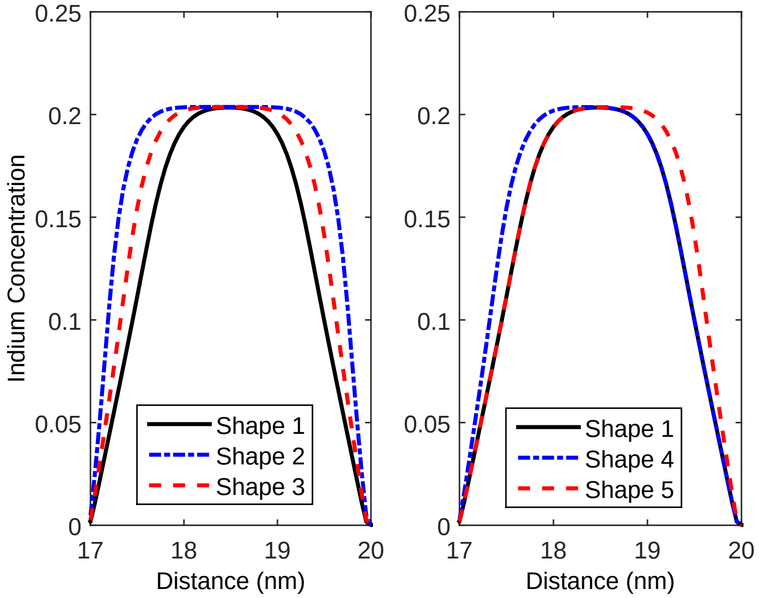

Figure 5.7: Interdiffused indium concentration of trapezoidal quantum well shapes.

The potential energy bands, U_c and U_v, for as grown case are shown in Figure 5.8. In case of symmetrical trapezoidal structures, the longer b gives higher potential energies, as in Figure 5.8(a) and 5.8(c). However, asymmetric shapes give different contributions. The U_c is increasing as the b part of trapezoidal shape is longer. On the contrary, the U_v is higher if the b part is less than c as shown in Figure 5.8(b) and 5.8(d). It does not only occur in as grown case but also in interdiffused case as can be seen in Figure 5.9

Looking at the eigen energies, the asymmetric trapezoidal profiles, Shape 4 and 5, give the same emission energy and relatively higher than the symmetric

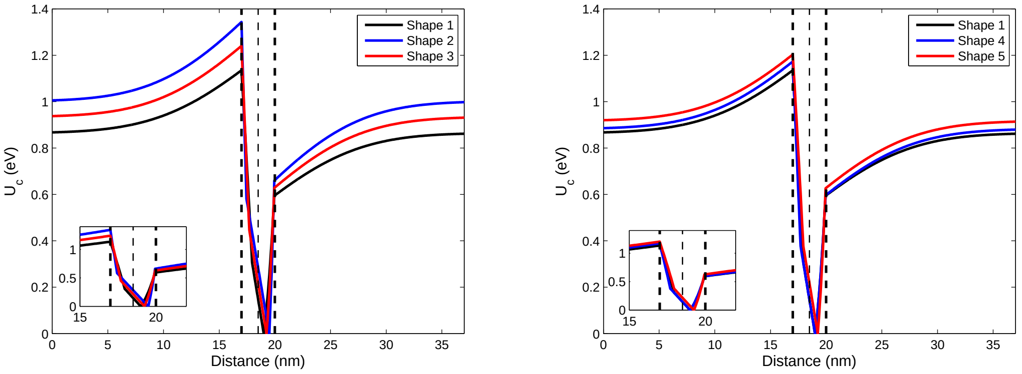

(a) U_c Shape 1, 2 & 3 (b) U_c Shape 1, 4 & 5

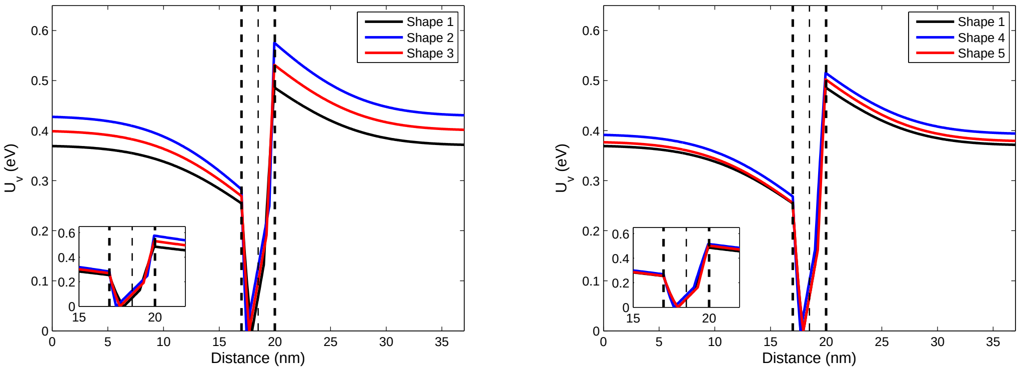

(c) U_v Shape 1, 2 & 3 (d) U_v Shape 1, 4 & 5

Figure 5.8: As grown conduction and valence potential energy bands.

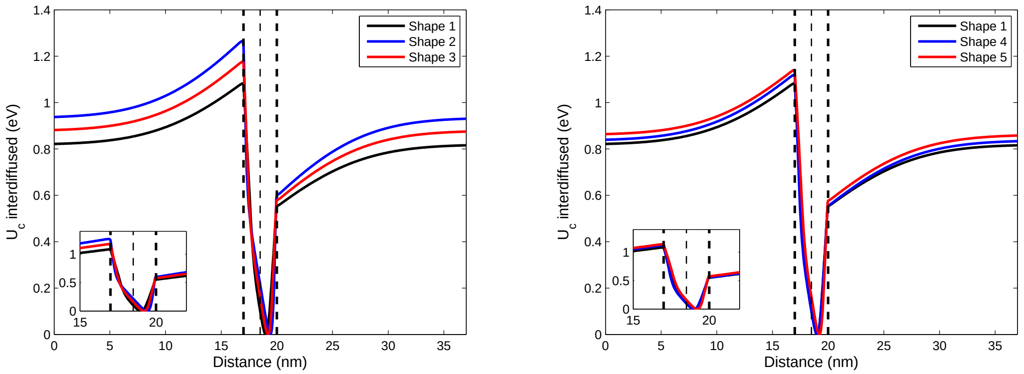

(a) Intermixed U_c Shape 1, 2 & 3 (b) Intermixed U_c Shape 1, 4 & 5

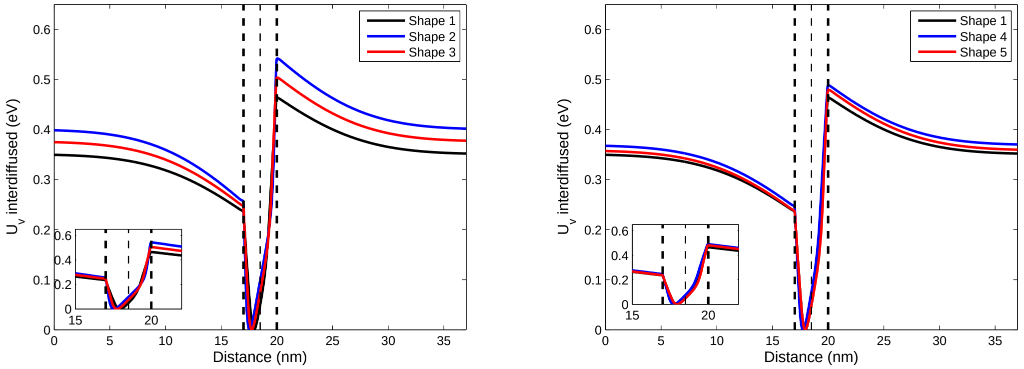

(c) Intermixed U_v Shape 1, 2 & 3 (d) Intermixed U_v Shape 1, 4 & 5

Figure 5.9: Conduction and valence potential energy bands after interdiffusion.

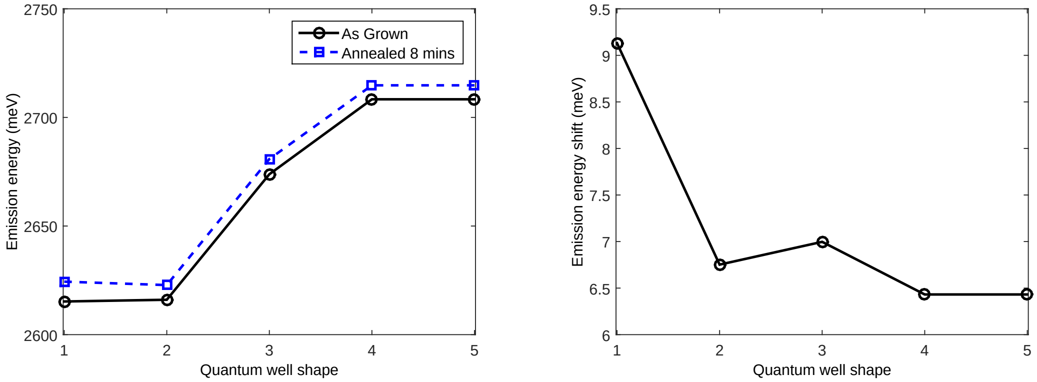

(a) Emission energy (b) Emission energy shift

Figure 5.10: Quantum well shape effects on emission energy and its shift.

trapezoidal profiles as shown in Figure 5.10(a). However, after 8 minutes annealing process under temperature 950 ^oC, the asymmetric trapezoidal profiles show the least energy shifts compared to as grown unlike Shape 1, which gives the largest energy shift as depicted in Figure 5.10(b). In the case of eigen function, the length of b part in the symmetric trapezoidal profiles drives the shift of eigen function consistently.

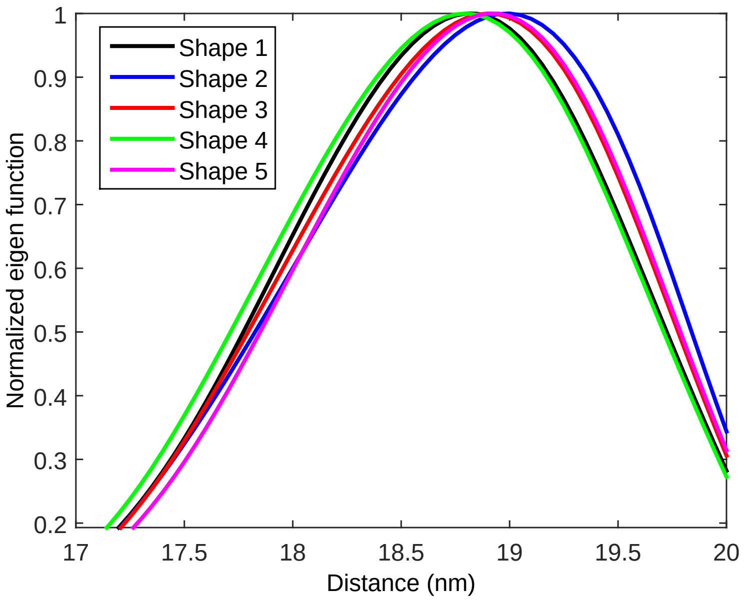

Figure 5.11: Quantum well shape effect on eigen function.

5.1.3 Annealing Time and Temperature Variations

Annealing treatment to induce the intermixing process in nanostructures is very crucial. Annealing time and annealing temperature are two parameters that can be adjusted in experiment. Thus, the study of annealing time and temperature is conducted.

Variation of annealing time and temperature are taken as 4, 8 and 12 minutes and 850, 900 and 950 ^{o}C, respectively. Figure 5.12 describes the energy shifts of the emission of the SQW for all variations. The shift is higher as the annealing time is longer or the temperature increases. In fact, the slope of the shift of each temperature variation is unequal due to the exponential model of the interdiffusion coefficient on temperature. The higher annealing temperature allows atoms to interdiffuse faster and yields higher eigen energy.

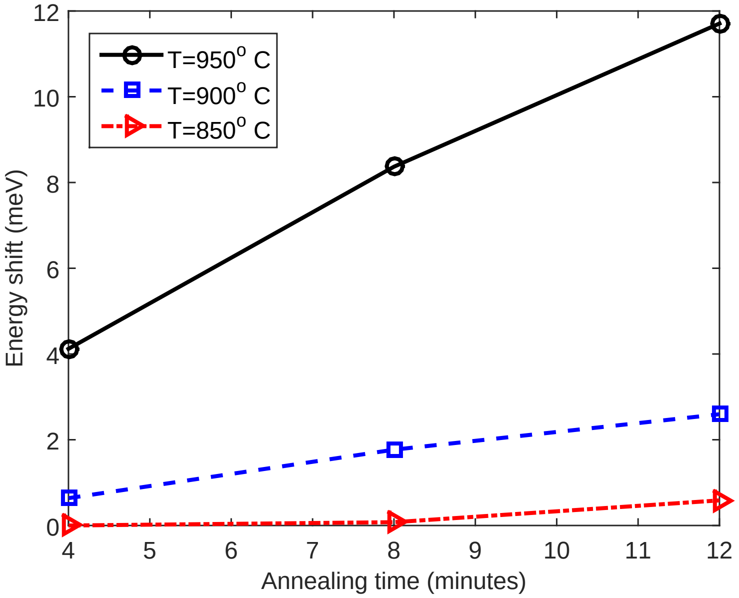

Figure 5.12: Eigen energy shifts due to annealing time and temperature variations.

5.1.4 Initial Indium Concentration Variations

Another important parameter is the profile of indium concentration of as grown SQW due to the dependency of interdiffusion coefficient on concentration. As an evidence, Figure 5.13 shows the energy shift for different initial indium concentration profile. The numbers mentioned in the figure show the initial indium mole fraction in b zone of trapezoidal quantum well region. It can be concluded that the energy shift magnitude and the slope are proportional to the initial indium profile.

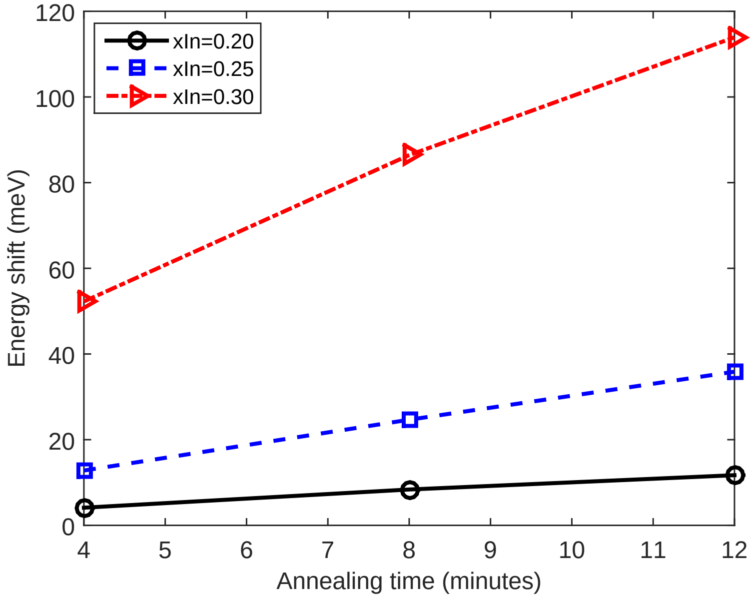

Figure 5.13: Eigen energy shifts due to as grown indium concentration variations.

5.1.5 Well Thickness Variations

Next, as explained in Chapter 1 about quantum structures, the thickness of quantum well affects the confinement of particles, i.e. electrons and holes. In order to study the effects of well thickness, W, on the intermixing process as well as quantum properties, we vary the W to be 3 nm, 5 nm (a and c are 1.5 nm) and 7 nm (a and c are 2.0 nm).

In Figure 5.14, the energy shifts are shown. The largest shift occurs on the most narrow well thickness for all temperature variations. It means that the electrons and holes are well-trapped in tight structure.

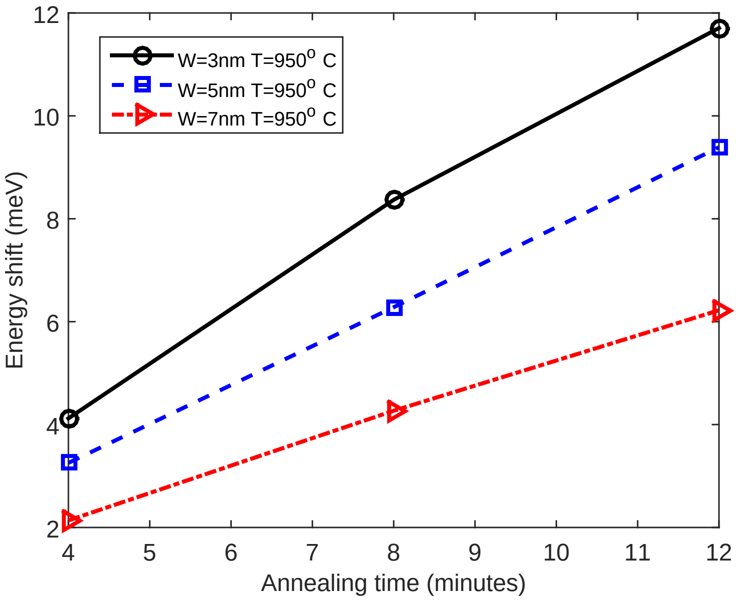

Figure 5.14: Eigen energy shifts due to quantum well thickness variations.

5.1.6 Experimental Verification

As mention in Chapter 3 section 3.3, the coefficients of prefactor interdiffusion coefficient, D_1 and D_2, are readjusted in this section due to the huge difference between experimental data and simulation. The redesign of $D_0(c)$ is formulated as

$$D_0(c) = D_3 D_2 \exp(D_1 c) \tag{5.1}$$

where D_3 is adjustable constant.

As we can see in Figure 5.15, by adjusting the value of D_3 to 50, the errors are still big but the slope of the shift is close to the experiment. Attempting to decrease the error for 4 minutes annealing time by increasing D_3 up to 400, the slope of the shift escalates with time. It is difficult to drive the slope to be close to the experiment due to the fact that the dependency of the coefficient on concentration is in exponential function. Figure 5.16 shows the fitting for other temperatures, 850 and 950 ^oC, with D_3 is equal to 200.

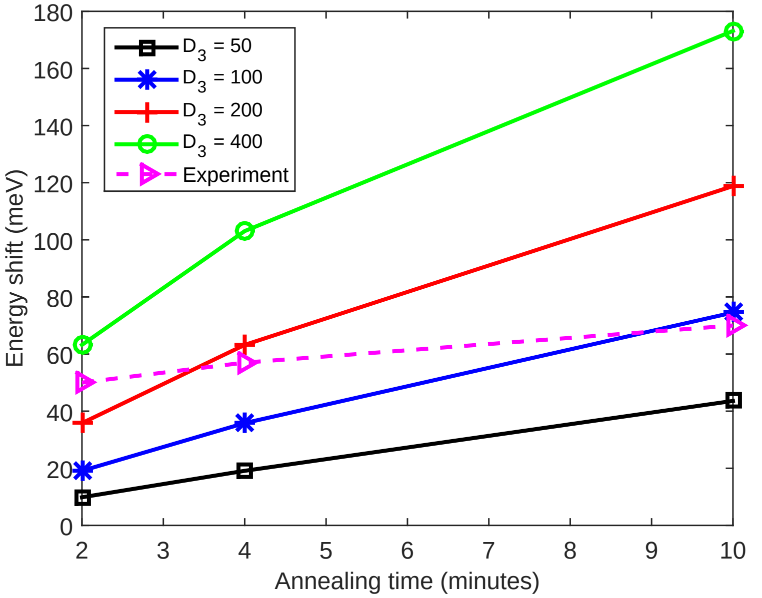

Figure 5.15: Variation of D_3 as fitting constant to the experimental data.

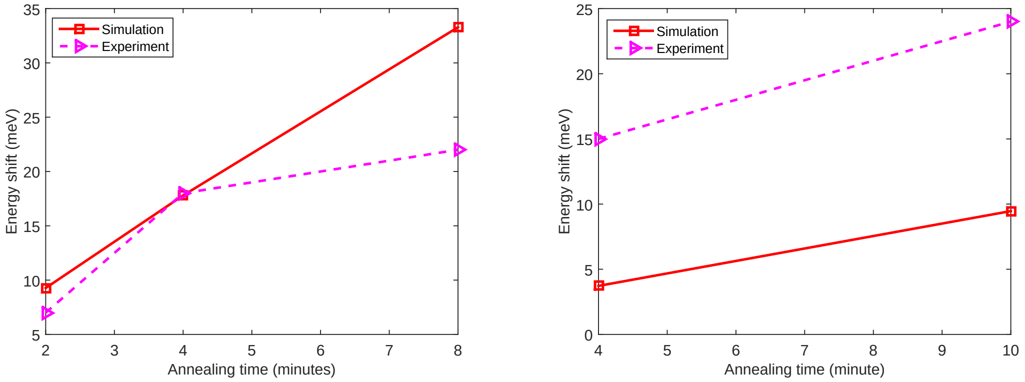

(a) 900 ^oC (b) 850 ^oC

Figure 5.16: Comparison between simulation and experiment results for 850 and 900 ^oC annealing temperatures.

The function of $D_0(c)$ is also varied in order to achieve minimum error. Figure 5.17 shows three representations of prefactor, D_1c, D_1c^2 and D_1c^3, including variation of the parameter, D_1. The results show similar trend in comparison to previous result. The slope increases as the parameter increases for all functions.

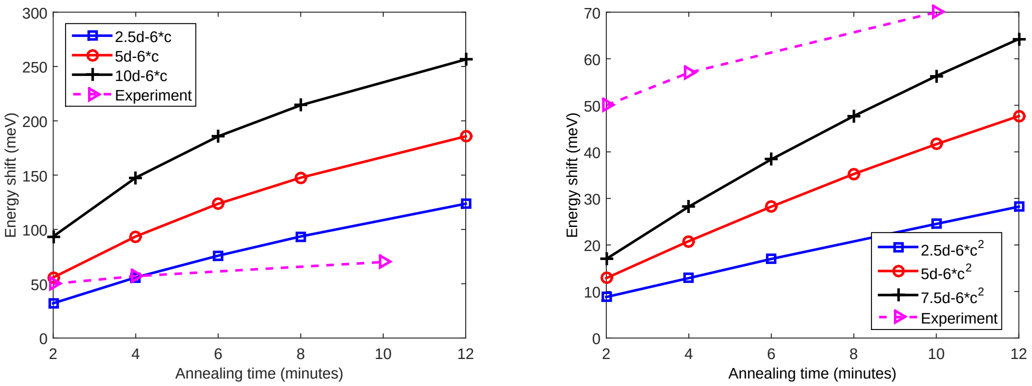

(a) $D_0(c) = D_1 c$ (b) $D_0(c) = D_1 c^2$

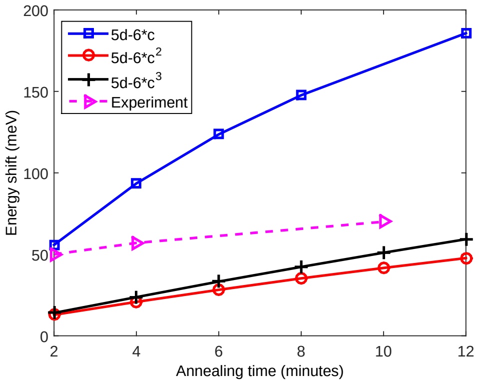

(c) $D_0(c) = D_1 c^3$

Figure 5.17: Variation of $D_0(c)$.

5.2 $GaN/InGaN$ Multiple Quantum Well (MQW)

The number of disks in QD-NW might actually give contribution to the interdiffusion process. Multiple disks in a nanowire provides more interfaces and consequently affects the movement of atoms. Moreover, spontaneous and piezoelectric polarizations are also increased and change the portion of electrostatic voltages. At the end, the energy band is changed.

In order to study the effect of multiple disks, we consider MQW in one dimensional representation of QD-NW with multiple disks. Figure 5.18 describes the schematic of MQW with 2 wells. The general structural parameters are the same as SQW problem previously studied.

Figure 5.18: One dimensional MQW structure.

5.2.1 Well Separation Variations

The distance between the two wells can be used as a parameter to study well-coupling and its effects. Distinguishing coupled and uncoupled wells can be seen through the eigen functions. The overlaps between single well eigen function gives rise to the formation of coupled wells. In this study, the separation of the wells is varied to be 5, 7 and 9 nm. Figure 5.19(a) and 5.19(b) shows the eigen functions of double quantum well for electrons and holes, respectively. As we can observe, in several cases, the tails of eigen functions overlap in the case of 5 and 7 nm separation lengths.

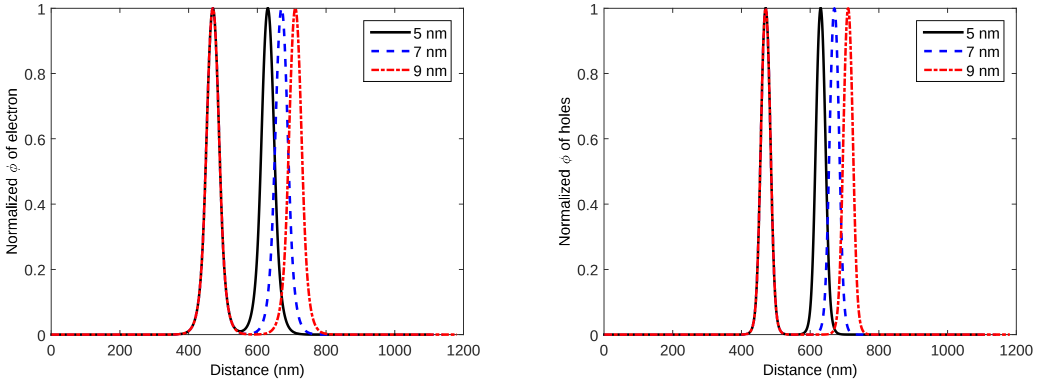

(a) Electrons

(b) Holes

Figure 5.19: Normalized eigen functions of electron in MQW.

CHAPTER 6

THREE DIMENSIONAL INTERMIXING PROCESS IN QD-NW SIMULATION

The results of one dimensional simulation of intermixing phenomenon in QD-NW has been presented in Chapter 5. There are several reasons that the attempt to build a multi dimensional solver is needed.

- One dimensional solution might not fully represent the QD-NW due to its cylindrical structure. The round-edges of the domain can not be simply reduced to one dimension.

- In order to study of Nanowire (NW) diameter effects, the finite x and y-axes must be accounted for in the simulation.

In fact, the three dimensional solver consumes more computation time and size. However, there have been terrific improvement in computation both in hardware and software. Thus, the simulation time can be reduced by applying parallel computing. Moreover, the values of Δx, Δy and Δz can be adjusted. In this

Table 6.1: Parameter of three dimensional simulation.

Properties	Value	Unit
Barrier material	GaN	-
Disc material	$InGaN$	-
Barrier length	12	nm
Disc thickness	3	nm
NW diameter	4/8/20	nm
Air thickness	3	nm
Initial indium concentration	0.20369149	-
$a-b-c$ trapezoidal lengths	1-1-1	nm
Δx-Δy-Δz	0.5-0.5-0.1	nm

chapter, the three dimensional solution of intermixing process and related phenomena in $GaN/InGaN$ single disk of QD-NW is conducted. The structure of the QD-NW in three dimensions follows the schematic in Figure 5.1 with parameters as listed in Table 6.1. Figure 6.1 shows the sample of three dimensional simulation domain for the case of 20 nm diameter. The values in x, y and z-axes represent the discretization points.

6.1 Three Dimensional Interdiffusion Solution

According to the model, the divergence operator indicates that the distribution of indium concentration in all directions can significantly affect the movement of atoms. The contribution of x and y-axes to the intermixing process might be large if the gradient of the concentrations are also large or there are out forces that induce the atom movements such as in the case of capping layer method.

Figure 6.2(a) and 6.2(b) show the three dimensional visualization of as grown indium concentration profiles of the QD-NW with 20 nm diameter, y and z-axes

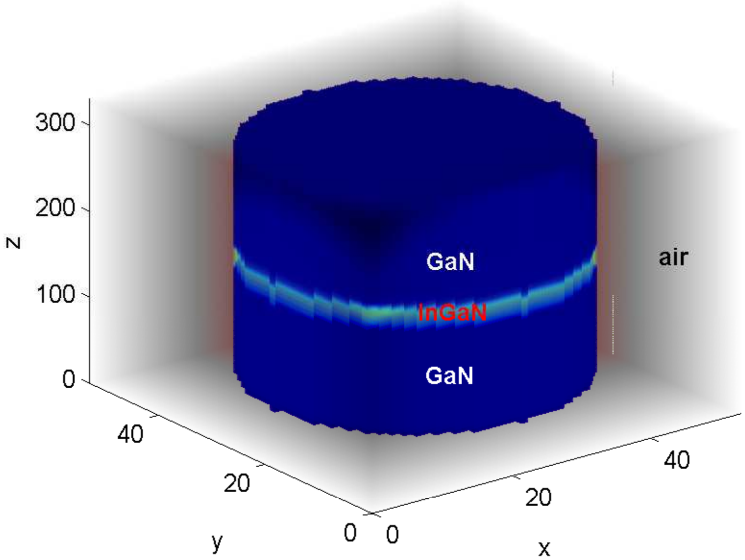

Figure 6.1: Three dimensional simulation domain.

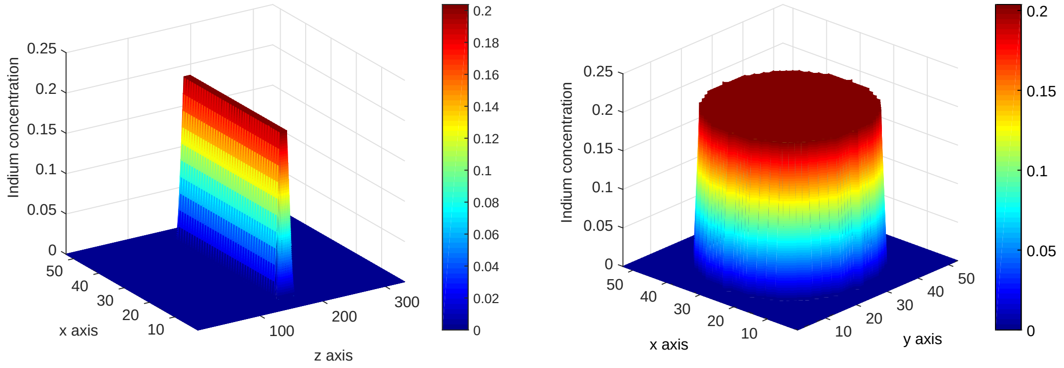

(a) y-axis slice

(b) z-axis slice

Figure 6.2: As grown indium concentration profile.

slices, respectively. Applying annealing temperature at 950 ^oC for 8 minutes, the staggered concentration profile of indium (y-slice) is depicted in Figure 6.3. The comparison of 1D and 3D indium concentration profile after intermixing shown in Figure 6.4 that describes that the contribution of interdiffusion in x and y-axes are nearly zeros since there is slight difference between the two.

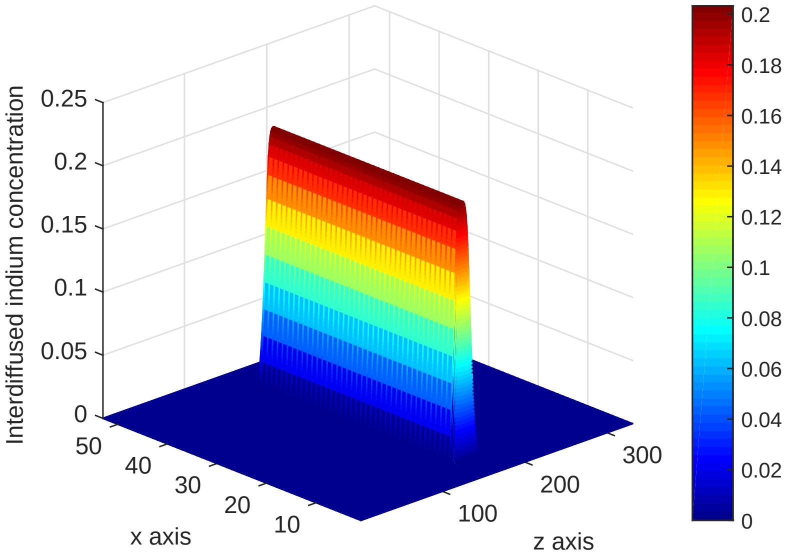

Figure 6.3: Interdiffused indium concentration profile (y-axis slice).

6.2 Three Dimensional Polarization Effects Solution

Next, the distribution of indium concentration in the previous chapter is used to calculate the electrostatic voltages. The profile of P_{tot} in Figure 6.5 shows us that the total polarization for as grown and intermixed follow the concentration profiles respectively.

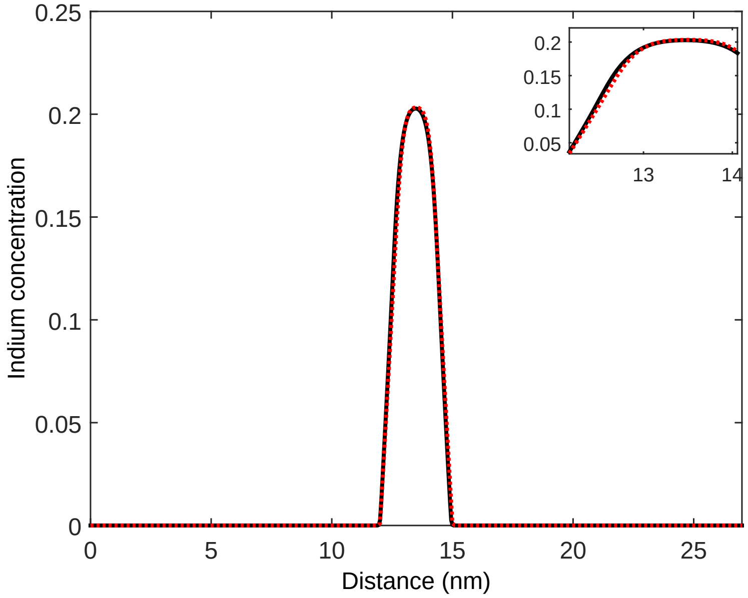

Figure 6.4: 1D and 3D interdiffused indium concentration profile comparison.

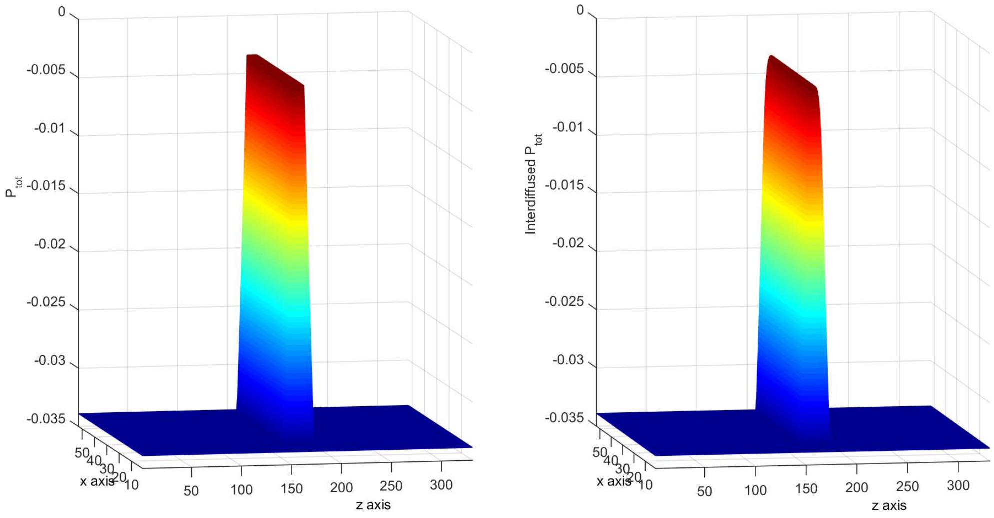

Figure 6.5: As grown and interdiffused total polarization profile.

Furthermore, considering 80% polarization percentage, Figure 6.6 shows the distribution of electrostatic voltages both for as grown and interdiffused. The profile is now used to calculate the distribution of U_c and U_v. Figure 6.7 and 6.8 show the comparison of as grown and interdiffused U_c and U_v.

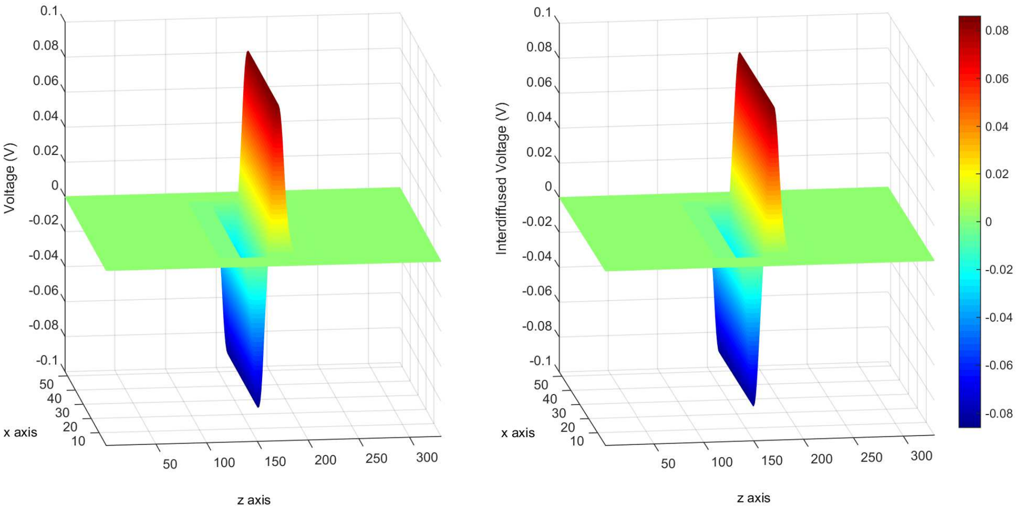

Figure 6.6: As grown and interdiffused electrostatic voltage profile.

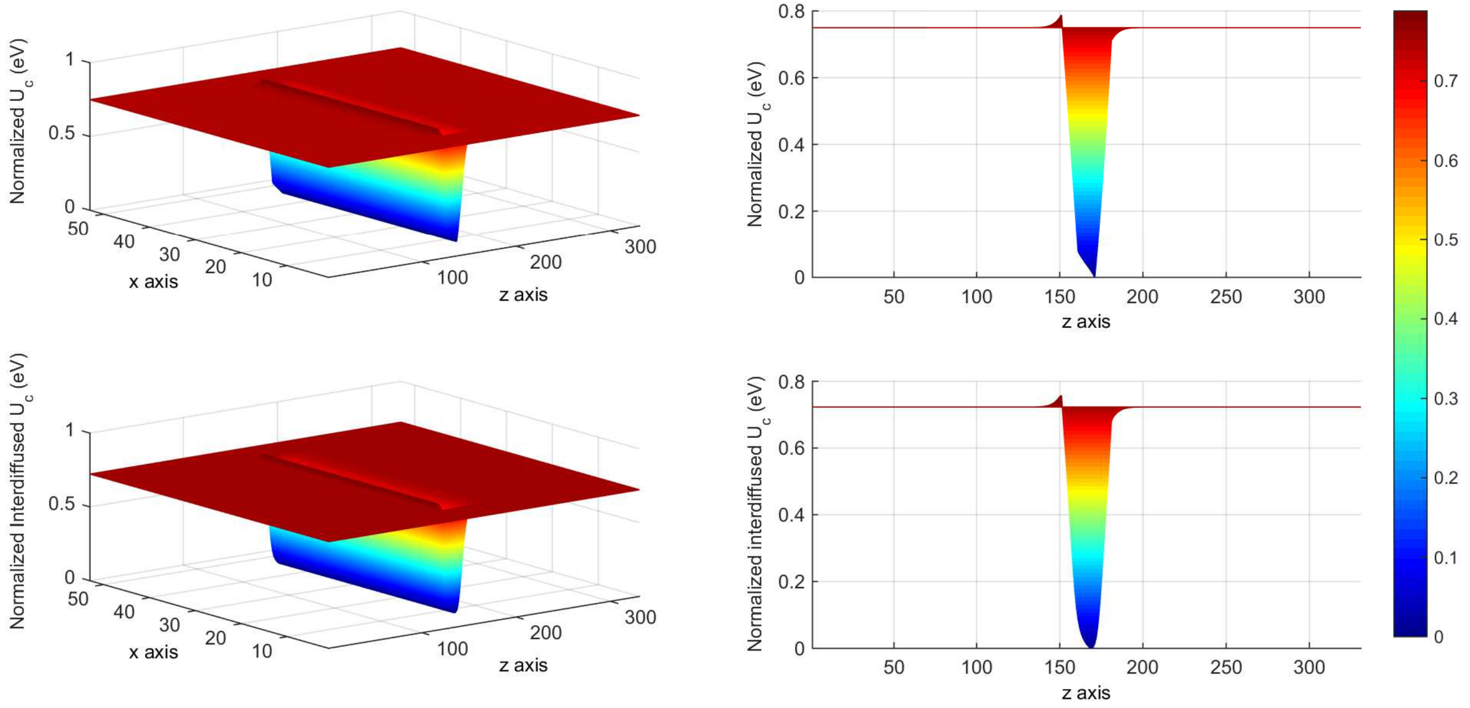

Figure 6.7: As grown and interdiffused U_c profile.

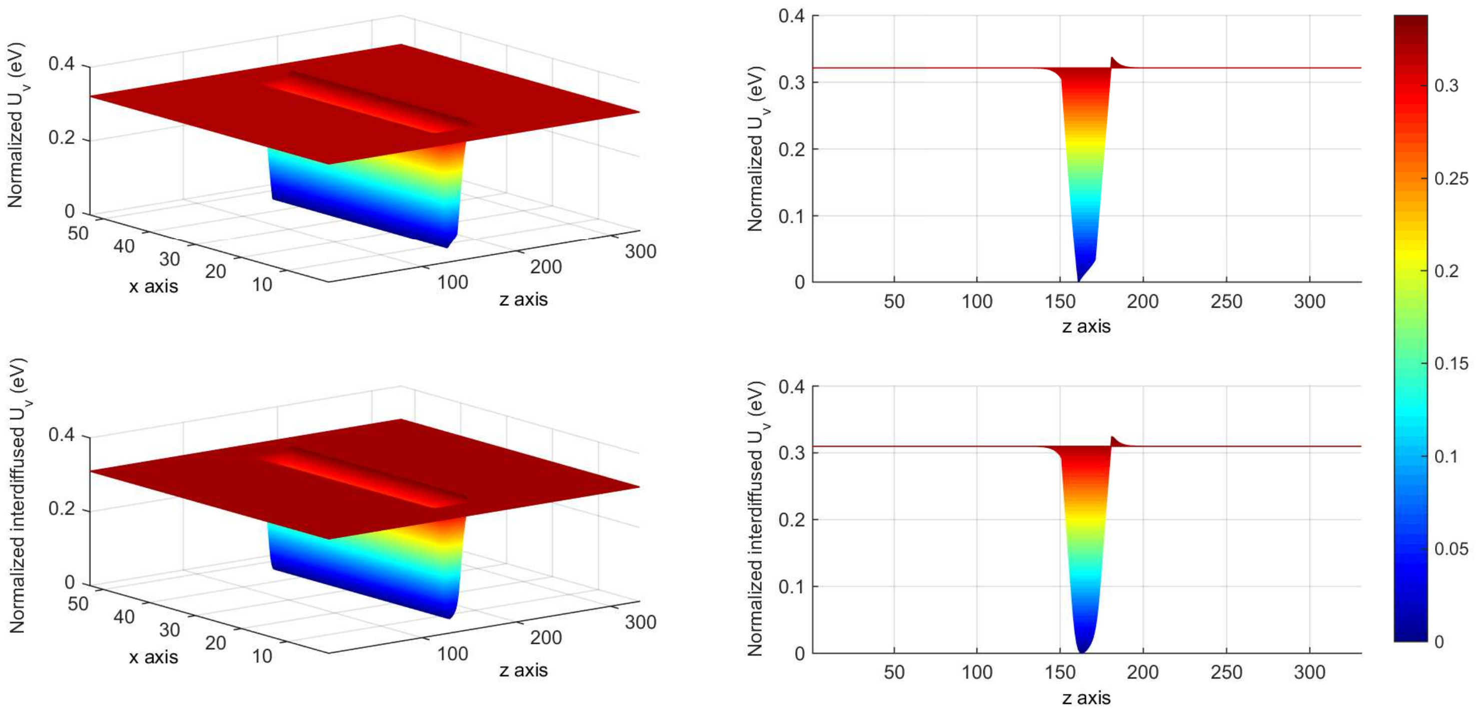

Figure 6.8: As grown and interdiffused U_v profile.

6.3 Three Dimensional Schrödinger Equation Solver Verification

In order to verify the three dimensional solver for Schrödinger equation, a rectangular prism infinite well is considered as depicted in Figure 6.9. The dimensions and material parameters are selected to be equal to the problem that has been presented by Sullivan et.al in [35]. The material is *GaAs* with effective mass of electron is equal to 0.067*m_0.

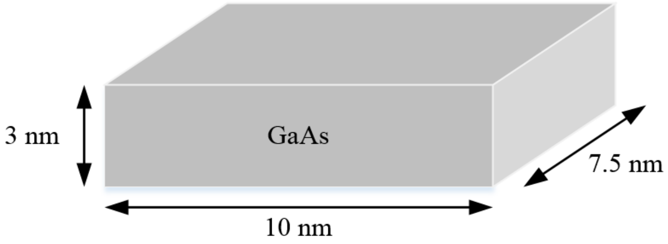

Figure 6.9: Three dimensional rectangular infinite well diagram.

The eigen energies of a three dimensional infinite well can be calculated by the following equation:

$$\varepsilon(n_x, n_y, n_z) = \frac{\hbar^2\pi^2}{2m}\left[\left(\frac{n_x}{L_x}\right)^2 + \left(\frac{n_y}{L_y}\right)^2 + \left(\frac{n_z}{L_z}\right)^2\right] \tag{6.1}$$

where L is the length of the well and n is the integer number of the modes. The subscripts x, y and z on L and n represent the axes.

Considering this, the eigen energies from QFDTD solver are compared to analytical solutions based on Equation 6.1 and solutions based on Sullivan in [35] as tabulated in Table 6.2. The error between analytical solutions and QFDTD solutions is very minor, which is not more than 1%, and so with the error between Sullivan and QFDTD solutions. Figure 6.10 shows the difference of the eigen energies between the three solutions.

Table 6.2: The first ten eigen energies of three dimensional infinite well.

Mode (n_x,n_y,n_z)	Analytic	Sullivan	Our Simulation
111	779.4987	775	775.7
211	947.8704	942	944.0
121	1078.8262	1072	1074.1
311	1228.4899	1220	1222.7
221	1247.1979	1242	1241
331	1527.8174	1520	1521.1
131	1577.7053	1565	1567.1
411	1621.3572	1610	1610.5
231	1746.0770	1735	1734.1
421	1920.6847	1908	1908.9

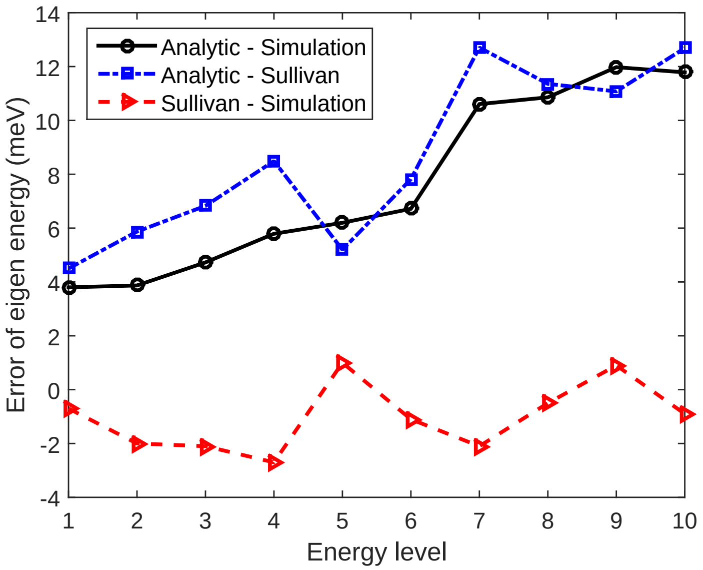

Figure 6.10: Error of eigen energy between analytical, Sullivan and QFDTD solutions.

6.4 Nanowire Diameter Variation

The QD-NW is characterized by the circular bounded structure. It gives distinctive characteristic to the emission properties. In order to study the contribution of it, the variation of NW diameters is studied. It is varied to be small (4 nm), medium (8 nm) and large (20 nm) diameters.

6.4.1 Energy Shift

Clearly, Figure 6.11 shows the significant effect of diameter to the electrons-holes confinements. The energy shift of the emission is larger as the nanowire is shrank in the circular direction. In the case of small diameter, the confinement is not only in z-axis but also x and y-axes. It is more like quantum dot, which is the confinement in all directions.

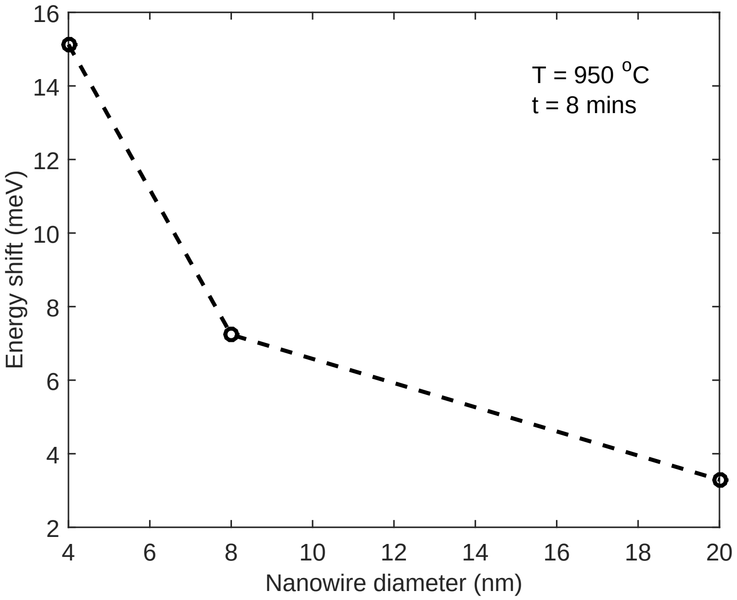

Figure 6.11: Energy shift due to nanowire diameter variations.

6.4.2 Eigen Functions

The occurrence of energy shifting due to diameter shrinking can be linked to the fact that eigen functions for each diameter value is different. Obviously, the eigen function of smaller diameter is more narrow compared to medium and large sizes. It also explains why the eigen energy in 4 nm diameter QD-NW is higher. Figure 6.12, 6.13 and 6.14 show the corresponding ground state eigen function visualizations, both 2D and 3D, for 4, 8 and 20 nm respectively.

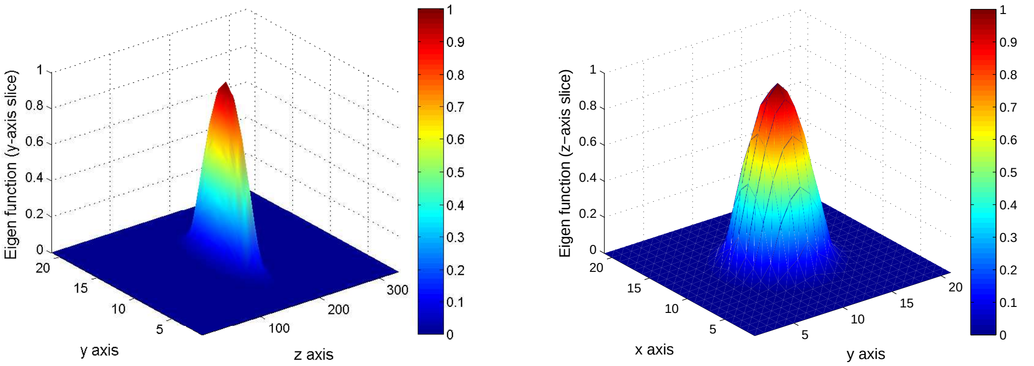

(a) 2D y-slice (b) 2D z-slice

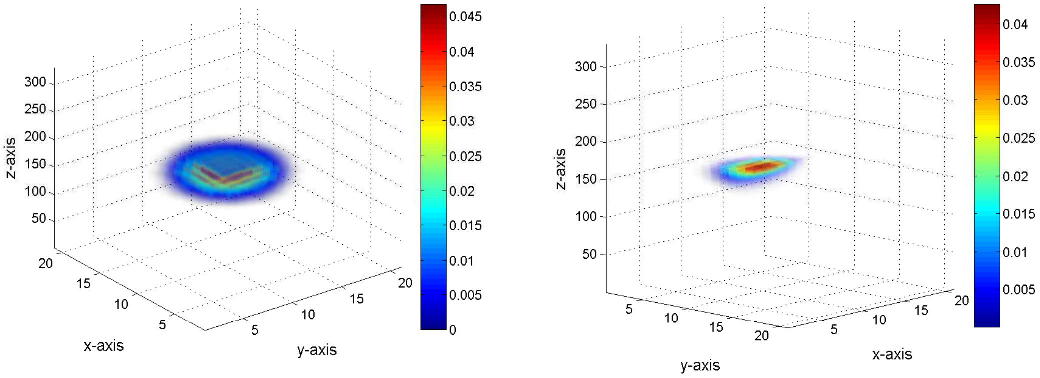

(c) 3D Full (d) 3D Half

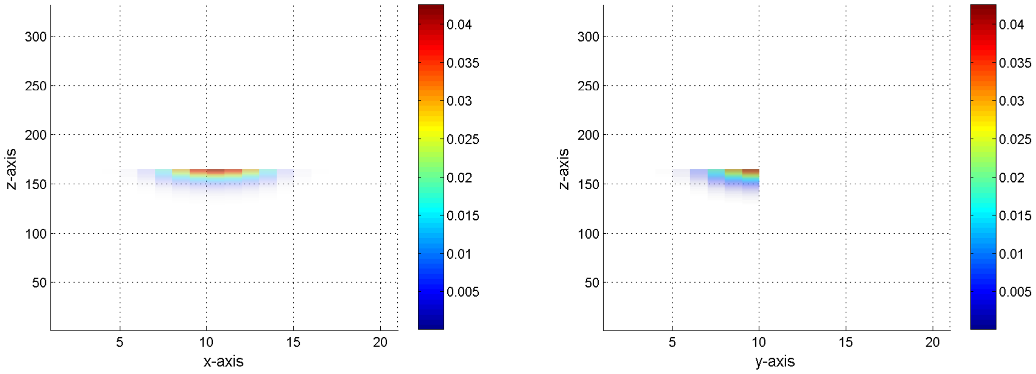

(e) 3D Half yz-view (f) 3D Half xz-view

Figure 6.12: Two & Three dimensional normalized eigen functions visualization of as grown QD-NW 4 nm diameter.

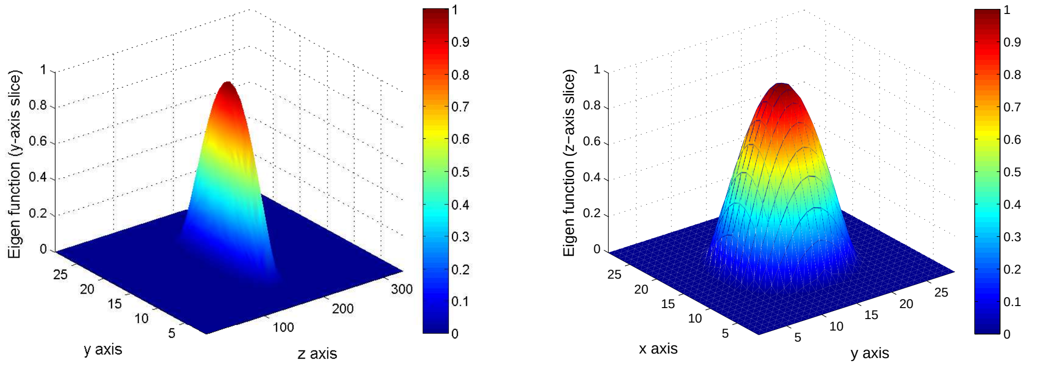

(a) 2D y-slice (b) 2D z-slice

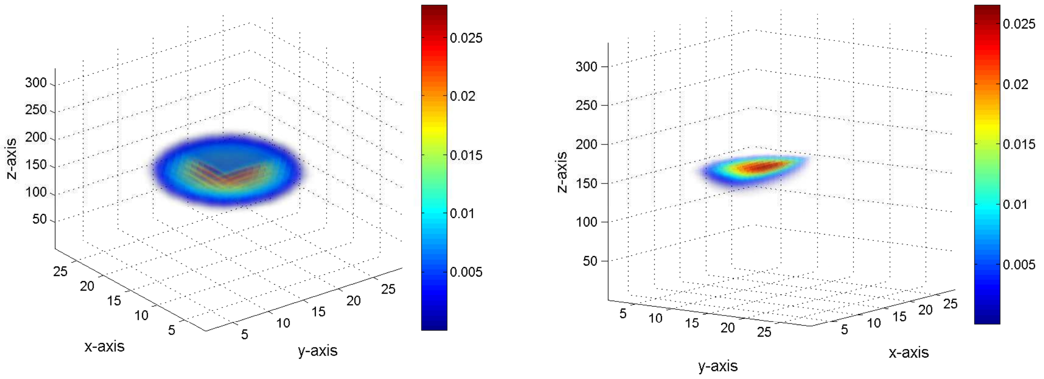

(c) 3D Full (d) 3D Half

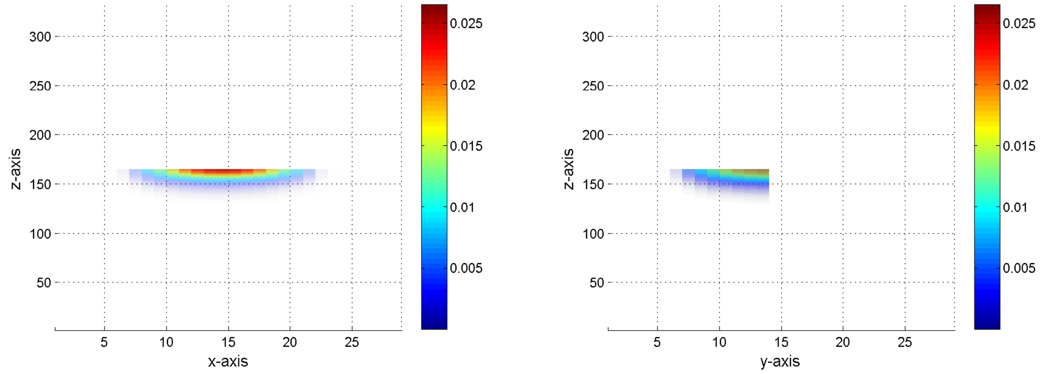

(e) 3D Half yz-view (f) 3D Half xz-view

Figure 6.13: Two & Three dimensional normalized eigen functions visualization of as grown QD-NW 8 nm diameter.

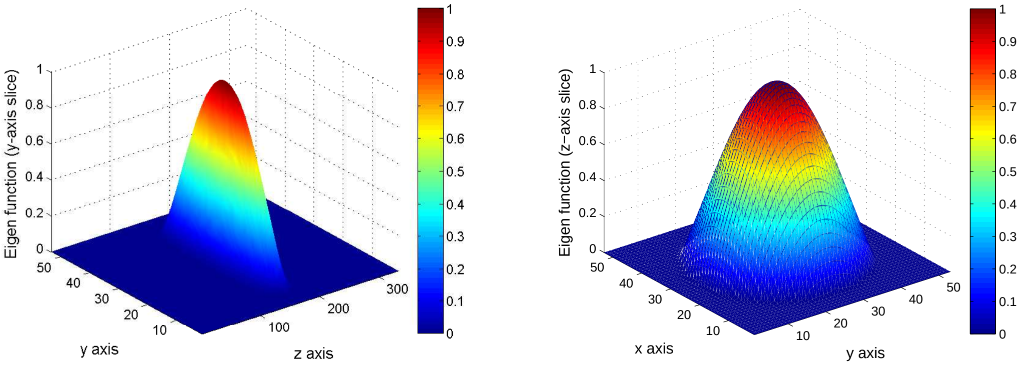

(a) 2D y-slice

(b) 2D z-slice

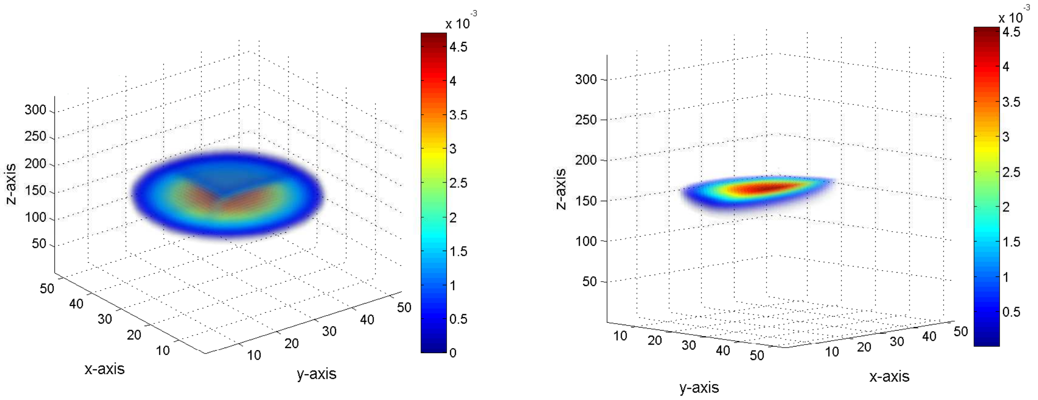

(c) 3D Full

(d) 3D Half

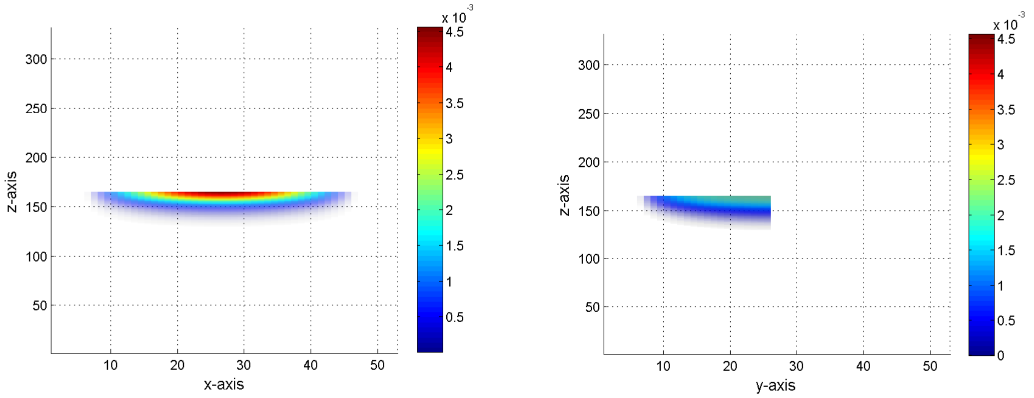

(e) 3D Half yz-view

(f) 3D Half xz-view

Figure 6.14: Two & Three dimensional normalized eigen functions visualization of as grown QD-NW 20 nm diameter.

CHAPTER 7

SUMMARY AND CONCLUSION

This work involves the modeling, numerical analysis and solution of the intermixing process. A numerical solver has been used to generate solutions for intermixing process in QD-NW based on the FDTD method. Therefore, to know the effect of the intermixing process on the emission properties of a nanostructure device, several models have to be considered such as the polarization effects, band gap alignment and quantum properties. The overall summary, conclusion and future work are presented in the following sections.

7.1 Summary

- Intermixing process in nanostructure is modeled by Fickian law in interdiffusion with an interdiffusion coefficient that depends on atomic concentration and annealing temperature.
- The parameters of the interdiffusion coefficient are calculated from the fitting curve of experimental data.

- The polarization effect is modeled by the heterogeneous Poisson equation. The indium concentration dielectric function is taken from experimental data and fitted using LSM curve fitting. The model is solved iteratively by the Successive Over Relaxation (SOR) method.
- Energy band profiles are aligned by considering Vegard's law. The potential energy from the energy band is used to couple with Schrödinger equation.
- The Schrödinger equation is solved numerically using Quantum Finite Difference Time Domain solver. The solver is able to generate eigen energies and eigen functions as emission properties.
- All numerical analysis for the models have been elaborated including discretization scheme analysis, consistency, stability criteria and convergence.
- The solver was used for one dimensional problems as well as three dimensional cases.

7.2 Conclusion

The following items are the conclusion of the research work done in this thesis.

- The ABFD differencing scheme provides correct solution for $\frac{\partial f(\mathbf{x})}{\partial \mathbf{x}}.\frac{\partial g(\mathbf{x})}{\partial \mathbf{x}}$ type equation. In the interdiffusion model, ABFD differencing scheme can maintain the total concentration and concentration distribution unlike the BD, FD and CD differencing schemes.

- The percentage of total polarization affects V, U_c, U_v, eigen energies, and eigen functions. The magnitude of V follows the polarization percentage proportionally as well as for U_c and U_v. The eigen energies shift decreases (positive) as the percentage increases. The shift of eigen functions also follows the increase of the percentage.

- The shape of the quantum well can be used as a parameter to engineer the emission of QD-NW. For the symmetrical trapezoidal shape, the length of b drives potential energies, both U_c and U_v, proportionally unlike in the asymmetrical shape that the longer b-part increases the U_c but decreases the U_v. The symmetrical trapezoidal shape with a, b and c equal to 1 nm gives the highest emission energy shift.

- The annealing time and temperature also contribute proportionally to the emission energy shift. In particular, the slope of the energy shift increases as the temperature increases. This is because the temperature in the interdiffusion coefficient model is in an exponential function, $D(T,c) = D_0(c)\exp\left(\frac{-E_a}{k_B T}\right)$.

- The concentration of indium in as-grown structure also contributes to the shift of the emission energy proportionally. In fact, the slope of the shift is also higher as the initial indium concentration is higher. It is also related to the interdiffusion coefficient, which is the prefactor that is an exponential function of concentration.

- Another parameter, the well thickness also provides proportional contribution to the emission energy shift. Like annealing temperature and as grown indium distribution, the slope of the shift is higher as the well becomes thicker. It shows that in a 3 nm wide well, the electrons and holes are better-trapped than in the 5 and 7 nm wide wells.

- In MQW, the separation length between the two wells defines the well-coupling. In case of electrons, the tail of the eigen function for a 5 nm well barrier is strongly coupled. It decreases as the separation gets longer.

- In three dimensional QD-NW simulation, the energy shift decreases as the nanowire diameter increases. It is related to the confinements of electrons and holes. A smaller nanowire in diameter gives stronger confinement compare to a larger nanowire. The efect can also be observed from its eigen functions.

7.3 Future Work

The QFDTD solution method is capable of providing emission properties of the QD-NW LED structure coupled to the interdiffusion and polarization models solution. However, there are several suggestions that can be attempted in the future.

- Three dimensional study for multi discs in QD-NW based structure. It might give a better representation of well-coupling.

- Three dimensional study for capping layer method to induce the intermixing can be considered.

- Interdiffusion coefficient, D, model has already accounted for several parameters such as concentration, annealing temperature and activation energy. New models for D that give a better experimental verification can also be incorporated in the solver.

- Experimental calibration to verify the model can be done by considering variation of as grown emissions and information of indium distribution before and after intermixing process.

- Experimental observation of QD-NW size expansion due to annealing process.

REFERENCES

[1] E. Schubert, *Light-Emitting Diodes*, 2nd ed. Cambridge, 2006.

[2] H. J. Round, "A note on carborundum," 1907.

[3] N. Zheludev, "The life and times of the led a 100-years history," *Nature Photonics*, vol. 1, 2011.

[4] M. A. Hobhkob, "Oleg vladimirovich losev pioneer of the semiconductor electronics," *Solid State Physic (Rusia)*, 204.

[5] S. Nakamura, T. Mukai, and M. Senoh, "Candelaclass highbrightness ingan/algan doubleheterostructure bluelightemitting diodes," *Applied Physics Letters*, vol. 64, no. 13, 1994.

[6] P. Harrison, *Quantum wells, wires, and dots: theoretical and computational physics of semiconductor nanostructures.* Wiley-Interscience, 2005. [Online]. Available: http://books.google.com.sa/books?id=7KzvAAAAMAAJ

[7] S. Nakamura, M. Senoh, N. Iwasa, and S. ichi Nagahama, "High-brightness ingan blue, green and yellow light-emitting diodes with quantum well

structures," *Japanese Journal of Applied Physics*, vol. 34, no. 7A, p. L797, 1995. [Online]. Available: http://stacks.iop.org/1347-4065/34/i=7A/a=L797

[8] D. L. Barton, M. Osinki, P. Perlin, P. G. Eliseev, and J. Lee, "Single-quantum well ingan green light emitting diode degradation under high electrical stress," *Microelectronics Reliability*, vol. 39, pp. 1219–1227, 1999.

[9] Y. D. Qi, H. Liang, W. Tang, Z. D. Lu, and K. M. Lau, "Dual wavelength ingan/gan multi-quantum well leds grown by metalorganic vapor phase epitaxy," *Journal of Crystal Growth*, vol. 272, pp. 333–340, 2004.

[10] C. J. Yuon, T. Jeong, M. S. Han, J. W. Yang, and K. Y. Lim, "Optical degradation of ingan/gan multi quantum well led structures induced by the md-doped p-gan activation temperature," *J. of the Korean Physical Society*, vol. 41, pp. 778–782, 2002.

[11] C. S. X. et.al, "Simulation of ingan/gan mqw leds with quantum dot model for electrical and optical effects," *Optical and Quantum Electronics*, vol. 38, pp. 1077–1089, 2002.

[12] C. P. Benjamin Damilano, Nicolas Grandjean and J. Massies, "Monolithic white light emitting diodes based on ingan/gan multiple-quantumwells," *Japan Journal of Applied Physics*, vol. 40, pp. 918–920, 2001.

[13] M. Zhang, P. Bhattacharya, and W. Guo, "Ingan/gan self-organized quantum dot green light emitting diodes with reduced efficiency droop,"

Applied Physics Letters, vol. 97, no. 1, pp. –, 2010. [Online]. Available: http://scitation.aip.org/content/aip/journal/apl/97/1/10.1063/1.3460921

[14] W. Guo, M. Zhang, A. Banerjee, and P. Bhattacharya, “Catalyst-free ingan/gan nanowire light emitting diodes grown on (001) silicon by molecular beam epitaxy,” *Nano Letters*, vol. 10, no. 9, pp. 3355–3359, 2010, pMID: 20701296. [Online]. Available: http://dx.doi.org/10.1021/nl101027x

[15] W. Guo, A. Banerjee, P. Bhattacharya, and B. S. Ooi, “Ingan/gan disk-in-nanowire white light emitting diodes on (001) silicon,” *Applied Physics Letters*, vol. 98, no. 19, pp. –, 2011. [Online]. Available: http://scitation.aip.org/content/aip/journal/apl/98/19/10.1063/1.3588201

[16] E. H. L. (editor) and M. Manasreh, *Optoelectronic properties of semiconductor and super lattices (series editor): Semiconductor quantum wells intermixing*, 2000.

[17] H.-W. Lin, Y.-J. Lu, H.-Y. Chen, H.-M. Lee, and S. Gwo, “Ingan/gan nanorod array white light-emitting diode,” *Applied Physics Letters*, vol. 97, no. 7, pp. –, 2010. [Online]. Available: http://scitation.aip.org/content/aip/journal/apl/97/7/10.1063/1.3478515

[18] S. Jahangir, A. Banerjee, and P. Bhattacharya, “Carrier lifetimes in green emitting ingan/gan disks-in-nanowire and characteristics of green light emitting diodes,” *physica status solidi (c)*, vol. 10, no. 5, pp. 812–815, 2013. [Online]. Available: http://dx.doi.org/10.1002/pssc.201200583

[19] I. Gontijo, T. Krauss, J. Marsh, and R. De La Rue, "Postgrowth control of gaas/algaas quantum well shapes by impurity-free vacancy diffusion," *Quantum Electronics, IEEE Journal of*, vol. 30, no. 5, pp. 1189–1195, May 1994.

[20] F. Qian, Y. Li, S. Gradecak, H.-G. Park, Y. Dong, Y. Ding, Z. L. Wang, and C. M. Lieber, "Multi-quantum-well nanowire heterostructures for wavelength-controlled lasers," *Nat Mater*, vol. 7, pp. 701–706, 2008.

[21] C.-C. Chuo, C.-M. Lee, and J.-I. Chyi, "Interdiffusion of in and ga in ingan/gan multiple quantum wells," *Applied Physics Letters*, vol. 78, no. 3, 2001.

[22] S. Chen and G. Wang, "Nonlocal optical properties in ingan/gan strained quantum wells with a strong built-in electric field," *Journal of Applied Physics*, vol. 113, no. 2, pp. –, 2013. [Online]. Available: http://scitation.aip.org/content/aip/journal/jap/113/2/10.1063/1.4775484

[23] B. S. Ooi, S. G. Ayling, A. C. Bryce, and J. H. Marsh, "Fabrication of multiple wavelength lasers in gaas/algaas structures using a one-step spatially controlled quantum well intermixing technique," *IEEE Photonic Technology Letters*, vol. 7, no. 9, pp. 944–946, 1996.

[24] M. D. McCluskey, L. T. Romano, B. S. Krusor, and N. M. Johnson, "Interdiffusion of in and ga in ingan quantum wells," *Applied Physics Letters*, vol. 73, no. 9, p. 1281, 1998.

[25] C.-C. Chuo, C.-M. Lee, and J.-I. Chyi, "Interdiffusion of in and ga in ingan/gan multiple quantum wells," *Mater. Sci. Semicond. Process*, vol. 16, no. 3, p. 738741, 2013.

[26] D. A. May-Arrioja, N. Bickel, A. Alejo-Molina, and M. Torres-Cisneros, "Intermixing of inp-based multiple quantum wells for integrated optoelectronic devices," *Microelectronics Journal*, vol. 40, p. 574576, 2009.

[27] X. P. (editor), D. Munteanu, and J.-L. Autran, *A 2-D/3-D Schrodinger-Poisson Drift-Diffusion Numerical Simulation of Radially-Symmetric Nanowire MOSFETs in book: Nanowires - Recent Advances*, ch. 15.

[28] D. M. Sullivan, *Quantum Mechanics for Electrical Engineers*, 2011.

[29] D. M. Sullivan, "Determination of the eigenfunctions of arbitrary nanostructures using time domain simulation," vol. 91, no. 5, pp. 3219–3226, 2002.

[30] J. M. (editor) and M. Karimi, *Diffusion in Polymer Solids and Solutions in book Mass Transfer in Chemical Engineering Processes.*

[31] T. B. Susilo, M. Alsunaidi, C. Shen, and B. Ooi, "Intermixing effects on emission properties of ingan/gan coupled quantum wells in book: Gcc conference and exhibition (gccce), 2015 ieee 8th," pp. 1–4, Feb 2015.

[32] J. P. (editor) and F. Bernardini, *Spontaneous and Piezoelectric Polarization: Basic Theory vs. Practical Recipes in book: Nitride Semiconductor Devices: Principles and Simulation*, 2007, ch. 3.

[33] J. P. (editor), R. Goldhahn, C. Buchheim, P. Schley, A. T. Winzer, and H. Wenzel, *Optical Constants of Bulk Nitrides in book: Nitride Semiconductor Devices: Principles and Simulation*, 2007, ch. 5.

[34] K. Mukai, M. Sugawara, and S. Yamazaki, "Interdiffusion process in lattice-matched inxga1-xasyp1-y/inp and gaas/alxga1-xas quantum wells," *Phys. Rev. B. Condens. Matter*, vol. 50, no. 4, p. 2273, 1994.

[35] D. M. Sullivan and D. S. Citrin, "Determining quantum eigenfunctions in three-dimensional nanoscale structures," *Journal of Applied Physics*, vol. 97, no. 10, pp. –, 2005. [Online]. Available: http://scitation.aip.org/content/aip/journal/jap/97/10/10.1063/1.1896437

Vitae

- Name : Tri Bagus Susilo
- Nationality : Indonesia
- Date of Birth : October 12^{th}, 1988
- Email : 3bagussusilo@gmail.com, tbagussusilo@gmail.com
- Permanent Address : Karanggondang RT.5 RW.2, Boyolali, Indonesia
- Academic Background :
  - Master of Science (M.Sc) in Electrical Engineering Department, King Fahd University of Petroleum and Minerals, April 2015, 3.656/4 GPA
  - Bachelor of Engineering (B.Eng) in Electrical Engineering Department, Diponegoro University, April 2011, 3.58/4 GPA
- Publication :
  - Susilo, Tri B., Khan, I., Alsunaidi, M. A.: Modelling, Identification and Verification of Intermixing Process in Coupled InGaN/GaN Multiple Quantum Wells. (abstract has been accepted in ICMAT 2015 Conference)

- Susilo, Tri B., Khan, I., Chao S., Ooi, Boon S., Alsunaidi, M. A.: Intermixing effects on emission properties of InGaN/GaN coupled quantum wells, In: The 3rd Saudi International Nanotechnology Conference, 2014. (presented)
- Susilo, Tri B., Chao S., Ooi, Boon S., Alsunaidi, M. A.: Intermixing effects on emission properties of InGaN/GaN coupled quantum wells, In: 8th IEEE GCC Conference and Exhibition, Feb. 2015. (published)
- Chen, Z., Noura, H., Susilo, Tri B., Younes, Y. A.,: Engineering Implementation on Fault Diagnosis for Quadrotors based on Nonlinear Observer, In: 25th IEEE Chinese Control and Decision Conference, 2013. (published)
- Chen, Z., Noura, H., Susilo, Tri B., Younes, Y. A.: Robust Fault Diagnosis for Quadrotor UAVs Using Adaptive Thau Observer, In: Journal of Intelligent Robot System, Oct. 23, 2013. (published)
- Wahyudie, A., Susilo, Tri B., Noura H.: Robust PID Controller for Quad-rotors, In: Journal of Unmanned System Technology, April 16, 2013. (published)